

Heat and Mass Transfer Enhancement in Rotating Disk Systems



By:

Muhammad Usman
Reg. No. 32-FBAS/PHDMA/S13

Department of Mathematics and Statistics
Faculty of Basic and Applied Sciences
International Islamic University, Islamabad
Pakistan



~~PHD~~

TH93373

PHD
516
MUH

Heat transfer
Mass transfer
Mathematics

Heat and Mass Transfer Enhancement in Rotating Disk Systems



By:

Muhammad Usman
Reg. No. 32-FBAS/PHDMA/S13

Supervised By:

Dr. Ahmer Mehmood

**Department of Mathematics and Statistics
Faculty of Basic and Applied Sciences
International Islamic University, Islamabad
Pakistan
2019**

Heat and Mass Transfer Enhancement in Rotating Disk Systems

By:

Muhammad Usman
Reg. No. 32-FBAS/PHDMA/S13

A DISSERTATION SUBMITTED IN THE PARTIAL FULFILLMENT
OF THE REQUIREMENTS FOR THE DEGREE OF DOCTOR OF
PHILOSOPHY IN MATHEMATICS

Supervised By:

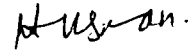
Dr. Ahmer Mehmood

Department of Mathematics and Statistics
Faculty of Basic and Applied Sciences
International Islamic University, Islamabad
Pakistan
2019

Author's Declaration

I, **Muhammad Usman** Reg. No. **32-FBAS/PHDMA/S13** hereby state that my Ph.D. thesis titled: **Heat and Mass Transfer Enhancement in Rotating Disk Systems** is my own work and has not been submitted previously by me for taking any degree from this university, **International Islamic University, Sector H-10, Islamabad, Pakistan** or anywhere else in the country/world.

At any time if my statement is found to be incorrect even after my Graduation the university has the right to withdraw my Ph.D. degree.



Name of Student: *(Muhammad Usman)*

Reg. No. **32-FBAS/PHDMA/S13**


Dated: **08/05/2019**

Plagiarism Undertaking

I solemnly declare that research work presented in the thesis titled: **Heat and Mass Transfer Enhancement in Rotating Disk Systems** is solely my research work with no significant contribution from any other person. Small contribution/help wherever taken has been duly acknowledged and that complete thesis has been written by me.

I understand the zero tolerance policy of the HEC and University, **International Islamic University, Sector H-10, Islamabad, Pakistan** towards plagiarism. Therefore, I as an Author of the above titled thesis declare that no portion of my thesis has been plagiarized and any material used as reference is properly referred/cited.


I undertake that if I am found guilty of any formal plagiarism in the above titled thesis even after award of Ph.D. degree, the university reserves the rights to withdraw/revoke my Ph.D. degree and that HEC and the University has the right to publish my name on the HEC/University Website on which names of students are placed who submitted plagiarized thesis.

Student/Author Signature: 
Name: **(Muhammad Usman)**

Certificate of Approval

This is to certify that the research work presented in this thesis, entitled: **Heat and Mass Transfer Enhancement in Rotating Disk Systems** was conducted by **Mr. Muhammad Usman**, Reg. No. **32-FBAS/PHDMA/S13** under the supervision of **Dr. Ahmer Mehmood** no part of this thesis has been submitted anywhere else for any other degree. This thesis is submitted to the **Department of Mathematics & Statistics, FBAS, IIU, Islamabad** in partial fulfillment of the requirements for the degree of **Doctor of Philosophy in Mathematics, Department of Mathematics & Statistics, Faculty of Basic & Applied Science, International Islamic University, Sector H-10, Islamabad, Pakistan.**

Student Name: Muhammad Usman

Signature: 

Examination Committee:

a) **External Examiner 1:**

Name/Designation/Office Address

Signature: 

Prof. Dr. Saleem Asghar
Professor of Mathematics,
Department of Mathematics,
COMSATS, IIT, Park Road, Chak Shahzad,
Islamabad.

b) **External Examiner 2:**

Name/Designation/Office Address)

Signature: 

Prof. Dr. Muhammad Ayub
Professor of Mathematics,
Department of Mathematics,
QAU, Islamabad

c) **Internal Examiner:**

Name/Designation/Office Address)

Signature: 

Prof. Dr. Muhammad Sajid T.I
Professor

Supervisor Name:

Dr. Ahmer Mehmood

Signature: 

Name of Dean/HOD:

Prof. Dr. Muhammad Sajid, T.I

Signature: 

Dedication

This research work is dedicated to:

The sake of **ALLAH**, my Creator and my Master,

My great Teacher and Messenger, Holy Prophet Hazrat **Muhammad (SAW)**,

Who taught us the purpose of life,

My homeland **Pakistan**,

The International Islamic University Islamabad,

The great and kind supervisor **Dr. Ahmer Mehmood**,

My great **Ammi Jan & Abu Jan**,

My dearest and beloved wife **Dr. Ayesha Usman**,

My beloved brother and bother & sisters in law

My sweet and cute nephew & nieces **Ch. Muhammad Rohan, Aiza Adnan &**

Shajia Noor,

My friends and family,

All the people in my life who touch my heart,

I dedicate this PhD thesis.

Acknowledgements

ALLAH ALMIGHTY says in Holy Quran (2:117);

“The Originator of the heavens and the earth! When He wants a thing, He says unto it only: Be! and it is.”

First and foremost, I must acknowledge my limitless thanks to Almighty **ALLAH**, all praises for HIM, the Originator of everything and bestowed upon me with one of HIS chief blessings for mankind-the thinking mind. I must also pay my gratitude to my beloved Holy Prophet **Hazrat Muhammad (Peace Be Upon Him)**; the Gem of mankind, the Sultan of creation, the Unparalleled, the Succorer of humanity (Countless Darood and unlimited blessings on Him). Without the teachings and inspirations provided by Him (peace be upon him), I would never able to complete my research work.

Pursuing a PhD degree in fact require an extreme hard work, patience, devotion, clarity of thoughts, courage, and definitely some caring people to be around. In this regard, I am very much fortune to have a good list of great persons to whom I must want to say heartfelt thanks and pay my deepest gratitude.

First of all I would like to express my sincere and heartiest gratitude to my honorable and respected supervisor **Dr. Ahmer Mehmood** who had been no less than a helicon for me throughout my research work. I can never adequately thank him for his sincere support, guidance, motivation, patience, and immense knowledge. Without his encouragement, creative ideas, efforts, continuous support, contribution, permanent guidance, and valuable criticism, the current dissertation would not have been possible. He is always being available to me for the long constructive discussions (not always technical). He rather gave me a thirst of knowledge as the only great teachers often give. I could not even imagine to have a better mentor and advisor for my present research work.

I would also like to thank **Prof. Dr. –Ing. Bernhard Weigand** for his willingness to improve some of research articles related to this dissertation. Thanks are due to **Dr. Nasir Ali, Dr. Tariq Javed, Prof. Dr. Muhammad Sajid TI** from whom I learnt a lot during my course work.

I am thankful to **Dr. Saleem Iqbal, Dr. Abuzar Ghaffari, Dr. Sami Ullah Khan, Dr. Khurram Javed, Dr. Mohsin Hassan, Dr. Mubbashar Nazeer, Dr. Zeeshan Asghar, Dr. Raheel Ahmed, Dr. Atif, Sajid Khan, Ghulam Dastgir Tabassum,**

Babir Shah, Mudasar Maskeen, Abdul Haleem Hamid for their moral support and loving attitude. I am also extraordinary fortune in having intelligent and sincere fellows like **Iqrar Raza and Muhammad Awais**. They pray a lot for my success and supported me in all situations. It's really a great pleasure for me to be with them and share different research ideas.

I would like to highly acknowledge and extend my heart full gratitude to my parents who are in fact most precious fortune for me in my life and dedicate this piece of work to them for their unconditional love, prayers, vital encouragement, generous support, and many sacrifices throughout my life and particularly during my PhD studies. I am also greatly thankful to my grandmother who has always been a source of prayers for me. I can't forget her love. My heartfelt thanks are also due to my sweet brother **Ch. Muhammad Adnan** for supporting me in multiple manners. Especially in taking huge care of parents in my absence and managing all house responsibilities both physically and financially. Without his efforts, I can't complete my task with an ease. Love is also due to little **Muhammad Rohan, Aiza Adnan, and Shajia Noor** who had always been so happy whenever they saw me at village **Gulyana**. I owe profound gratitude to my grandfather **Ch. Sadr-ud-Din (Late)**; May his soul rest in heavens, as he was in fact my first teacher and polished my mind in an efficient way when I was a child. I am giving fully credit of my PhD to him. I will miss his love and care forever and ever.

My heartiest and a special acknowledgement goes to one of the most extraordinary and intelligent person in my life who has been a blessing for me, and my great motivators – her Excellency **Dr. Ayesha Usman**, my dearest and beloved wife. I will never forget her efforts, sincerity, care, dedication, hard work, huge sacrifice, devotion, and countless giving which are always been very much assistive for me to accomplish different life tasks and to especially this one. She make me feel like that I can do anything and I am so happy to be with her.

Last but not least, many many thanks to relatives and friends; **Irfan-ul-Haq, Noman Afzal, Haroon, Naveed Asghar, Toqeer, Aqeel, Taimoor, Noman Ahmed, Amir Sajjad, Sabbar, Naseer Rabbani, Umair, Inam, Jibrán (Spain), Altamash (Spain), Faisal (Spain)**, who are always been a moral support for me in my life.

Muhammad Usman

Preface

The design of an efficient cooling system comprising of a rotating disk arrangement is essential owing to the ever-growing demand in the power output and thermal efficiency of turbomachinery systems, gas turbine, transport engineering, chemical engineering, aircraft engineering, rotating disk contractors, and many other rotating heat exchanging devices. The engineering sophistication and economic incentives of industries do also require to improve the performance of heat exchangers in order to obtain the optimum use of energy, and materials, to achieve further thermal control, and to meet the compactness requirements. Ranging from the simple turbomachinery to the state - of - the - art aerospace vehicles most of the practical rotating systems have strong connections with the rotating disk configuration, either rotating freely or in a housing. This signifies the importance of the geometrical configuration of rotating disk system as it relates to a large number of practical applications, namely, spin coating, rotational air-cleaners, disk drivers, atomizers, jet cooling, food processing, rotating machinery, medical equipment and many more. Further understanding of the convective transport mechanism due to a rotating disk, whose surface is flat and also not essentially flat, is an important area of research. Explanation to the non-trivial augmentation in heat transfer and the identification of the agents contributing there are the fundamental reasons behind this study.

Therefore, the present monograph focuses on the prediction of the enhanced heat transfer rate in some complex flows arising in the rotating disk system as it directly links to the cooling performance of such systems. On the other hand the consequential mitigation of environmental degradation has provoked many techniques of heat transfer augmentation. In this context, different approaches, such as active, passive and combined (i.e. both active and passive), techniques are employed to achieve the heat transfer augmentation. The primary objective of this work is to investigate the impact of non-homogenous distribution of nanoparticles, non-uniform disk temperature distribution, disk transpiration, waviness of the disk and the external forced flow to the rotating disk geometries. The detailed discussion of obtaining the heat transfer enhancement via Nanofluid is given in **Chapter 2** where the weak prediction of homogeneous models (as compared to non-homogeneous model) on heat transfer enhancements is identified. Almost 67% enhancement in heat transfer rate is noted for the non-uniform nanoparticle distribution (non-homogeneous modeling) for some fixed

values of the involved parameters whereas the uniform distribution (homogeneous model) yields only 22% which signifies the role of nanoparticle distribution in heat transfer augmentation. The research work presented in **Chapter 2** are published in **Thermal Science: Year 2018, Vol. 22, No. 6A, pp. 1-16**. Some new classes of rotating disk temperatures have been considered in **Chapter 3** due to which increased heat transfer rates were noticed. For instance, exponentially increasing disk temperature of a free rotating disk in the quiescent air yields 27% augmentation in heat transfer rate while a radially increasing non-linear disk temperature corresponds to 15% intensification in heat transfer rate as compared to isothermal disk. The heat transfer augmentation has also been acquired by the mass addition/removal to flow inside the gap between a cone and a disk. **Chapter 4** highlights this analysis in detail. A serious lack of work is felt in the study of surface roughness effects on rotating disk boundary-layer and this is focused in **Chapters 5 and 6**. The sinusoidal-shaped (wavy) disk has been opted as it can be dealt quite easily with the mathematical modeling. A comprehensive discussion has been made in the aforementioned **Chapters** highlighting the role of surface texture in different flow regimes like non-isothermal distribution of disk temperature and under uniform forced flow. The findings of Chapter 5 are published in **International Journal of Heat and Mass Transfer: Year 2019, Vol. 129, pp. 96-102**. Finally, inferences are drawn in the **Conclusions** section which are very helpful in order to understand the heat transfer enhancement mechanisms in rotating disk systems. It is important to mention here that the existence of the analogy between convective heat and mass transfer phenomena leads this study to cover the topic of mass transfer in a rotating disk systems as well.

TABLE OF CONTENTS

LIST OF FIGURES	X
LIST OF TABLES	XIV
LIST OF SYMBOLS	XVI
CHAPTER 1 INTRODUCTION AND PRELUDES	1
1.1 Heat and mass transfer enhancement	1
1.2 Fluid mechanics features	3
1.3 Overview of rotating flows	6
1.3.1 Essence of rotating disk systems	6
1.3.2 Literature review	8
1.4 Flow, heat and mass transfer structure	9
1.5 Heat and mass transfer enhancement in rotating disk systems	10
1.5.1 Improvements using nanofluid	11
1.5.2 Augmentation via non-uniform disk temperature distribution	13
1.5.3 Intensification due to transpiration	14
1.5.4 Enhancement due to disk topography	15
1.6 Preludes	17
1.6.1 Skin-friction coefficient	17
1.6.2 Moment torque	18
1.6.3 Moment coefficient	18
1.6.4 Mass flow rate	18
1.6.5 Displacement thickness	18
1.6.6 Swirl angle	18
1.6.7 Prandtl number	19
1.6.8 Schmidt number	19
1.6.9 Lewis number	19

1.6.10	Nusselt number.....	19
1.6.11	Sherwood number	20
1.6.12	Suction/Injection	20
1.6.13	Axially-symmetric flow	20
1.7	General assumptions	21
1.8	Governing equations	21
1.8.1	Continuity equation.....	21
1.8.2	Momentum equation	22
1.8.3	Energy equation.....	22
1.8.4	Diffusion equation.....	22
1.9	Boundary-layer equations for flat disk.....	22
1.10	Boundary-layer equations for sinusoidal disk.....	23
1.11	Solution techniques	25
1.11.1	The bvp4c algorithm	26
1.11.2	The shooting method.....	26
1.11.3	The Keller-box Method.....	26
CHAPTER 2 HEAT TRANSFER ENHANCEMENT IN ROTATING DISK		
	BOUNDARY-LAYER USING NANOFUID	28
2.1	Mathematical formulation	28
2.1.1	Nanofluid modeling.....	28
2.1.2	Mathematical model.....	31
2.2	Self-similar form of equations.....	32
2.2.1	Numerical solution	34
2.3	Results and discussion.....	34

CHAPTER 3 HEAT TRANSFER ENHANCEMENT VIA NON-ISOTHERMAL	
ROTATING DISK.....	44
3.1 Problem statement.....	45
3.2 Heat transfer analysis	46
3.2.1 Sinusoidal disk temperature variations	46
3.2.2 Exponential disk temperature distribution	47
3.2.3 Polynomial (increasing or decreasing) form of disk temperature	49
CHAPTER 4 HEAT TRANSFER AUGMENTATION IN ROTATING FLOW	
BETWEEN A CONE AND DISK WITH SUCTION/INJECTION.....	52
4.1 Problem formulation	52
4.2 Similarity solution.....	54
CHAPTER 5 HEAT TRANSFER ENHANCEMENT FROM A NON-	
ISOTHERMAL ROTATING DISK WITH SURFACE	
TOPOGRAPHY	66
5.1 Model description.....	66
5.1.1 Boundary conditions	67
5.2 Solution procedure	68
5.2.1 Non-dimensionalization	68
5.2.2 Numerical method	68
5.2.3 Quantities of physical interest	69
5.3 Heat transfer analysis	70
CHAPTER 6 HEAT TRANSFER FROM A WAVY DISK ROTATING IN	
FORCED FLOW	76
6.1 Flow configuration and heat transfer	77
6.2 Normalization.....	78

6.3	Numerical solution	78
6.4	Velocity profiles.....	79
6.4.1	Radial component of velocity	79
6.4.2	Circumferential component of velocity.....	80
6.4.3	Radial and circumferential shearing stresses on wavy disk	81
6.4.4	Heat transfer rate (CHF).....	85
6.4.5	Heat transfer rate from non-isothermal wavy disk (VWT).....	87
CHAPTER 7 CONCLUSIONS.....		95
REFERENCES.....		100

LIST OF FIGURES

Fig. 1.1: Heat exchanger.	3
Fig. 1.2: Boundary-layer flow along a flat plate.	5
Fig. 1.3: Schematic of the free rotating disk.	10
Fig. 1.4: Configuration of wavy disk.	24
Fig. 2.1: Flow geometry.	31
Fig. 2.2: Radial, transverse and axial components of velocity for different Sc	35
Fig. 2.3: Effects of Sc on pressure profile.	35
Fig. 2.4: Temperature profile for different Sc	36
Fig. 2.5: Concentration profile for different Sc	36
Fig. 2.6: Radial, transverse and axial component of velocity and temperature profiles.	37
Fig. 2.7: Effects of ϕ_∞ pressure profile.	38
Fig. 2.8: Relative moment coefficient plotted against ϕ_∞	40
Fig. 2.9: Relative Nusselt number as a function of nanoparticle concentration.	40
Fig. 2.10: Relative mass flow rate as a function of nanoparticle concentration.	40
Fig. 2.11: Relative tangent of the swirl angle plotted against ϕ_∞	41
Fig. 3.1: Variation in Nusselt number for sinusoidal disk temperature.	47
Fig. 3.2: Local Nusselt number corresponding to exponentially varying disk temperature.	48
Fig. 3.3: Local Nusselt number for polynomial distribution of disk temperature.	50
Fig. 4.1: Schematic of the flow.	53
Fig. 4.2: Dimensionless mass transfer parameter effects on radial-velocity distribution in a large conical gap between a rotating cone and stationary permeable disk. ...	57

Fig. 4.3: Dimensionless mass transfer parameter effects on tangential velocity distribution in a large conical gap between a rotating cone and stationary permeable disk.....	57
Fig. 4.4: Dimensionless mass transfer parameter effects on axial velocity distribution in a large conical gap between a rotating cone and stationary permeable disk.	58
Fig. 4.5: Dimensionless mass transfer parameter effects on pressure in a large conical gap between a rotating cone and stationary permeable disk.	58
Fig. 4.6: Dimensionless mass transfer parameter effects on temperature distribution in a large conical gap between a rotating cone and stationary permeable disk. (i) $n_* = 0.0$, (ii) $n_* = -1.0$ & (iii) $n_* = 2.0$	60
Fig. 4.7: Heat transfer rate as a function of dimensionless mass transfer parameter in a large conical gap between a rotating cone and stationary permeable disk.....	61
Fig. 4.8: Heat transfer rate as a function of dimensionless mass transfer parameter in a large conical gap between a stationary cone and permeable rotating disk.....	62
Fig. 4.9: Heat transfer rate as a function of dimensionless mass transfer parameter in a large conical gap between a co-rotating cone and permeable disk.....	63
Fig. 4.10: Dimensionless mass transfer parameter effects on radial-velocity distribution in a large conical gap between a counter-rotating cone and permeable disk.	64
Fig. 4.11: Heat transfer rate as a function of dimensionless mass transfer parameter in a large conical gap between a counter-rotating cone and permeable disk.....	65
Fig. 5.1: Temperature profile for different values of the Prandtl number.	72
Fig. 5.2: Temperature profile for different values of the disk temperature distribution exponent n_* (the curve $n_* = 0$ also characterize the concentration profile at $Sc = 0.71$).	73

Fig. 5.3: Local Nusselt number variations with surface roughness ratio for a non-isothermal wavy disk (the curve $n_* = 0$ also depicts the local Sherwood number at $Sc = 1$).	73
Fig. 5.4: Influence of Prandtl number on local Nusselt number.....	74
Fig. 5.5: Averaged Nusselt number \overline{Nu} (curve 1) and \overline{Nu}_p (curve 2) under the influence of non-uniform temperature distribution and surface roughness ratio parameters (the curves $n_* = 0$ also correspond the variation of averaged Sherwood numbers Sh and Sh_p at $Sc = 0.71$).....	74
Fig. 5.6: Effects of number of sinusoids on heat transfer rates for various temperature distribution exponent at $Pr = 0.71$ (the curve $n_* = 0$ also represents the mass transfer rate at $Sc = 0.71$).....	75
Fig. 6.1: Schematic of the disk geometry and the used coordinate system.	77
Fig. 6.2: Variation of the radial velocity component with a/ω for a wavy disk.....	79
Fig. 6.3: Variation of the radial velocity component with the surface roughness ratio at a fixed $a/\omega = 0.5$	80
Fig. 6.4: Variation of the circumferential velocity component with a/ω for a wavy disk.	80
Fig. 6.5: Variation of circumferential velocity component with the surface roughness ratio at a fixed $a/\omega = 0.5$	81
Fig. 6.6: Local azimuthal skin-friction coefficient as a function of amplitude-to-wavelength ratio with relative motion of disk and fluid.....	82
Fig. 6.7: Local radial skin-friction coefficient as a function of amplitude-to-wavelength ratio with relative motion of disk and fluid.	82
Fig. 6.8: Influence of surface roughness ratio on average radial skin-friction coefficients $\overline{C_{fr}}$ (curve 1) and $\overline{C_{frp}}$ (curve 2).	84

Fig. 6.9: Influence of surface roughness ratio on average azimuthal skin-friction coefficients $\overline{C_{f\theta}}$ (curve 1) and $\overline{C_{f\theta p}}$ (curve 2).....	84
Fig. 6.10: Dependence of average azimuthal skin-friction coefficient on the number of sinusoids.	85
Fig. 6.11: Local Nusselt number as a function of surface roughness ratio with relative motion of disk and fluid for $Pr = 0.71$	85
Fig. 6.12: Influence of surface roughness ratio on average Nusselt numbers \overline{Nu} (curve 1) and $\overline{Nu_p}$ (curve 2) for $Pr = 0.71$	87
Fig. 6.13: Dependence of heat transfer on number of waves at $Pr = 0.71$	87
Fig. 6.14: Spatial variation of Nusselt number for different temperature distribution exponents with fixed relative velocity ratio.	88
Fig. 6.15: Spatial variation of Nusselt number for different values of relative velocity ratio with fixed temperature distribution exponent.	90
Fig. 6.16: Mean Nusselt number \overline{Nu} (curve 1) and $\overline{Nu_p}$ (curve 2) under the influence of non-uniform temperature distribution and amplitude – to – wavelength ratio.	90
Fig. 6.17: Effect of Prandtl number on mean Nusselt number for various variation in relative velocity ratio at $a_0/\lambda = 0.1$	91
Fig. 6.18: Heat transfer rate influenced by number of sinusoids at $Pr = 0.71$	93

LIST OF TABLES

Table 2.1: The comparison between current results and Shevchuk [37].	34
Table 2.2: Impact of nanoparticle concentration and Schmidt number on relative values of vital physical parameters for $Pr = 6, D = 0.05, \rho_p/\rho_f = 3.98195$.	39
Table 2.3: Percent increase in the values of Nusselt number relative to the pure fluid calculated at different Pr when $D = 0.05, \rho_p/\rho_f = 3.98195$.	42
Table 2.4: Relative values of important physical parameters for different values of Pr when $D = 0.05, \rho_p/\rho_f = 3.98195, \phi_\infty = 0.1$.	42
Table 2.5: Effects of D for $Pr = 6, \rho_p/\rho_f = 3.98195, \phi_\infty = 0.1$.	43
Table 2.6: Percent increase in heat transfer rate computed for homogeneous and non-homogeneous models.	43
Table 3.1: Local Nusselt number at various stations for sinusoidal disk temperature.	46
Table 3.2: Local Nusselt number at various stations for exponentially increasing disk temperature.	48
Table 3.3: Local Nusselt number at various stations for exponentially decreasing disk temperature.	49
Table 3.4: Local Nusselt number at various stations for exponentially decreasing disk temperature.	49
Table 3.5: Local Nusselt number at various stations for non-linearly increasing disk temperature.	50
Table 3.6: Local Nusselt number at various stations for non-linearly decreasing disk temperature.	51
Table 4.1: Data of heat transfer rate, rotating cone and stationary permeable disk.	61
Table 4.2: Data of heat transfer rate, stationary cone and permeable rotating disk.	62

Table 4.3: Data of heat transfer rate, co-rotating cone and permeable disk.	63
Table 4.4: Situation of centripetal and centrifugal flow under the influence of dimensionless mass transfer parameter in the situation of counter-rotating of porous disk and cone.	65
Table 4.5: Data of heat transfer rate, counter-rotating cone and permeable disk.	65
Table 5.1: Comparison of data of heat transfer rates for non-isothermal flat disk.	69
Table 5.2: Values of $\overline{Nu_p}(\overline{Sh_p})$ at $N = 2$	72
Table 5.3: Values of temperature distribution exponent for which heat transfer from the wavy disk (at $N = 2$) is seized.	73
Table 6.1: Comparison of the present numerical calculations with the work of Mabuchi et al. [79].....	79
Table 6.2: Average azimuthal and radial skin-friction coefficients, moment coefficient, and Nusselt number (CHF) ($Pr = 0.71, N = 3$).	83
Table 6.3 (i) $Pr = 0.71$, (ii) $Pr = 1$ & (iii) $Pr = 10$: Values of mean Nusselt number $\overline{Nu_p}$ for different temperature distribution exponent and relative velocity ratios with two sinusoids.	91
Table 6.4: Values of temperature distribution exponent for which heat transfer from the wavy disk is seized.	93

List of Symbols

a	Pure constant, –
a_0	Amplitude of wavy disk, m
A	Constant having suitable dimension
b	Disk radius, m
c	Specific heat capacity of nanofluid, $\text{kgm}^2\text{K}^{-1}$
C	Concentration in the boundary-layer, –
C_w	Surface concentration, –
C_∞	Ambient concentration, –
$C_{fr}, C_{f\theta}$	Components of local shearing stress, –
$\overline{C_{fr}}, \overline{C_{f\theta}}$	Average shear stresses, –
$\overline{C_{frp}}, \overline{C_{f\theta p}}$	Average radial and tangential shear stresses related to the flat disk surface, –
C_M	Moment coefficient of flat disk, –
$\overline{C_M}$	Moment coefficient of wavy disk, –
c_0	Arbitrary constant having suitable dimensions
D	Diffusion coefficient, m^2s^{-1}
D_B	Brownian diffusion coefficient, m^2s^{-1}
D_T	Thermophoretic diffusion
d_p	Nanoparticle diameter, m
$f(\epsilon, \eta), g(\epsilon, \eta)$	Dimensionless stream functions, –
F, G, H	Dimensionless velocity components, –
h, h_E	Enthalpy, Jkg^{-1}
H_E	Dimensionless enthalpy, –
h_v	Axial velocity component for flat disk, ms^{-1}
H_w	Dimensionless velocity normal through the disk, –
$H_{w,Thrs}^{Suc}$	Minimum threshold value of dimensionless wall velocity normal to the disk due to suction, –
$H_{w,Thrs}^{Inj}$	Minimum threshold value of dimensionless wall velocity normal to the disk due to injection, –

k	Thermal conductivity, $\text{kg m s}^{-3} \text{K}^{-1}$
k_B	Boltzmann constant, $\text{kg m}^2 \text{s}^{-2} \text{K}^{-1}$
Le	Lewis number, —
m	Exponential temperature distribution exponent, —
M	Moment of flat disk, $\text{kg m}^2 \text{s}^{-2}$
\bar{M}	Rotating torque of wavy disk, $\text{kg m}^2 \text{s}^{-2}$
\dot{m}_d	Mass flow rate of flat disk, kg s^{-1}
n	Polynomial temperature exponent, —
n_*	Pure constant, —
N	Number of sinusoids, —
Nu	Local Nusselt number, —
$\overline{Nu}(\overline{Sh})$	Average Nusselt (Sherwood) number related to the actual disk surface, —
$\overline{Nu}_p(\overline{Sh}_p)$	Average Nusselt (Sherwood) number corrected by the surface area ratio, —
p	Static pressure, $\text{kg m}^{-1} \text{s}^{-2}$
P	Dimensionless pressure, —
Pr	Prandtl number, —
q	Uniform heat flux, kg s^{-3}
R	Dimensionless radial distance, r/λ , —
r	Radial distance from the rotation axis, m
$r^* = r/b$	Dimensionless radial coordinate, —
Re_r	Local Reynolds number, $\Lambda r^2/\nu$, based on radial coordinate, —
Re_λ	Reynolds number, $\omega \lambda^2/\nu$, based on wavelength, —
Re_Λ	Rotational Reynolds number, $a\Lambda^2/\nu$, —
Re_ω	Local rotational Reynolds number, $\omega r^2/\nu$, —
Re_Ω	Rotational Reynolds number, $\Omega r^2/\nu$, —
S	Wavy disk surface area, m^2
Sc	Schmidt number, —
Sh	Local Sherwood number, —
$S_w(r)$	Variable surface temperature of disk, K
T	Fluid temperature in the boundary-layer, K
T_w	Surface temperature, K

T_{∞}	Ambient temperature, K
v_r, v_{φ}, v_z	Velocity components in cylindrical coordinates, $m s^{-1}$
v_x, v_{θ}, v_y	Velocity components in curvilinear coordinates, $m s^{-1}$
v_{wd}	Suction/injection velocity, $m s^{-1}$
x	Curvilinear radial coordinate, m
y	Curvilinear normal coordinate, m
z	Axial coordinate, m
Greek symbols	
α	Thermal diffusivity of the fluid, $m^2 s^{-1}$
α_w	Swirl angle, —
β	Thermal expansion, K^{-1}
γ	Gap angle, —
δ	Boundary-layer thickness, m
δd	Displacement thickness, m
ϵ	Dimensionless x -coordinate, x/λ , —
η	Dimensionless variable, —
$\eta_1 = \frac{h}{r}$	Dimensionless variable, —
θ	Azimuthal direction for wavy disk, —
Θ	Dimensionless temperature, —
λ	Wavelength, m
Λ	Combined rotation rate, $\Lambda = (a^2 + \omega^2)^{1/2}$, s^{-1}
μ	Dynamic viscosity, $kg \cdot (ms)^{-1}$
ν	Kinematic viscosity, $m^2 s^{-1}$
ρ	Density, $kg m^{-3}$
τ_{wr}	Radial wall shear stress, $kg \cdot m^{-1} s^{-2}$
$\tau_{w\varphi}$	Tangential wall shear stress, $kg \cdot m^{-1} s^{-2}$
φ	Azimuthal coordinate, —
ϕ	Nanoparticle concentration, —
Φ	Dimensionless concentration, —
$\psi(x, y), \Psi(x, y)$	Stream functions, $m^2 s^{-1}$
ω	Disk rotation rate, s^{-1}
Ω	Cone rotation rate, s^{-1}

Subscripts

f	For base fluid
p	For nanoparticle
r	Radial velocity component
w	For wall conditions
x	Curvilinear radial velocity component
y	Curvilinear normal velocity component
z	For axial velocity component
θ	Curvilinear azimuthal velocity component
φ	For azimuthal velocity component
0	For pure fluid
∞	For ambient conditions

CHAPTER 1

Introduction and Preludes

The present research work highlights the analysis of heat and mass transfer from a rotating disk surrounded by a quiescent or moving fluid and inside a gap between a disk and a cone. It has been investigated that the heat (mass) transfer characteristics strongly relies on some major features, namely, various flow conditions, surface temperature distribution, design of the disk, non-homogeneous distribution of nanoparticles in pure fluid, pressure gradient, and transpiration. The primary objective of this dissertation is to predict the enhanced heat (mass) transfer rate in all these aforementioned situations. Therefore, it is essential to explain, first, the significance of heat and mass transfer enhancement, which is fully described in the next section.

1.1 Heat and mass transfer enhancement

A great societal challenge faced by the scientific community, especially working in power engineering, in the current era is to save the energy and material to attain more thermal control, sustainable developments, compactness requirements, etc. One of the exertion made by the researchers is the heat transfer enhancement (intensification or augmentation) towards energy saving and several other economical and mechanical benefits. In many engineering applications, a mechanical process undergoes in a very high temperature environment such as the rocket motor, Pyrolysis, Hypersonic vehicles, load-bearing applications, etc. Similarly, there is a demand of proper operations, which are capable of removing the heat produced by the prime movers of automobiles. The requirement of cooling system for the heat dissipation of electronic devices is also appropriate example. These situations necessitate an efficient heat transfer mechanism so that the working machinery can continue without any collapse. Therefore the engineers and scientists are always interested in searching the ways in which high rate of heat transfer can be achieved. In doing so, different techniques are adopted like nanoscale coating, surface coating at the micron scale, hydrodynamic cavitation, use of nanofluid, surface roughness, surface porosity, external fluid motion, etc. depending upon the suitability of the situation. Heat transfer enhancement is also essential for the

economic incentives of the industries (food process, chemical engineering, automobile, nuclear energy, aeronautic industries, air conditioning, etc.) and fuel conservations as it improves the efficiency of heat exchangers (i.e. increase the UA value of heat exchanger, utilization of the maximum possible power, etc.). Furthermore, effective heat transfer results in the reduction of size of heat exchangers which makes them more compact by reducing their capital cost.

Different approaches or techniques are employed from which heat transfer augmentation can be achieved, namely, active, passive and combined (active and passive). In passive techniques, improvements in the process of heat exchange can be obtained by increasing the surface area of heat exchanger (surface coating at micron scale level, nano scale coating, waviness, etc.); by modification of the physical properties of fluid or surface (nanofluid); by hydrodynamic cavitation; by turbulence mixing promoters; boiling and condensation, etc. External power is required for active methods to increase the heat transfer rate. Surface vibrations, jets (single/multiple impinging jets, unsteady jets and synthetic jets), spray, mechanical aids, electrostatics, etc. are the well-known active techniques used to improve overall heat transfer in heat exchangers.

Heat exchange (a concerned device is shown in Fig. 1.1) is the term used for the heat transfer between a fluid and solid or between two or more fluids. Cooling or heating of a fluid, condensation, evaporation, internal combustion engine, petroleum refineries, chemical plant power stations, cooling of electronic appliances, ventilation, etc. are the classical examples of heat exchange phenomenon. Heat and mass transfer between a fluid and a solid surface depend strongly upon the character of the momentum, thermal, and concentration boundary-layers. This fact signifies the importance of convective heat transport phenomena which is essential for diverse engineering or industrial applications, for example, heat exchangers, computer storage devices, power engineering, aerodynamic extrusion of flexible surfaces, external cooler, direct steam blowing or injection, melting spinning, glass and polymer industry, paper production, gas turbine engines, rocket motor, air-cooled turbine disks, gear wheels, fly wheels and many others. Convective heat transfer occurs as a result of the fluid motion in the presence of temperature gradients where the main concern is to estimate the heat transfer rate. There exists an analogy between heat and mass transfer (which occurs due to the presence of concentration gradients) and is also of great importance in heat exchange devices, cooling towers, condensers, evaporators, drying,

absorption, etc. This analogy enables one to use the similar governing equations (based on analogical laws) that were used to predict the heat transfer rate and acquired solutions can directly be applied if one assumes the energy equation to be the diffusion equation and heat transfer rate to be the mass transfer rate. The calculations of heat and mass transfer rates require the information of velocity, temperature and concentration fields. Therefore, to attain the increased heat and mass transfer rates in a rotating disk arrangement first the phenomenon of fluid motion associated to this system needs to be evaluated and understood.

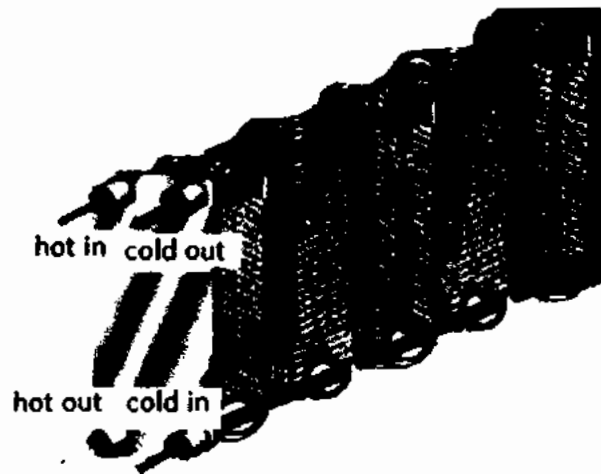


Fig. 1.1: Heat exchanger.

1.2 Fluid mechanics features

Since we live in a dense gas atmosphere on a planet mostly covered by a liquid, a simple grasp of fluid mechanics is part of our daily life. Air flow during respiratory process, observance of water flowing at high speeds while walking along a river, stirring of a tea cup containing sugar, irrigation process, etc. are good examples of fluid mechanics problems. Fluid mechanics is an important field for engineers and scientists with a lot of practical and exciting applications. Our water sewage and electrical systems heavily depend on fluid equipment. Pipes and pumps are obvious constituents of these arrangements. Furthermore, automobiles, aircrafts, spacecrafts, ships, and essentially all other vehicles comprise interactions with fluid of one kind or another, both internally and externally, inside an engine or a portion of a hydraulic control structure. It also helps us to understand and investigate many features of our body such as blood flow from the heart with the help of a branching network of blood vessels,

veins, capillaries and also lung's air cycle. Fluid mechanics problems were also being of great interest which aroused from the environment like prediction of weather, hurricanes, control of air and water pollution, flows of rivers, underground movement of water, the tidal flows, the magma flows of volcanoes and the movement of melted rocks within the earth.

The term gas, liquid, solid and fluid are casually used in daily conversation. There exists a huge misconception among the people about fluids to be synonym of liquids and the solids having so strong rigidity that they can't be deformed. Actually, the solids and fluids can basically be distinguished upon the responses given to the applied shear stresses. Under the influence of small shear stress (ratio of tangential force to area) the static deformation can be noticed in solids while a continuous deformation is an attribute of fluids. This means that fluid is such a substance which is incapable of deformation prevention. The branch of science which deals the fluid flows influenced by external forces (body, surface, etc.) is named as *fluid dynamics*. The types of flows are many, however, all such flows are usually categorized as: external or internal flows. If a fluid moves in the interior of bounding walls it is known as internal flow. The pumping of fluid through pipes is a common example of internal flows. Society could not function without water, steam, oil, air, natural gas, and many other hydrocarbons transported via piping systems. Besides this, the involved mathematicians and engineers were also concerned with the external flows, i.e. a fluid flow around the object such as a vehicle moving through a fluid or study of airfoils, etc. There are different sorts of flows arising in practical applications such as laminar flow (movement of fluids in layers) and turbulence (chaotic, disordered and unsteady). Laminar flows are rare in nature while most of the flows are turbulent. But an important fact about the laminar flows is that the solutions obtained from laminar flows serve as a basis for the simulation of turbulent flows.

Applied fluid mechanics is usually involved in the analyses or design of a mechanism having certain definite goals (e.g. an airplane, a heat exchanger, a piping system, etc.). The primary objective is to estimate the device resistance to fluid motion. For a vehicle, this flow resistance is called as drag. In piping system and in rotating electrical machines the calculation of pressure loss is of practical importance. The engineers and scientists were very much concerned with the boundary effects on fluid flows, i.e. the nature of flows near a solid boundary. The mystery of fluid motion near the walls (boundary-layer flows) was first resolved by L. Prandtl [1] in 1904. His

investigations had a worth of milestone in the discipline of fluid mechanics as it was Prandtl's findings due to which famous D'Alembert's paradox (given in 1752) was resolved. He [1] investigated that the viscous effects are important in a thin near wall regions. Examples of such flows include air flow over a sharp edged flat plate, water flow over a flat plate at zero incidence, flow past a cylinder, sphere or disk, etc. Therefore, from the Prandtl's investigation the external flows had been categorized into two regions: a thin region close to the body where viscous effects are prominent (boundary-layer region) and the remaining region in which viscous effects are not important (see Fig. 1.2).

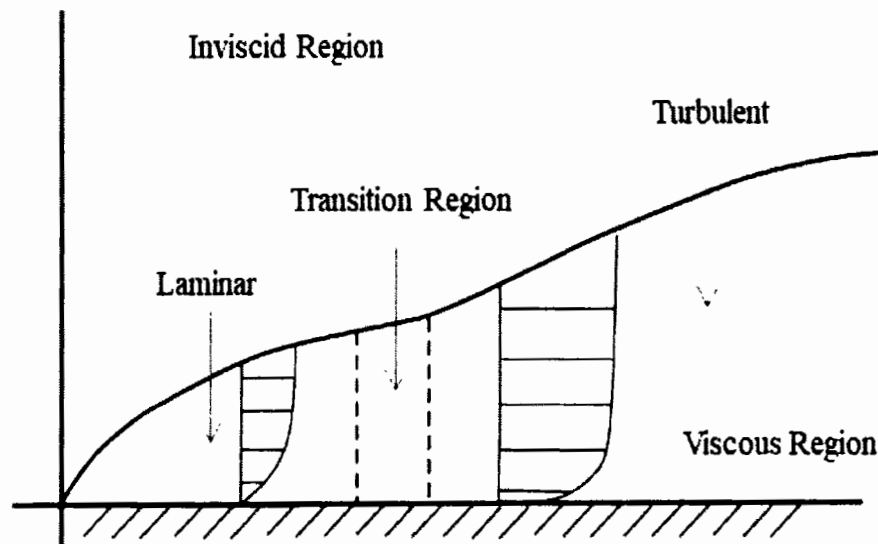


Fig. 1.2: Boundary-layer flow along a flat plate.

The calculation of drag, separation, heat, and mass transfer would have never been possible without this contribution. From the engineering prospective, calculation of the drag force, heat or mass transfer coefficient were the main concerns in boundary-layer flow problems. Drag (fluid resistance) is the component of retarding force acting on the body in the opposite direction of relative motion of fluid and object. Blasius [2], who was the student of Prandtl, calculated the drag for the fundamental flow of fluid mechanics which is known as Blasius's flow (two-dimensional flow along a stationary smooth plate). In order to model virtually all modern transportation systems the drag is a key factor and is must to be explored. It depends highly on fluid motion and in fact varies linearly with velocity in laminar flows, whereas quadratic function of velocity in turbulent flows. Apart from this, the fluid rotation has also a great impact on drag and its (drag coefficient) study is of huge importance in rotating flows. For instance, in the

design of hulls of full-scale ships, aircrafts, jet engines, etc. An overview of these flows is presented in the next section owing their diverse applications.

1.3 Overview of rotating flows

Rotation phenomena happen in abundance in natural and engineering processes such as, oceanic circulations, hurricanes, tornadoes, stirring tea in a tea cup, the atmosphere, aerospace vehicles, centrifugal pumps and aircrafts, flow of waxy crude oils, computer disk drives, car brake systems, etc. The rotation of various objects is very important in many areas of engineering and science such as rotation of earth, a turbine rotor or a space vehicle. Rotating flows are a good source of providing modeling and design for various products for example, vacuum cleaners, pumps, jet engines, gas turbine, and rotating machinery industries. Rotating fluid theory is also a helping material for the understanding of some practically important situations like many subtle fluid-structure interactions that turn out vorticity and secondary flows. For example, movement of viscous fluid through a bend of pipe or channel induces secondary flow which causes energy losses in many engineering applications. In designing of most rotating machinery, there are some common features to be considered such as curved motion, viscosity, boundary-layers, secondary flows, lift and drag. These flows are also important for many vehicles that contain liquid as fuel. Some vehicles are independent of fluid due to their heavy mass as compared to fluid. But on the other hand, for example an oil tanker or a space vehicle (90% fuel mass), the fluid mass may exceed the structural mass of vehicles. There are many technical applications of rotating flows, including viscometry, lubrication, rotating machinery (e.g. centrifugal pumps). In order to obtain 100% efficiency of the machine it is quite important to fully understand the flow phenomena taking place at the rotating components of these machines. Swirling generators, system rotation and flows in bends and turns are the common sources which give rise to rotating flows. However, the present research work has been devoted to the flows governed by rotating disk systems. The further explanation about the essence of this system is described in the next section.

1.3.1 Essence of rotating disk systems

In order to search a desirable system to study the transport phenomena of rotating fluid flow in three-dimensional boundary-layer, the rotating disk is confirmed to be the best choice. There are a multitude reasons to garner the interest of this

geometry. It allows the complete three-dimensional self-similar exact solution whereby reducing the coupled system of Navier-Stokes equations to a simple non-linear system of ordinary differential equations. Design of gas turbine, rotating disk electrodes (electro-chemistry), transport engineering (vehicle brakes), bio-and chemical reactors, rotating disk cleaners, computer disk drives, atomizers, extractors, evaporators, chemical engineering, air craft engineering, etc. necessitate the utilization of rotating disk systems. Despite the afore mentioning closely related engineering applications and the potential of mathematical simplification the rotating disk flow serves as the global paradigm for many three-dimensional flows, such as the flow on swept wings. The generation of spiral vortices at the edge of swept wings is similar in nature to the class of flow vortices developed due to the rotation of the disk in an infinite ambient fluid. The presence of the point of inflection in the laminar velocity curve of the rotating disk flow indicates the vulnerability of it to the cross flow instability. This ultimately makes the rotating disk model as an alternative laboratory towards the study and understanding of many boundary-layer features associated, particularly, with the three-dimensional flows. Based on these observations and great resemblances among the rotating disk boundary-layer and the three-dimensional boundary-layer Lingwood [3] preferred to choose the rotating disk model towards the study of absolute instability associated with the three-dimensional flow. Her investigation concludes that neither the Coriolis force nor the streamline curvature affects the absolute instability in the disk flow, which confirms the application of the disk results to the swept wing case where the Coriolis effects are absent at all. Continuing with the Lingwood's choice of disk model Pier [4] proposed a new method in order to delay the onset of transition. This was accomplished by introducing a continuously supplied periodic force in the unstable region in order to improve the ongoing self-sustained nonlinear dynamics. The laminar-turbulent transition in the boundary-layer flows can also be delayed, in some cases, because of the advantageous effects of the compliant walls. In order to investigate the supportive role of compliant wall in general, and to understand the drag reduction in the swimming dolphin's body due to the flexible nature of its skin in particular, Carpenter and Thomas [5] also preferred to choose the rotating disk model as the convenient flow geometry. Following the same analogy between the disk flow and three-dimensional boundary-layers, as utilized by the above researchers, Davies and Carpenter [6] also considered it as a prototype model for the investigation of linear global behavior of the absolute instability in three-dimensional boundary-layers. Continuing in this way Imayama [7]

contributed sufficient efforts towards the further understanding of laminar-turbulent transition in the rotating disk flow. Further relevant, and of course interesting, studies can also be found in the bibliographic items of [7]. The general reason behind the preference to the rotating disk model in the above studies is the most general nature of disk flow that resembles in large to the three-dimensional flows. The glimpses from the bulk of available literature seem to be sufficient for the reader in order to make him realize the wider scope and physical richness of the von Kármán swirling flow [8]. Apart from this, the flow analysis of cone-disk systems are very useful in viscometry, medical equipment, etc. From here one can feel the importance of investigation of flows associated with the rotating disk systems and in order to find a gap for further investigation one must need the comprehensive literature survey which is accomplished in the coming section.

1.3.2 Literature review

A classical fluid mechanics problem, the free rotating disk boundary-layer flow was initiated by von Kármán [8] in 1921. He transformed the well-known Navier-Stokes equations into coupled ordinary differential equations using similarity transformations. Cochran [9] made the first extension in von Kármán's flow in 1934 by considering the impulsive fluid motion started from rest. A steady state asymptotic solution of accuracy of higher degree was reported by him. Theoretical as well as experimental studies of this problem were also conducted by Goldstein [10] and Gregory et al. [11] in 1935 and 1955, respectively. Schlichting and Truckenbrod [12] and Tifford [13] in 1951 and 1952, respectively, studied the rotating disk flow in a uniform stream. The permeability of rotating disk was discussed by Stuart [14] in 1954 and Mithal [15] in 1961 where they explored the influence of mass-withdrawal on rotating disk boundary-layer. Axially-symmetric flow between two disks was analyzed by Lance and Rogers [16] in 1961. In 1966, Benton [17] improved the unsteady solution of Cochran. The flow between a stationary and a rotating disk was addressed by Mellor et al. [18] in 1968. The micropolar fluid flow due to rotating disk was studied by Gram and Anwar [19] in 1979. In 1979 also, Wang and Watson [20] examined the porosity effects in the rotating disk system. The compressible flow over a rotating disk was executed by Solan et al. [21] in 1983. The magnetic effects on the unsteady rotating disk flow were studied by Attia [22] in 1998. Attia and Hassan [23] also investigated the Hall effects on this flow in 2004. In the same year Miklavcic and Wang [24]

considered the partial slip effects on the disk surface. The unsteady von Kármán's swirling flow had been analyzed by Mehmood et al. [25] in 2010.

Laminar heat transfer due to a rotating disk was first investigated by Milsaps and Pohlhausen [26] in 1952 for a small range of Prandtl numbers. A more general analysis related to the Prandtl numbers was made by Sparrow and Gregg [27] in 1959 in the uniform disk temperature situation. Hartnett [28], Hartnett et al. [29] and Tien and Tsuji [30] in 1959, 1961 and 1963, respectively, considered the non-uniform temperature of the disk surface permitting the similarity solution. The convective mass transfer due to rotating disk flow discussed in detail by Levich [31] in 1962. Oxygen mass transfer rate due to rotating disk was reported experimentally by Ellison and Cornet [32] in 1971. Convective mass transfer rate had also been measured experimentally by Beg [33] in 1973. A theoretical relation for the mass flux comprising convective transport in the direction of axis of rotation to a disk rotating in a non-Newtonian fluid was obtained by Grief and Paterson [34] in 1973. Heat transfer performance in a flow between co-rotating parallel disks was determined theoretically by Yoon and Yang [35] in 1984. Flow and heat transfer within rotating disk chemical vapor deposition (CVD) had been modelled by Evens and Grief [36] in 1987 in which helium gas was taken as a carrier gas. A more detailed and comprehensive study related to heat/mass transfer in rotating disk systems had been accomplished by Shevchuk [37]. After the completion of brief review the flow structure of free rotating disk is necessary to be understood, which is explained in the next section.

1.4 Flow, heat and mass transfer structure

Consider a uniform flat disk centered at $z = 0$ in three dimensional space. The disk is surrounded by the fluid. The radius of the disk is assumed to be large enough so that it is larger than the boundary-layer thickness; edge effects have been ignored due to which the flow resembles to that considered by von Kármán [8] for an infinite disk. The disk rotates about the $z -$ axis with an angular speed ω . The disk temperature is T_w where the ambient temperature is assumed to be T_∞ . A schematic of the flow geometry is shown in Fig. 1.3. The structure of three-dimensional boundary-layer flow and heat transfer is quite simple. v_ϕ be the first component of velocity representing the azimuthal flow across the entire disk, as the fluid attached to the wall of the disk is spun up due to the disk rotation and moves in circumferential direction. However, the fluid is also thrown outwards in radial direction due to the influence of centrifugal force. The

superimposition of these two flow directions acts in such a way that the fluid rotates in a spiral fashion and it is lost at the disk edges due to its drawing in downwards direction into the boundary-layer across the entire disk which is replaced by the axial component of velocity. Thus, the flow induced by the free disk rotation operates similar to the centrifugal pump. Whereas, the heat and mass transfer boundary-layers are the same as they are on the flat plate. One directly looks forward to the ways which enhance the heat and mass transfer rates in the rotating disk systems, after the complete understanding of the rotating disk flow and associated heat and mass transfer phenomena, which are briefly discussed in the next section.

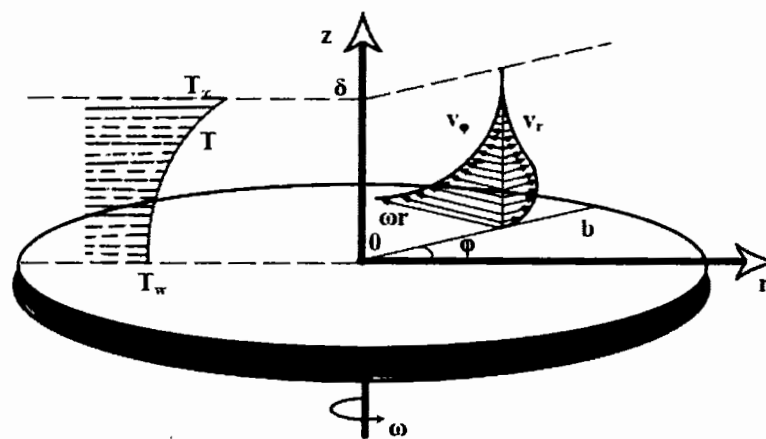


Fig. 1.3: Schematic of the free rotating disk.

1.5 Heat and mass transfer enhancement in rotating disk systems

The working fluid in almost all heat transfer system is circulated by a pump and one can reduce the consumption of associated power with the help of heat transfer augmentation. Numerous industrial applications (turbo machinery, aerospace engineering, flywheels, gear wheels, power engineering, air-cooled turbine disks, gas turbine engines, etc.) highlighted the requirement of more precise understanding of flow and heat transfer in disk pumps. Especially, there is still a room for the improvements in heat transfer and viscous drag in the flow near a rotating disk in order to predict the power losses and improved cooling phenomena in the devices which operate in the situations of high speed and temperature. Heat/mass transfer augmentation in rotating disk systems is the main concern in the current study where different techniques are

adopted like the use of nanofluid, non-uniform disk temperature, suction/injection, disk roughness and external flow which yield significant heat/mass enhancement thus resulting in improving the efficiency of rotating disk systems. In the following the detail is given one by one:

1.5.1 Improvements using nanofluid

The primary objective of the current analysis is to search out the mechanisms which lead to heat transfer augmentation in rotating disk systems. In doing so, the heat transfer enhancement in rotating disk boundary-layer has been first achieved through nanofluid which is addressed in **Chapter 2** in detail. The notion of nanofluid comes from the fact that metals have higher thermal conductivity than liquids. Due to the advent of nanotechnology it became possible to create metallic particles of nanoscale that can be mixed in a fluid (called base fluid) to form a nanofluid with enhanced thermal conductivity. Addition of small metallic particles has a big impact on thermophysical properties of the fluid. The flow and heat transfer with micro size particles was first studied by Maxwell [38] in 1904. Though he revealed some enhancement in heat transfer but the particle dimensions caused sedimentation; abrasion, and clogging (see, for instance [39]). It was realized that in order to keep the mixture homogeneous, the size of the particles needed to be minimized. This can now easily be achieved with the help of modern nanotechnology, which can produce particles of the size between 1nm-100nm. Due to extremely small- sized particles, comparable to the size of the molecules of the base fluid, they are easily accommodated by the fluid and the aforementioned issues caused by the micro sized metallic particles get resolved. Choi [40] was the first who introduced the word ‘nanofluid’ for such fluids. In most of the available literature on nanofluids, the researchers modeled the nanofluid as a homogeneous mixture by incorporating the role of thermophoresis and Brownian motion [41, 42] which are commonly known as the Buongiorno model and the Tiwari and Das model, respectively. Several authors investigated heat and mass transfer phenomena through Buongiorno [41] and Tiwari and Das [42] models for a variety of flow geometries, a few of them are mentioned here [43, 44, 45, 46]. Based on this modeling Magia et al. [45] and Avramenko et al. [47, 48] pointed out that, due to homogeneous models, the heat transfer coefficients of nanofluid are underpredicted. The reason is the incorrect incorporation of local concentration of the nanoparticles within the boundary-layer. The drawback with the Buongiorno [41] and Tiwari and Das

[42] models are the consideration of uniform distribution of nanoparticles in the base fluid. This is actually done on the basis of experimental evidences. However, the homogeneous distribution of nanoparticles is not sustained within the boundary-layer due to the relative motion of nanoparticles and fluid. Frank et al. [49] and Ding and Wen [50] theoretically proved the non-homogeneous distribution of nanoparticles in the nanofluid as a consequence of velocity and temperature gradients. The existence of concentration gradients is also confirmed through experiments [46]. Such a consideration of non-homogeneous concentration of nanoparticle also results in heat and mass transfer rate augmentation. This issue has recently been addressed by Avramenko et al. [47] and Mehmood and Usman [51, 52] where they successfully incorporated the effects of convective transport of nanoparticles on momentum, thermal and mass transfer phenomena within the boundary-layer. For detailed information it is fruitful to follow [53, 54, 55]. Inspired from this idea and after a close look at the available literature concerning the study of nanofluid over a rotating disk one finds a room for studying heat and mass transfer enhancement in a rotating disk system using the idea of non-homogeneous distribution of nanoparticles in the boundary-layer. In literature, the majority of the researchers gave interest to study the homogeneous distribution of nanoparticles. For instance, Bachok et al. [56] studied the effect of nanofluid on heat transfer in rotating flow near a porous disk. Turkyilmazoglu [57] considered the same flow for a non-porous disk taking five different types of nanoparticles. Enhanced heat transfer rate was noticed in both the studies [56, 57] where the uniform homogenous model of nanofluid was considered. Further results on the rate of heat and mass transfer enhancement can be found in recent studies concerning rotating disk systems [58, 59, 60]. In all these studies [56, 57, 58, 59, 60] the nanoparticle concentration gradient as well as the dependence of fluid properties on nanoparticle distribution has not been taken into account. Hence the main objective of **Chapter 2** is to consider forced convection heat and mass transfer phenomena in a rotating disk boundary-layer. The fluid properties are considered as variable, depending upon the nanoparticle concentration. Enhanced rate of heat transfer has been calculated and the effects of nanoparticle concentration on mass flow rate and moment coefficients are also highlighted. Results are interpreted through several graphs and Tables presented in **Chapter 2**.

1.5.2 Augmentation via non-uniform disk temperature distribution

An interesting aspect of the rotating disk flow is the existence of self-similar solution. In this connection an exact self-similar solution to the associated heat transfer problem is possible if the disk temperature is either constant or variable; following the power-law form. Owing to this fact an exact self-similar solution to the laminar heat transfer due to an isothermal rotating disk was first investigated by Milsaps and Pohlhausen [26] for a small range of Prandtl numbers. A more general analysis related to the extended values of the Prandtl number was made by Sparrow and Gregg [27] for the isothermal free rotating disk. Hartnett [28], Hartnett et al. [29] and Tien and Tsuji [30] considered the non-uniform disk temperature (following the power-law form) and obtained a similarity solution. So-far, the problem of thermal transport due to a rotating free disk is restricted to the self-similar cases for which the disk temperature must, in general, follow the power-law form. Other forms of the variable disk temperature, for which the solution is non-similar, have never been considered, to the best of our knowledge.

Therefore, for the case of non-uniform distribution of disk temperature a huge gap is felt reflecting the requirement of considering the other forms of the disk temperature. An attempt has been made in this regard in **Chapter 3** to fill the gap, though by a little, by taking the variable disk temperature generated by famous analytic functions such as sinusoidal, exponential and the polynomial function which do not allow the self-similar solution to the thermal transport equations. Interestingly, such specifications of the variable surface temperature had already been reported in [61, 62] for the case of the vertical flat plate.

Corresponding to the above mentioned forms of the disk temperature the wall heat flux does not remain self-similar at all radial locations. Consequently, the Nusselt number does also depend upon the radial variable r and is designated as a local Nusselt number. The present analysis comprises of both quantitative and qualitative results for the heat transfer rate as a function of radial distance on the disk surface for a wide range of Prandtl numbers (from 0.1 to 100). It is worth mentioning that the heat transfer characteristics reported for the flat plate case [61, 62] can also be seen in the disk case for the considered all three cases in a qualitative sense. For the considered heat transfer problem, detailed numerical data have been reported in the form of several Tables in

Chapter 3. Such computed data can indeed serve as a reference for the other future works either experimental or theoretical.

1.5.3 Intensification due to transpiration

The heat transfer augmentation has also been acquired by the mass addition/removal to flow inside the gap formed between a cone and a disk. **Chapter 4** highlights this analysis in detail. The arrangement of cone-plate is usually used in viscometry [63, 64, 65], in the biomedical field [66], and also in engineering [67]. Mooney and Ewart [63] were the pioneer who considered such a geometry in 1934 by developing the theory of conical region. They also verified the available theoretic relations regarding the measurement of fluid viscosity, applied torque and rotation rate with the aid of experimental measurements. After that many researchers [64, 65, 66, 67] utilized this geometry to measure the viscosity of fluids and to explore the secondary flow phenomena associated with cone and plate devices. Analytical solution of the cone-plate configuration for a small conical gap angle was obtained by Sodoungous [64] and Buchmann [66] with the help of perturbation techniques, whereas a detailed numerical solution to this problem was reported by Fewell and Hellums [65] in 1977. For a rotating disk and cone configuration, a comprehensive study was performed by Shevchuk [68, 69, 70] in which he presented the self-similar formulation of the momentum as well as the energy and diffusion equations. In ref. [68] Shevchuk in fact analyzed the flow and heat transfer characteristics under different situations like rotating cone with fixed disk, fixed cone and rotating disk, simultaneous co- as well as counter-rotation of the disk and cone cases. He concluded that the rate of heat transfer, under different flow situations, strongly depends upon the radial distribution of temperature on the disk surface. The complexity of the aforementioned problem [68] becomes more severe when the disk is permeable and permits the mass addition or removal at its surface. Such fluid removal or injection is of particular interest as it helps in analyzing the transport phenomena under the controlled boundary conditions, especially in the cooling process and for the transpiration cooling. Owing to this interesting feature, we have focused on mass transfer phenomena either to or from the fluid occupying the gap between a cone and disk by direct suction or injection in **Chapter 4**. The mass transfer rate (addition or removal) is considered to be uniform at all points on the entire disk surface. All possible cases, namely, (i) rotating cone and stationary disk (ii) stationary cone and rotating disk (iii) simultaneous co-rotation (iv)

counter-rotation of the disk and cone have been investigated in order to analyze the effects of suction/injection on the flow and heat transfer phenomena. The obtained solution comprises of interesting findings, which provide the in-depth understanding and detailed information regarding the dependence of flow and heat transfer characteristics upon the small or large suction/injection velocities.

1.5.4 Enhancement due to disk topography

It has been generally (both empirically and theoretically) admitted that surface interruptions usually expedite the heat transfer process. The periodic interruptions on the heat transferring surface make the thermal boundary-layer thinner which consequently increases the heat transfer rate. Consequently, pressure drop is enlarged with this strategy which ultimately requires the increased pumping power. These facts reflect the importance of design optimization which significantly affects the heat exchanger performance. However, in the case of a rotating disk geometry with periodic surface undulations on the disk surface an increased pumping power is also achieved without any extra effort. The advantage of rotating wavy disk is not limited to the increased heat transfer coefficient only. It also increases the power of the turbomachinery by increasing the torque of the rotating components. In this regard the advantage of the surface interruptions can be regarded as multifold.

Heat transfer enhancement due to the non-flat disk surface was first investigated by Le Palec [71], to the best of our knowledge. The theoretical as well as experimental work of Le Palec [71] and Le Palec et al. [72], signifies the impact of design parameters on the mechanism of heat transfer enhancement related to rotating disk systems. The periodic (sinusoidal) disk surface interruptions considered in [71] correspond to overall 15% heat transfer enhancement in comparison to the uninterrupted disk surface. Similarly the moment coefficient increases appreciably for such configurations as reported by Yoon et al. [73] which shows increased pumping power of wavy disk. These facts indicate the significance of surface irregularities towards heat transfer augmentation in laminar flow and heat transfer in a rotating disk boundary-layer. Heat transfer coefficient had been quite significantly influenced by the wall topography and it has been studied extensively by the researchers [74, 75, 76, 77, 78].

Compared to the flat disk situation the literature on the non-flat wavy disk is very limited. Because of very few investigations devoted to this topic the convective transport phenomena on a rotating rough disk is so-far less understood, as mentioned

above. Within the available literature, the cases of uniform disk temperature and heat flux have only been considered. Therefore, it is interesting to consider the other boundary conditions for the wall temperature such as the non-isothermal wall conditions. For this purpose, a non-uniform distribution of disk temperature in the form of power-law function of its radius, which has directly been observed in many engineering applications, is considered in **Chapter 5**. The prime objective of the work presented in **Chapter 5** is to quantify the results of local as well as overall heat transfer rate in comparison to the flat disk and to explore the richer physics associated with the geometry of disk. Numerical calculations are performed for a wider range of Prandtl (Schmidt) number which varies from 10^{-2} to 10^4 by varying the power index n_* from -2 to 4 . Due to the analogy between convective heat transfer and mass transfer phenomena the obtained findings of the study (in **Chapter 5**) are two-fold as they also characterize the mass transfer rate from the wavy rotating disk with a uniform distribution of mass at the disk surface. The results are valid for the Schmidt number ranging between 10^{-2} and 10^4 .

Different options can be adopted in the consideration of free disk flows depending on whether the ambient fluid is stationary and the disk is rotating or whether the disk is rotating in the presence of an external forced flow or the rotating fluid surrounds the stationary disk etc. These different choices reflect the significant variation in the flow characteristics, which in turn influence the heat transfer rate and the other parameters of engineering interest. Impact of outer forced flow orthogonal to the rotating disk is highly useful for cooling or heating the disk surface. Particularly, rotor end surfaces of the gas turbine are cooled through the application of such flows. The fundamental work regarding the analysis of these flows on a rotating flat disk along with heat transfer phenomena can be found in [30, 79, 80, 81]. More recently a comprehensive study was made by Wiesche and Helzig [82] in which theoretical as well as experimental investigation accompanying convective heat transfer from rotating disk subjected to stream of air has been done. They pointed out the advantageous aspect (especially on heat transfer enhancement) of forced flow on a rotating disk under different environments. This class of flow is also considered as a more general problem, having the free rotating disk flow as a limiting case. The relative motion of the disk and the fluid causes a considerable influence on the power needed to spin the flat disk as the torque coefficient increases significantly.

A large number of engineering applications require the study of the heat transfer and fluid flow characteristics of a simultaneous forced flow combined with rotation of solid bodies. By combining the useful effects of relative fluid motion along with altered geometrical configurations of the disk surface, as specified by Le Palec [71], it is of practical interest to investigate the flow and heat transfer phenomena in case of relative motion of a wavy disk and a superimposed forced flow (i.e. to predict the heat transfer rate and shear stresses in the situation of relative motion of fluid and sinusoidal-shaped disk). This all has been fully addressed in **Chapter 6**. It is worth mentioning that the flows addressed by von Kármán [8], Mabuchi et al. [79], and Le Palec [71] are limiting cases of the current study. The influence of surface texture of the disk rotating in a superimposed forced flow on the heat transfer (along with a non-uniform distribution of temperature on the disk surface) and the torque coefficient, which are of particular interest in technological applications, is investigated in **Chapter 6** by numerical calculations. The constant heat flux case under the action of uniform external radial flow has also been explored in **Chapter 6**.

At the end (in **Chapter 7**) detailed conclusive remarks of the whole work of current dissertation is given which in fact summarizes the outcome of the whole study.

Some of the basic terms, flow and heat and mass transfer assumptions, governing equations for the problems discussed above and their solution techniques have been explained in the rest of this chapter.

1.6 Preludes

1.6.1 Skin-friction coefficient

It is a dimensionless quantity describing the frictional force (at the boundary) occurring between solid surface and a fluid. Mathematically, it can be written as

$$C_f = \frac{\tau_w}{\frac{1}{2}\rho v^2},$$

where τ_w denotes the skin shear stress at the wall and v being the characteristic velocity of the flow such as $v = \omega r$ for free rotating disk. In the case of rotating disk, the shear stress has two components: radial and circumferential which lead to two components of skin-friction coefficients.

Radial skin-friction coefficient

For the rotating disk, it can be written as

$$C_{fr} = \frac{\tau_{wr}}{\frac{1}{2}\rho v^2}; \quad \tau_{wr} = \left. \frac{\partial v_r}{\partial z} \right|_{z=0}.$$

Tangential skin-friction coefficient

Mathematically, it is written as

$$C_{f\varphi} = \frac{\tau_{w\varphi}}{\frac{1}{2}\rho v^2}; \quad \tau_{w\varphi} = \left. \frac{\partial v_\varphi}{\partial z} \right|_{z=0}.$$

1.6.2 Moment torque

The moment on one side of a rotating disk is denoted and defined as

$$M = -2\pi \int_0^b r^2 \tau_{w\varphi} dr.$$

1.6.3 Moment coefficient

It is a dimensionless quantity to represent the power of a disk pump and is defined as

$$C_M = \frac{2M}{\frac{1}{2}\rho\omega^2 b^5}.$$

1.6.4 Mass flow rate

The fluid which is pumped in outward direction on one side of the disk due to the centrifugal force of a rotating disk is given by

$$\dot{m}_d = 2\pi b \rho \int_{z=0}^{\infty} v_r dz.$$

1.6.5 Displacement thickness

It is the distance displaced by the fluid as a result of velocity variations within the boundary-layer. It is defined as

$$\delta^* = \frac{1}{\omega r} \int_{z=0}^{\infty} v_\varphi dz.$$

1.6.6 Swirl angle

The flow swirl angle at the disk surface is calculated as

$$\alpha_w = - \left(\frac{\partial v_r / \partial z}{\partial v_\varphi / \partial z} \right)_{z=0}.$$

1.6.7 Prandtl number

The Prandtl number (Pr) signifies the nature of the fluid. A dimensionless number described by the ratio of momentum and thermal diffusivity, that is

$$Pr = \frac{\text{momentum diffusivity}}{\text{thermal diffusivity}} = \frac{\nu}{\alpha}$$

Most common gases and air at room temperature correspond to the value of Prandtl number ($Pr =$) 0.71. For water its value is 7.56 (at $17^{\circ}C$). Larger values of Prandtl number represent mostly liquids. For instance, $Pr = 10^5$ refers to some oils.

1.6.8 Schmidt number

The Schmidt number (Sc) is analogous to the Prandtl number and is the quotient of momentum and mass diffusivity. Mathematically, it can be written as

$$Sc = \frac{\text{momentum diffusivity}}{\text{mass diffusivity}} = \frac{\nu}{D}$$

For the gases it takes the values in the range 0.20-3.20 whereas for the liquids it assumes the values 100-1400 and even larger than this.

1.6.9 Lewis number

Simultaneous convective heat and mass transfer involves the Lewis number (Le) which is the ratio of thermal and mass diffusivity. Mathematical form of Lewis number is given by

$$Le = \frac{\text{thermal diffusivity}}{\text{mass diffusivity}} = \frac{\alpha}{D}$$

It can also be written as

$$Le = \frac{Sc}{Pr}$$

1.6.10 Nusselt number

The Nusselt number (Nu) is the quantitative measure of heat transfer rate to or from the wall and is a dimensionless quantity which can be defined as the ratio of convective to conductive heat transfer as

$$Nu = \frac{hL}{\kappa}$$

One can predict the heat transfer enhancement from the value of Nusselt number. From engineering prospective, heat transfer rate is predicted in two aspects, namely, (i) the

local heat transfer rate and (ii) the global heat transfer rate. On this basis the Nusselt number is also classified as (i) the local Nusselt number and (ii) the global Nusselt number which is explained as:

Local Nusselt number

It measures the heat transfer rate at a specific location of a bounding surface and its mathematical form is given by

$$Nu_x = \frac{h_x x}{\kappa}$$

In the local Nusselt number (Nu_x) the length 'x' should be considered as distance from a certain fixed point on the surface. Such flows are usually of non-similar nature.

Global Nusselt number

It measures the overall heat transfer rate over the whole region of the surface. It is also known as average Nusselt number because it is calculated by integrating the relation of local Nusselt number over the range of interest and is given by

$$\overline{Nu} = \frac{1}{L} \int_0^L Nu_x dx.$$

1.6.11 Sherwood number

Sherwood number (Sh) is a dimensionless number (analogous to the Nusselt number) in the studies of convective mass transfer and is interpreted in the same way as the Nusselt number for the heat transfer studies.

1.6.12 Suction/Injection

For the heat transfer enhancement suction is also an effective mode. In this process mass (fluid) is drawn out from the boundary-layer in the inner region of the body through narrow pores. Similarly the addition of fluid through pores of the body into the boundary-layer is known as wall injection or blowing. In most cases heat transfer rate increases due to the suction and reverse trend is seen in the case of blowing. Suction also controls the boundary-layer and sufficient amount of suction can prevent the separation of boundary-layer. On the other hand, blowing causes to destabilize the flow, in general.

1.6.13 Axially-symmetric flow

Throughout this dissertation, the primary geometry of interest is the circular disk configuration. All the work has been done with the assumption that fluid velocity is

independent of circumferential angle and such assumption designates the flow (in literature) as axially-symmetric flow.

1.7 General assumptions

Certain assumptions about the flow and heat transfer process have been made throughout the presented research work which are listed as under:

- a) Steady flow
- b) Laminar flow
- c) Incompressible flow
- d) Axis-symmetric flow
- e) Viscous dissipation is absent
- f) Cylindrical (flat disk) and curvilinear (wavy disk) coordinates are considered
- g) Newtonian fluids
- h) Absence of body forces
- i) Fixed frame i.e. the Coriolis forces are excluded

1.8 Governing equations

The flow of any viscous fluid is governed by the fundamental set of equations commonly known as Navier-Stokes equations which were independently developed by Claude-Louis Navier and George Gabriel Stokes in 1800's. For a moving fluid, these equations express the relationship existing among the velocity, temperature, pressure, and density. The influences of viscosity had also crucial role on the fluid motion which was incorporated in the Navier-Stokes equations and being an extension of the famous Euler equations. These equations are provoked from Newton's second law of motion. For (almost) all actual practical situations, these lead to a complex system of partial differential equations with the necessity of the satisfaction of law of conservation of mass. For the studies involving heat and mass transfer phenomena the law of conservation of mass and concentration are also appended to these equations.

1.8.1 Continuity equation

It is the mathematical statement of the law of conservation of mass and it serves as a constraint which must be obeyed by the velocity vector. In cylindrical coordinates it is given as

$$\frac{\partial(\rho r v_r)}{\partial r} + \frac{1}{r} \frac{\partial(\rho r v_\varphi)}{\partial \varphi} + \frac{\partial(\rho r v_z)}{\partial z} = 0, \quad (1.1)$$

which reduces to

$$\frac{\partial(r v_r)}{\partial r} + \frac{1}{r} \frac{\partial(r v_\varphi)}{\partial \varphi} + \frac{\partial(v_z)}{\partial z} = 0,$$

for an incompressible fluid.

1.8.2 Momentum equation

It is based on the basic law of mechanics (Newton's 2nd law of motion) and has three components which correspond to following set of equations (in the absence of body force)

radial component:

$$\rho \left(\frac{\partial v_r}{\partial t} + v_r \frac{\partial v_r}{\partial r} + \frac{v_\varphi}{r} \frac{\partial v_r}{\partial \varphi} - \frac{v_\varphi^2}{r} + v_z \frac{\partial v_r}{\partial z} \right) = -\frac{\partial p}{\partial r} + \mu \left(\nabla^2 v_r - \frac{v_r}{r^2} - \frac{2}{r^2} \frac{\partial v_\varphi}{\partial \varphi} \right), \quad (1.2)$$

circumferential component:

$$\rho \left(\frac{\partial v_\varphi}{\partial t} + v_r \frac{\partial v_\varphi}{\partial r} + \frac{v_\varphi}{r} \frac{\partial v_\varphi}{\partial \varphi} + \frac{v_r v_\varphi}{r} + v_z \frac{\partial v_\varphi}{\partial z} \right) = -\frac{\partial p}{\partial \varphi} + \mu \left(\nabla^2 v_\varphi - \frac{v_\varphi}{r^2} + \frac{2}{r^2} \frac{\partial v_r}{\partial \varphi} \right), \quad (1.3)$$

axial component:

$$\rho \left(\frac{\partial v_z}{\partial t} + v_r \frac{\partial v_z}{\partial r} + \frac{v_\varphi}{r} \frac{\partial v_z}{\partial \varphi} + v_z \frac{\partial v_z}{\partial z} \right) = -\frac{\partial p}{\partial z} + \mu (\nabla^2 v_z), \quad (1.4)$$

$$\text{where } \nabla^2 = \frac{\partial^2}{\partial r^2} + \frac{1}{r} \frac{\partial}{\partial r} + \frac{1}{r^2} \frac{\partial^2}{\partial \varphi^2} + \frac{\partial^2}{\partial z^2}.$$

1.8.3 Energy equation

It is based on law of conservation of energy (first law of thermodynamics) and has the following form in cylindrical coordinate system

$$\frac{\partial T}{\partial t} + v_r \frac{\partial T}{\partial r} + \frac{v_\varphi}{r} \frac{\partial T}{\partial \varphi} + v_z \frac{\partial T}{\partial z} = \alpha (\nabla^2 T). \quad (1.5)$$

1.8.4 Diffusion equation

The transport phenomena of any species in a fluid flow is described by Fick's law and is governed by the following equation

$$\frac{\partial C}{\partial t} + v_r \frac{\partial C}{\partial r} + \frac{v_\varphi}{r} \frac{\partial C}{\partial \varphi} + v_z \frac{\partial C}{\partial z} = D (\nabla^2 C). \quad (1.6)$$

1.9 Boundary-layer equations for flat disk

According to the Prandtl's idea of boundary-layer, the flow of fluid can be divided into two regions: viscous and inviscid. It has been observed that the viscous part of the flow

domain is actually very thin as compared to the whole domain. Based on this observation it was realized that the velocity varies very rapidly across this thin region. Because of this fact Prandtl proposed that (for a two-dimensional flow (say)) there must be two different length scales for the non-dimensionlization of space variables. This idea then gave birth to the order of magnitude analysis which simplifies the governing differential equations to a great extent. Continuity equation (1.1) remains the same after the implementation of order of magnitude analysis. Whereas the application of this analysis to the laws of conservation of momentum, energy, and concentration corresponds to the following assumptions:

- (i) The magnitude of axial velocity component is much smaller than the magnitude of the radial or tangential velocity components.
- (ii) The radial rate of change of all involved variables excluding pressure is much smaller than their axial rate of change.
- (iii) The pressure is only function of radial distance from rotation axis.

These assumptions hold for rotating disk boundary-layer flows as explained by Owen and Rogers [83]. Under these boundary-layer assumptions the momentum, energy, and concentration equations are reduced to the form (for an axially-symmetric flow):

$$v_r \frac{\partial v_r}{\partial r} - \frac{v_\phi^2}{r} + v_z \frac{\partial v_r}{\partial z} = -\frac{1}{\rho} \frac{\partial p}{\partial r} + \nu \frac{\partial^2 v_r}{\partial z^2}, \quad (1.7)$$

$$v_r \frac{\partial v_\phi}{\partial r} + \frac{v_r v_\phi}{r} + v_z \frac{\partial v_\phi}{\partial z} = \nu \frac{\partial^2 v_\phi}{\partial z^2}, \quad (1.8)$$

$$v_r \frac{\partial T}{\partial r} + v_z \frac{\partial T}{\partial z} = \alpha \frac{\partial^2 T}{\partial z^2}, \quad (1.9)$$

$$v_r \frac{\partial C}{\partial r} + v_z \frac{\partial C}{\partial z} = D \frac{\partial^2 C}{\partial z^2}. \quad (1.10)$$

These simplified equations are still coupled, non-linear partial differential equations. However, they are now of parabolic nature instead of elliptic one (as the original system ((1.1) – (1.6) was).

1.10 Boundary-layer equations for sinusoidal disk

Consider a non-flat, axially-symmetric circular disk having radius b rotating around its vertical axis with a constant rotation rate ω . The disk is assumed to rotate in a fixed frame due to which the Coriolis force is absent and the flow resembles to the classical von Kármán's flow. Such a rotating flow is assumed to be steady, viscous, incompressible, with constant thermo physical properties inside and away from the boundary-layer. The effects of viscous dissipation and gravity are also neglected. The

disk surface is structured (as depicted in Fig. 1.4) by the function $s(r^*) = a_0 \cos(2N\pi r^*)$, which specifies the non-flat surface of the disk as sinusoidal wavy surface as considered by Le Palec [71]. It is important to define the ratio (a_0/λ) known as the surface roughness ratio which controls the surface topography of the disk. To avoid the flow separation and the occurrence of secondary flow the roughness ratio is kept small ($a_0/\lambda \leq 0.2$) with the restriction that ($\delta \ll \lambda$) so that the governing system (given below) remains valid. The so chosen surface topography is not mandatory rather one is free to choose any other form. The reason behind the choice of current sinusoidal wavy surface is that it is a smooth differentiable function which is also of periodic nature. All these features of this sinusoidal function provide an ease during the computation process. Furthermore, this shape allows the current results to be compared with those reported by Le Palec [71]. After having the little surface undulations sprouted on the flat disk surface it is useful to choose an appropriate system of coordinates for its mathematical description. For this purpose the governing equations are derived in terms of an orthogonal curvilinear coordinate system (x, θ, y) in which the direction along the wavy surface of the disk is represented by x and normal to the surface is y while the azimuthal direction is described by θ (see Fig. 1.4).

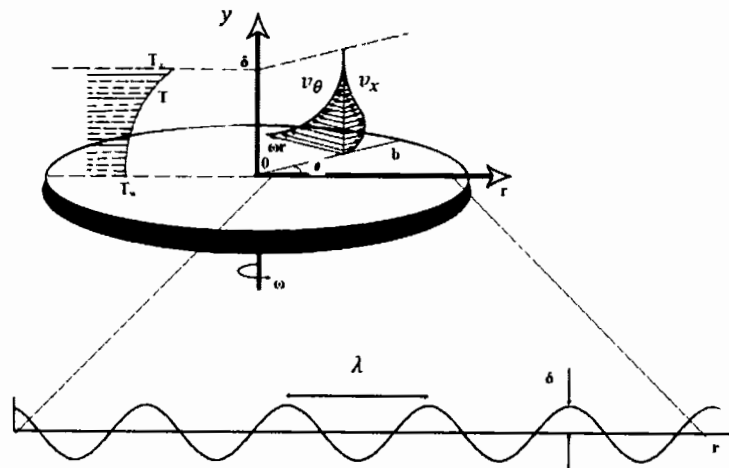


Fig. 1.4: Configuration of wavy disk.

In view of above assumptions the considered flow is axially symmetric and three-dimensional in nature. In accordance with the chosen system of coordinates the equation of continuity reads as

$$v_x \frac{\partial v_x}{\partial x} + \frac{\partial v_y}{\partial y} + \frac{v_x}{r} \frac{dr}{dx} = 0. \quad (1.11)$$

The Navier-Stokes equations after the implementation of boundary-layer approximations look like

$$v_x \frac{\partial v_x}{\partial x} + v_y \frac{\partial v_x}{\partial y} - \frac{v_\theta^2}{r} \frac{dr}{dx} = -\frac{1}{\rho} \frac{\partial p}{\partial x} + \nu \frac{\partial^2 v_x}{\partial y^2}, \quad (1.12)$$

$$v_x \frac{\partial v_\theta}{\partial x} + v_y \frac{\partial v_\theta}{\partial y} + \frac{v_x v_\theta}{r} \frac{dr}{dx} = \nu \frac{\partial^2 v_\theta}{\partial y^2}. \quad (1.13)$$

The appearance of the coefficient $\frac{dr}{dx}$ with some terms in Eqs. (1.11) – (1.13) signifies the contribution of surface curvature. In view of the definition of disk surface, defined above, the coefficient $\frac{dr}{dx}$ is determined as

$$\frac{dr}{dx} = \sqrt{1 + 4 \frac{a_0^2 \pi^2}{\lambda^2} \sin^2 \left(\frac{2N\pi r}{b} \right)}.$$

The energy equation for this flow comes out to be

$$v_x \frac{\partial T}{\partial x} + v_y \frac{\partial T}{\partial y} = \alpha \frac{\partial^2 T}{\partial y^2}, \quad (1.14)$$

which is apparently same as Eq. (1.9). However, the variables are not the same in these equations. In accordance with the energy equation the concentration equation is also of the form (1.14) and is given by

$$v_x \frac{\partial C}{\partial x} + v_y \frac{\partial C}{\partial y} = D \frac{\partial^2 C}{\partial y^2}. \quad (1.15)$$

1.11 Solution techniques

Unfortunately, the equations arising in the analyses of the flow and heat or mass transfer in a rotating disk system are highly non-linear and a complex set of *pdes* (partial differential equations) and their exact solution is not possible. For the reduction of complexity of the governing system, these equations were converted into a simpler form using the boundary-layer transformations. Their further simplified form would either comprised of self-similar (set of *odes*) or non-similar system (set of *pdes*). The self-similar problems lead to the boundary value problems comprising of *odes* (ordinary differential equations) which can be tackled easily with the help of numerical methods such as shooting, finite difference, etc. The handling of such problems has also been made easy with the availability of high speed computing machines along with several D-solve Packages in different softwares like MATHCAD, MATLAB, MATHEMATICA, MAPLE, COMSOL, etc. On the other hand, a non-similar system involves a set of *pdes* whose solution is not that easy. However such system can be

dealt efficiently and easily with the implicit finite difference scheme commonly known as Keller-box method. In the current research work both self-similar and non-similar systems have been solved with the employment of different numerical techniques which are mentioned in the following.

1.11.1 The *bvp4c* algorithm

The *bvp4c* is a built-in MATLAB program of finite difference method (uses three stage Lobatto formula) and is developed by Kierzenka and Shampine [84] in 2001 for finding the numerical solution of boundary value problems. It has a low storage and computational cost with the advantage of adaptive meshes which leads to high precision. Due to this it is more consistent and robust than other numerical techniques. The highly non-linear terms that arise in boundary value problems (like terms arising in **Chapter 2**) can easily be managed by this algorithm while the remaining methods offer more difficulty when these are implemented to the system of *odes* described in **Chapter 2**. Similar to other numerical techniques, it also depends on initial guess and it may fail for the poor initial guesses.

1.11.2 The shooting method

The shooting method is also a boundary value problem solving technique by converting it into initial value problem. This method starts with a guessed initial condition and it is refined with several iterations until a solution is obtained satisfying all the boundary conditions. It is also a very robust method and is applicable to a variety of scientific and engineering problems. For instance, problem arising in mathematical modelling of rotating disk-cone system (**Chapter 4**) cannot be solved by *bvp4c* but the shooting method is easily implemented with the usage of MATHCAD software to acquire the solution.

1.11.3 The Keller-box Method

All the non-similar problems have been dealt with the help of Keller-box method which is quite efficient and specifically designed for the boundary-layer flow problems. Keller [85] was the pioneer who introduced this box method in 1970 which is commonly named as Keller-box method or Preissman box scheme. The method is described in few steps which are listed below:

Step1: In this step by introducing new functions higher order differential equations are reduced to a system of first order differential equations.

Step2: The derivatives are replaced by central difference approximation, and the functions by their average value on rectangular net. After discretization one obtain a system of nonlinear or linear algebraic equations.

Step3: Newton's method is employed in order to linearize the non-linear algebraic equations.

Step4: The set of linear equations is written in a tri-diagonal matrix form and is solved by the block-elimination or LU-decomposition method.

The main features of this method are:

- As compared to other implicit methods it is slightly more arithmetic
- It can work out with arbitrary spacing of space coordinates
- Its accuracy is of second order
- This method allows very swift x -variations
- Due to this technique (by simple programming) mixed (coupled) problems can be solved with a great ease
- It is specially developed for the boundary-layer flows

CHAPTER 2

Heat Transfer Enhancement in Rotating Disk Boundary-Layer using Nanofluid

A generally admitted fact about nanofluids is the expedition of heat transfer process in comparison to pure fluids. The calculation of enhanced rate of heat transfer depends strongly upon the nanofluid modeling. Following the experimental evidences most of the researchers assume the nanofluid to be a homogeneous mixture. However, this is a severe condition that results in under prediction of heat transfer rate. Due to the ongoing convection phenomena the nanoparticle concentration is actually non-homogeneous within the boundary-layer because of the presence of concentration gradients. The objective of this **Chapter** is to calculate the heat transfer enhancement in three-dimensional boundary-layer when the working fluid is a nanofluid. The rotating disk geometry, which perhaps serves as the bench mark for the three-dimensional boundary-layers, have been chosen for the purpose here. The non-homogeneous nanofluid modeling has been utilized and percent increase in Nusselt number has been calculated. Detailed analyses of flow and heat transfer phenomena for nanofluid have been conducted under the influence of several physical parameters.

2.1 Mathematical formulation

2.1.1 Nanofluid modeling

Consider a mixture of a pure fluid and metallic particles of nanosize in it. The concentration of nanoparticle in the base fluid is fixed and is denoted by ϕ_{∞} . The presence of nanoparticles in the base fluid alters the material properties of the mixture such as viscosity, density and thermal conductivity. Because of the diverse nature of nanofluid with regard to the nature, size, shape, and concentration of the nanoparticle within the base fluid, it is quite hard to propose a single model for every such property which would be applicable everywhere in general. So far, the theory and experiment have not been succeeded in doing so. Consequently, there exist several empirical and theoretical models for the description of effective viscosity, density and thermal heat capacity of the nanofluid. These models have their own merits and demerits within the limited domain of applicability. For example, a list of several models, based on theory and experiment, for the effective viscosity of nanofluid is given in a nice book by

Minkowycz et al. [86]. Most of the models have particularly been developed for nanoparticle of spherical shape. The spherical shaped nanoparticle with no intra interaction are usually preferred where the nanoparticles are required to behave, to some extent, as the fluid particles. Einstein [87] introduced the simplest model for effective viscosity of the nanofluid by using the hydrodynamic equations, where the nanoparticle volume fraction was limited to 2% only, in the form

$$\mu = (1 + 2.5\phi)\mu_f. \quad (2.1)$$

The Einstein's model (2.1) was further improved by Brinkman [88], Batchelor [89] and Lundgren [90] in order to extend it to high-moderate concentration or to incorporate the Brownian motion effects. Lundgren [90] simply assumed the Einstein's model as the first two terms of the Taylor series expansion of the form

$$\mu = (1 - 2.5\phi)^{-1}\mu_f = (1 + 2.5\phi + 6.25\phi^2 + \dots)\mu_f, \quad (2.2)$$

and proposed the consideration of the complete series (2.2) instead of the first two terms. The model is, however, still limited to the dilute suspension of nanoparticle. The Batchelor's model [89] improves the Einstein's one by including a one more term of the Taylor series (2.2) whose coefficient is taken as 6.2 instead of 6.25 as in Eq. (2.2). This model is actually based on the reciprocal theorem of Stokes flow and includes the effects of Brownian motion. The Brinkman model [88] also considers the Taylor series of the form

$$\mu = (1 - 2.5\phi)^{-2/5}\mu_f, \quad (2.3)$$

whose first two terms also cover the Einstein's model. This model is applicable to the moderate and high concentration of the nanoparticle. In addition to these, there are several other nanofluid models for effective viscosity which are though limited to the spherical shaped nanoparticle but also include the radius of the spherical particles with some other restrictions. However, literature is not limited to the spherical shaped nanoparticle but also includes some other shapes such as cylinder, cone, brick, etc. Despite the presence of all such theoretical models the literature is also quite rich in the empirical models of the effective viscosity based wholly on the experimental data. Although, the empirical models are quite exact and have the capacity of predicting the very true results, but the problem with such models is that they are very limited in scope and apply only to those particular situations for which the corresponding experimental data have been collected. While in the theoretical analysis, as conducted in the current study, one is more inclined towards the general analysis of heat and mass transport

phenomena in order to make a general qualitative analysis of the whole process. On these basis the theoretical models are usually being preferred having wider scope of applicability with some compromise on the qualitative measurements. Another aspect which is somehow more preferred by the theoretical analysts is the mathematical simplification of the chosen models. In the current analysis we choose to assume the spherical shape of nanoparticle and the moderate range for nanoparticle concentration. Owing to these properties and the mathematical ease the Brinkman model is observed to be the appropriate for current analysis. The effective density of the nanofluid based on the physical rule of mixture is given by

$$\rho = (1 - \phi)\rho_f + \phi\rho_p, \quad (2.4)$$

which also shows an excellent agreement with the experiment. Maxwell [91] was the first to derive the effective thermal conductivity of the solid-liquid mixture and proposed that

$$k = k_f \left[\frac{k_p + 2k_f + 2\phi(k_p - k_f)}{k_p + 2k_f - \phi(k_p - k_f)} \right], \quad (2.5)$$

which is applicable to the moderate concentration levels. The formula (2.5) was extended to high concentration nanofluid by Bruggeman [92] in the form

$$k = k_f \left[\frac{(3\phi - 1)\frac{k_p}{k_f} + 3(1 - \phi) - 1 + \sqrt{\Delta}}{4} \right]; \quad \Delta = \left[\frac{(3\phi - 1)k_p}{k_f} + 3(1 - \phi) - 1 \right]^2 + 8\frac{k_p}{k_f},$$

which readily reduces to the Maxwell's one for the case of moderate concentration. The thermal heat capacity of the nanofluid based on the analytical model reads as

$$\rho c = (1 - \phi)(\rho c)_f + \phi(\rho c)_p. \quad (2.6)$$

It has been shown by Minkowycz et al. [86] that the expansion (2.6) finds an excellent agreement with the experimental data. The Brownian motion diffusion coefficient and thermophoresis parameters are given by

$$D_B = \frac{k_B T}{3\pi\mu a_p}, \quad D_T = \beta v \phi, \quad (2.7)$$

where β stands for thermal expansion and has the following form

$$\beta = (1 - \phi)\beta_f + \phi\beta_p. \quad (2.8)$$

An alternative definition of β is also available in literature with a certain modified form, given as

$$\rho\beta = (1 - \phi)(\rho\beta)_f + \phi(\rho\beta)_p. \quad (2.9)$$

In comparison to the experimental data both definitions of β do not find a good agreement; a poor approximation due to Eqs. (2.8) & (2.9) can, however, not be denied.

However, it has also been observed that the selection of (2.8) or (2.9) does not harm the results of skin friction and Nusselt number by any large. Staying on equal footing regarding the experimental data, Eqs. (2.8) or (2.9) are equally valid with Eq. (2.8) having an edge of mathematical simplicity.

2.1.2 Mathematical model

Consider a uniform flat disk resting at $z = 0$ in three dimensional space. The disk is surrounded by the non-homogeneous nanofluid. The disk rotates about the z – axis with an angular speed ω . The disk temperature is fixed as T_w where the ambient temperature is assumed to be T_∞ such that $T_w < T_\infty$. A schematic of the flow is shown in Fig. 2.1.

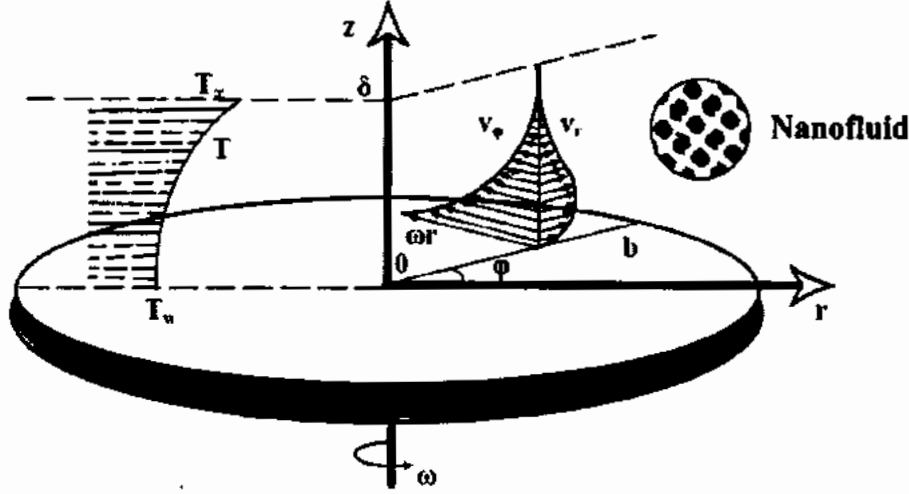


Fig. 2.1: Flow geometry.

The symmetry of flow geometry requires the consideration of cylindrical coordinates for further analysis. In this way the conservation laws (1.1) – (1.4) (under the assumption of steady and axially-symmetric flow) have been implemented (with modified thermophysical properties). The enthalpy and the concentration equations for the non-homogeneous model read as

$$\rho \left(v_r \frac{\partial h_e}{\partial r} + v_z \frac{\partial h_e}{\partial z} \right) = \frac{\partial}{\partial z} \left(k \frac{\partial T}{\partial z} \right) + \rho_p c_p \left(D_B \frac{\partial \phi}{\partial z} \frac{\partial T}{\partial z} + \frac{D_T}{T} \left(\frac{\partial T}{\partial z} \right)^2 \right), \quad (2.10)$$

$$v_r \frac{\partial \phi}{\partial r} + v_z \frac{\partial \phi}{\partial z} = \frac{\partial}{\partial z} \left(D_B \frac{\partial \phi}{\partial z} + \frac{D_T}{T} \frac{\partial T}{\partial z} \right), \quad (2.11)$$

and the relative boundary data is given by:

at the disk surface ($z = 0$)

$$v_r = v_z = v_\phi - r\omega = 0, h_e - h_{ew} = 0, T - T_w = 0, \left(D_B \frac{\partial \phi}{\partial z} \right)_{z=0} + \left(\frac{D_T}{T} \frac{\partial T}{\partial z} \right)_{z=0} = 0, \quad (2.12)$$

at ambient locations ($z = \infty$)

$$v_r = v_\varphi = 0, h_e - h_{e\infty} = 0, T - T_\infty = 0, \phi = \phi_\infty. \quad (2.13)$$

2.2 Self-similar form of equations

Similar to the classical von Kármán flow, the considered nanofluid flow induced by the disk rotation does also admits a solution in the separable form given by

$$v_r = rf(z), v_\varphi = rg(z), v_z = h(z), p = p(z), h_e = h_e(z), \phi = \phi(z). \quad (2.14)$$

The non-dimensional variables are constructed (with the help of Buckingham Pi Theorem)¹ as

$$\left. \begin{aligned} \eta = z \sqrt{\frac{\omega}{v_f}}, f = \omega F(\eta), g = \omega G(\eta), h = \sqrt{v_f \omega} H(\eta), p = \rho_f v_f \omega P(\eta), h_e = h_{e\infty} H_e(\eta), \\ \phi = \Phi(\eta) \end{aligned} \right\} \quad (2.15)$$

The combination of Eqs. (2.14) and (2.15) is used to obtain the self-similar variables. Since the continuity equation involves variable density therefore the consideration of flow rates (instead of velocities only) is a convenient choice [47]. Keeping this fact in mind we write

$$\rho v_r = \rho_\infty r \omega F(\eta), \rho v_\varphi = \rho_\infty r \omega G(\eta), \rho v_z = \rho_\infty \sqrt{v_f \omega} H(\eta). \quad (2.16)$$

Also the variable nature of thermophysical properties of nanofluid which depend upon concentration or temperature is described as

$$\rho = \rho(\phi), \mu = \mu(\phi), D_B = D_B(T), D_T = D_T(\phi), c = c(\phi), k = k(\phi). \quad (2.17)$$

The utilization of Eqs. (2.14) – (2.17) into the system (1.1) – (1.4) and Eqs. (2.10)–(2.11) results in the transformed self-similar form of the governing equations, given by

$$H' + 2F = 0, \quad (2.18)$$

$$\begin{aligned} M \left(F'' - \frac{2}{R} F' \Phi' R' + F \left(\Phi'^2 \left(2 \left(\frac{R'}{R} \right)^2 - \frac{R''}{R} - \Phi'' \frac{R'}{R} \right) \right) \right) + (M' \Phi' - \bar{\rho} H) \left(F' - \right. \\ \left. F \Phi' \frac{R'}{R} \right) - \bar{\rho} (F^2 - G^2) = 0, \end{aligned} \quad (2.19)$$

$$\begin{aligned} M \left(G'' - 2G' \Phi' \frac{R'}{R} + G \left(\Phi'^2 \left(2 \left(\frac{R'}{R} \right)^2 - \frac{R''}{R} - \Phi'' \frac{R'}{R} \right) \right) \right) + (M' \Phi' - \bar{\rho} H) \left(G' - \right. \\ \left. G \Phi' \frac{R'}{R} \right) - 2\bar{\rho} FG = 0, \end{aligned} \quad (2.20)$$

¹ However this construction of dimensionless group is not unique.

$$M \left(H'' - 2H'\Phi' \frac{R'}{R} + H \left(\Phi'^2 \left(2 \left(\frac{R'}{R} \right)^2 - \frac{R''}{R} - \Phi'' \frac{R'}{R} \right) \right) \right) + (M'\Phi' - \bar{\rho}H) \left(H' - H\Phi' \frac{R'}{R} \right) - \frac{P'}{R} = 0, \quad (2.21)$$

$$KH_e'' + H_e' \left(-\bar{\rho}PrH \frac{RC}{R} + \Phi' \left(K' + \frac{1}{Le} + 2 \left(\frac{R'}{R} - \frac{RC'}{RC} \right) \left(K + \frac{\bar{D}}{Le} \right) \right) + H_e \left(\left(\frac{R'}{R} - \frac{RC'}{RC} \right) \left(K\Phi'' + \Phi'^2 \left(\frac{1}{Le} + K' \right) \right) + \Phi'^2 \left(\bar{D} \left(\frac{R'}{R} - \frac{RC'}{RC} \right)^2 + K \left(2 \frac{RC'^2}{RC^2} - 2 \frac{R'RC'}{RRC} + \frac{R''}{R} - \frac{RC''}{RC} \right) \right) \right) + \frac{\bar{D}}{Le} \frac{H_e'^2}{H_e} = 0, \quad (2.22)$$

$$\Phi'' \left(1 + \bar{D} \left(\frac{R'}{R} - \frac{RC'}{RC} \right) H_e \right) + \Phi' \left(\frac{H_e'}{D_B} \left(\frac{D_T'}{H_e} + D_B' \right) - \frac{\bar{D}}{R} ScH \right) + \Phi'^2 \left(\left(\frac{R'}{R} - \frac{RC'}{RC} \right) \left(\frac{D_B'}{D_B} H_e + \frac{D_T'}{D_B} \right) + \bar{D} \left(\frac{RC'^2}{RC^2} - \frac{R'^2}{R^2} + \frac{R''}{R} - \frac{RC''}{RC} \right) \right) + \bar{D} \left(\frac{H_e''}{H_e} - \frac{H_e'^2}{H_e^2} \right) = 0, \quad (2.23)$$

where $M(\Phi) = (1 - \Phi)^{\frac{-5}{2}}$, $R(\Phi) = (1 - \Phi) + \Phi \frac{\rho_p}{\rho_f}$, $\bar{\rho} = \frac{\rho_\infty}{\rho_f}$, $K(\Phi) = \frac{k_p + 2k_f + 2\Phi(k_p - k_f)}{k_p + 2k_f - \Phi(k_p - k_f)}$,
 $Pr = \frac{\mu_f c_f}{k_f}$, $RC(\Phi) = (1 - \Phi) + \Phi \frac{\rho_c p}{\rho_c f}$, $\bar{D} = \frac{D_T}{D_B}$, $Sc[H_e(\eta)] = \frac{\mu_f}{\rho_f D_B}$, $Le[H_e(\eta)] = \frac{Sc[H_e(\eta)] (\rho c)_f}{Pr (\rho c)_p}$. (2.24)

In the above equations F', G', H', H_e' and Φ' mean differentiation with respect to η , R', RC', M', K' and D_T' represent the derivative with regard to Φ , and D_B' denotes the derivative with respect to T . From Eq. (2.24) it is observed that the Prandtl number depends on pure fluid properties only.

The self-similar form of boundary data given in Eqs. (2.12) and (2.13) read as

$$\left. \begin{aligned} \eta = 0: F = G - \frac{R(\Phi_w)}{\bar{\rho}} = H = P = 0, H_e = \frac{h_{ew}}{h_{e\infty}}, \frac{H_e}{H_e'} = \Phi' \left(\frac{RC'}{RC} - \bar{D} \right) \\ \eta = \infty: F = G = H_e - 1 = \Phi - \phi_\infty = 0 \end{aligned} \right\} \quad (2.25)$$

The ratio $h_{ew}/h_{e\infty}$ in the above equation is accommodated by the replacement of enthalpy by temperature in energy Eq. (2.10). In doing so, the specific heat capacity of the nanofluid is also kept uniform c_∞ which is a valid assumption [47] and especially holds for large values of the Schmidt number, which is a characteristic of flow of nanoparticle. Further D_B and D_T are also taken as constant, and constant temperature equals to T_∞ in the denominator of last term in Eqs. (2.10) and (2.11). Under these assumptions Eqs. (2.10) and (2.11) are must be simplified to the following form:

$$K\theta'' + \theta' \left(\frac{D}{Le} \theta' + \frac{\Phi'}{Le} + K'\Phi' - \bar{\rho}PrH \right) = 0, \quad (2.26)$$

$$\Phi'' - \frac{\bar{\rho}}{R} ScH\Phi' + D\theta'' = 0, \quad (2.27)$$

where $\theta(\eta) = \frac{T-T_w}{T_\infty-T_w}$, $Le = \frac{Sc \rho_f c_\infty}{Pr \rho_p c_p}$ and $D = \frac{T_\infty-T_w D_T}{T_\infty D_B}$.

The boundary conditions simplify to the form

$$\left. \begin{aligned} \eta = 0: F = G = \frac{R(\phi_w)}{\bar{\rho}} = H = P = \theta = D\theta' + \Phi' = 0 \\ \eta = \infty: F = G = \theta - 1 = \Phi - \phi_\infty = 0 \end{aligned} \right\} \quad (2.28)$$

2.2.1 Numerical solution

The numerical solution of the reduced boundary-layer equations (2.18) – (2.21), and (2.26) – (2.28) is acquired through the famous computing tool MATLAB in which built in scheme bvp4c is used. The convergence of the solution is assured after several runs under the default tolerance level of 10^{-4} . The present numerical procedure has been checked by solving the system of self-similar equations for pure fluid. Table 2.1 gives the comparison of the current numerical solution with that reported by Shevchuk [37]. An excellent match to four decimal places can easily be seen in this Table. This authenticates our program and permits for the solution of current equations.

Table 2.1: The comparison between current results and Shevchuk [37].

<i>Pr</i>	$\theta'(0)$		$F'(0)$		$G'(0)$	
	Shevchuk [37]	Present	Shevchuk [37]	Present	Shevchuk [37]	Present
0.10	0.0766	0.0766	0.5102	0.5102	-0.6159	-0.6159
1.00	0.3969	0.3969	0.5102	0.5102	-0.6159	-0.6159
10.0	1.1341	1.1341	0.5102	0.5102	-0.6159	-0.6159
13.0	1.2579	1.2579	0.5102	0.5102	-0.6159	-0.6159

2.3 Results and discussion

The impact of nanofluid on heat transfer rate has been understood by the detailed analysis of the involved parameters namely, ϕ_∞ , D , Sc , and Pr . A strong convective heat transfer in rotating disk boundary-layer is found when ϕ_∞ is varied from 0.0 to 0.4 at a fixed Prandtl number ($Pr = 6$) and diffusion parameter ($D = 0.05$). The Schmidt number (Sc) is also varied for a wide range (10 – 1000) and is suitable for the base fluid to be a liquid. The insertion of nanoparticles in the base fluid have also strong impact on the momentum transport across the boundary-layer. The influence of Schmidt number on all components of velocity and pressure is depicted in Figs. 2.2 &

2.3. Clearly, the influence of Sc is very weak on all the velocity components and slightly stronger on pressure. Pressure decreases within the boundary-layer by increasing the values of Sc .

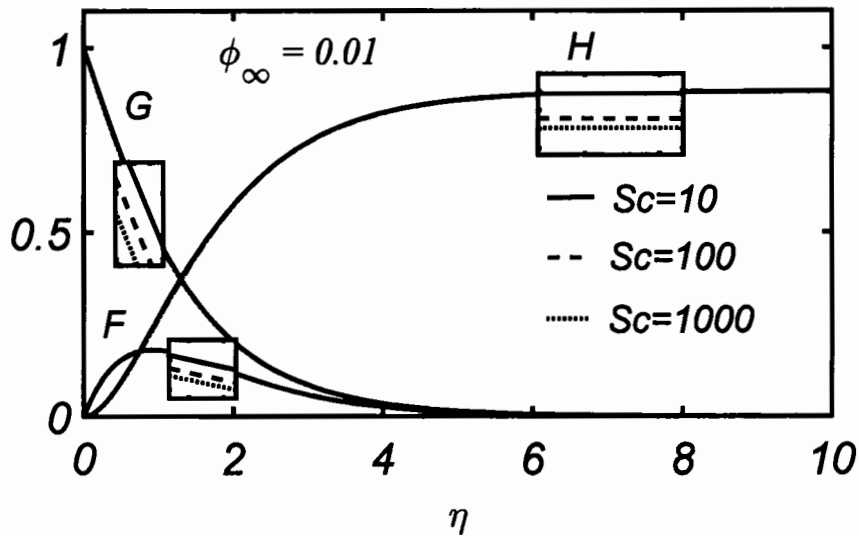


Fig. 2.2: Radial, transverse and axial components of velocity for different Sc .

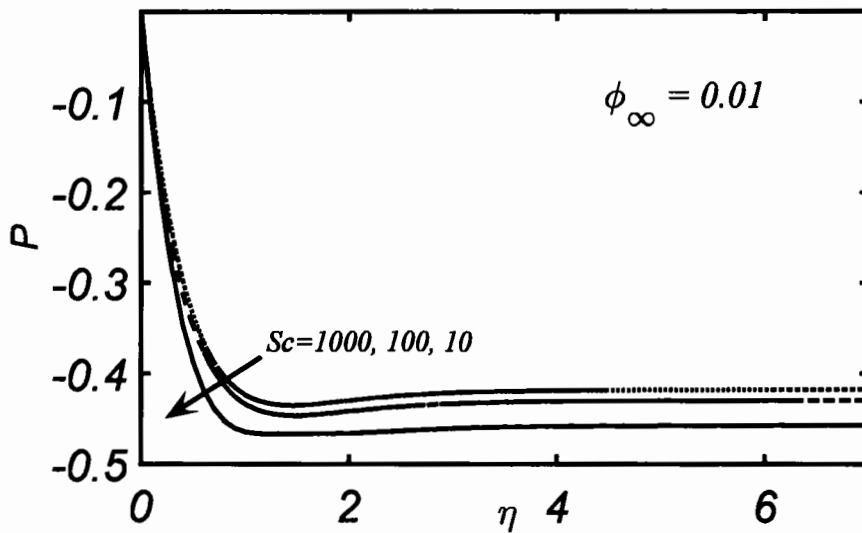


Fig. 2.3: Effects of Sc on pressure profile.

Similarly the temperature profiles are not affected by changing the values of Sc parameter as shown in Fig. 2.4. However strong dependence of the concentration profile on Sc can be seen in Fig. 2.5. Clearly, concentration boundary-layer thickness decreases by increasing Sc number which reflects that the large values of Sc depreciate the mass transport phenomena across the boundary-layer and limit it to a very thin near-wall

region. In comparison with momentum boundary-layer thickness, the concentration boundary-layer makes about 10% of the momentum boundary-layer which means that over the most part of the momentum boundary-layer the nanoparticle concentration is uniform and is varying rapidly in the region close to the rotating disk. This is the reason that large values of Sc correspond to weak Brownian diffusion of nanoparticles. In such a situation nanofluid behaves more or less as a homogenous mixture. Therefore simulation of transport processes with a homogeneous mixture is justified for situations where Sc accepts large values.

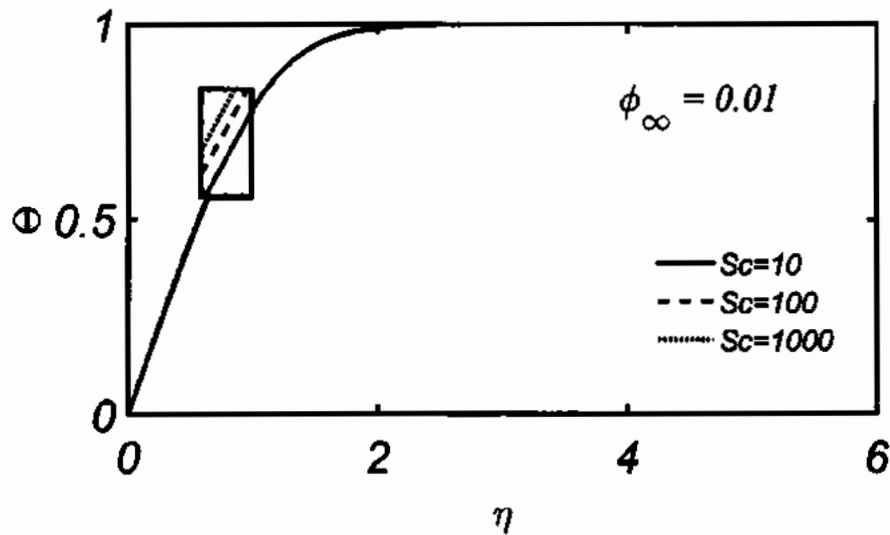


Fig. 2.4: Temperature profile for different Sc .

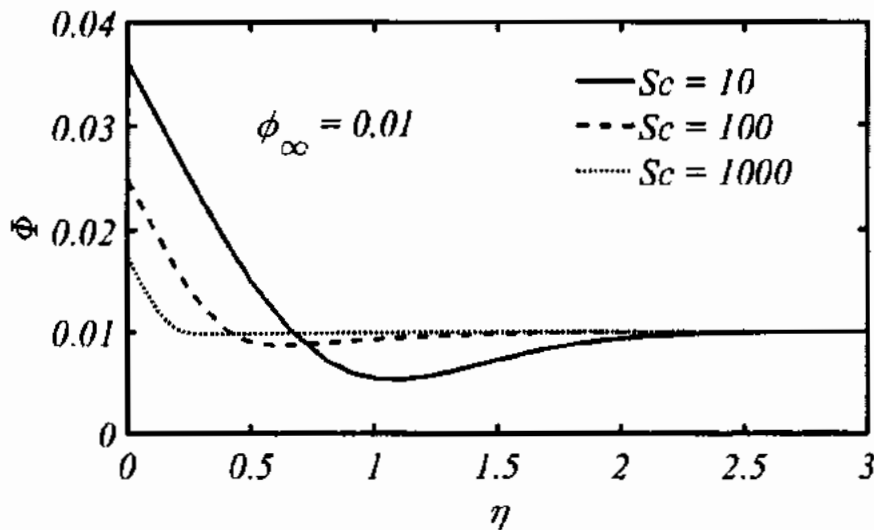


Fig. 2.5: Concentration profile for different Sc .

Figures 2.6 & 2.7 depict the effects of nanoparticle concentration ϕ_∞ on velocity components, temperature, and pressure. It is clearly seen that all the velocity components are increased by increasing ϕ_∞ . Moreover increase in the level of nanoparticle concentration leads to increase the boundary-layer thickness also which means that the momentum transport is enhanced across the boundary-layer with the insertion of nanoparticle in the base fluid. An interesting role of nanoparticle concentration on the rotating disk boundary-layer is highlighted in Fig. 2.6 showing the enhancement in the downward axial velocity due to the increasing level of nanoparticle concentration. Hence this tends to enhance the mass flux which ultimately supports the heat transfer augmentation. This behavior can also be seen from Table 2.2 in which the relative mass flow rate is increased with increasing the nanoparticle concentration and consequently the Nusselt number is also enhanced. The definitions of relative mass flow rate and some other dimensionless physical parameters such as relative moment coefficient, relative displacement thickness, relative tangent of the flow swirl angle, and the relative Nusselt number are given as

$$\frac{\dot{m}_d}{\dot{m}_{d0}} = \frac{\rho \int_{z=0}^{\infty} v_r dz}{\rho_f \int_{z=0}^{\infty} v_{r0} dz}, \quad \frac{C_m}{C_{m0}} = \frac{\rho \int_0^b r^2 \tau_{z\phi} dr}{\rho_f \int_0^b r^2 \tau_{z\phi_0} dr}, \quad \frac{\delta^*}{\delta_0^*} = \frac{\int_{z=0}^{\infty} v_\phi dz}{\int_{z=0}^{\infty} v_{\phi_0} dz},$$

$$\frac{\alpha_w}{\alpha_{w0}} = \frac{[\partial v_r / \partial z / \partial v_\phi / \partial z]_{z=0}}{[\partial v_{r0} / \partial z / \partial v_{\phi_0} / \partial z]_{z=0}}, \quad \frac{Nu}{Nu_0} = \frac{[\partial T / \partial z]_{z=0}}{[\partial T_0 / \partial z]_{z=0}}.$$

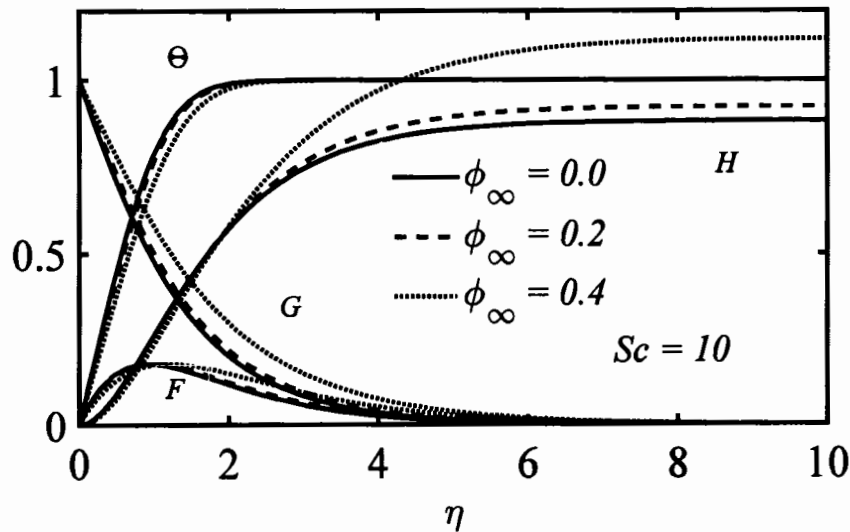


Fig. 2.6: Radial, transverse and axial component of velocity and temperature profiles.

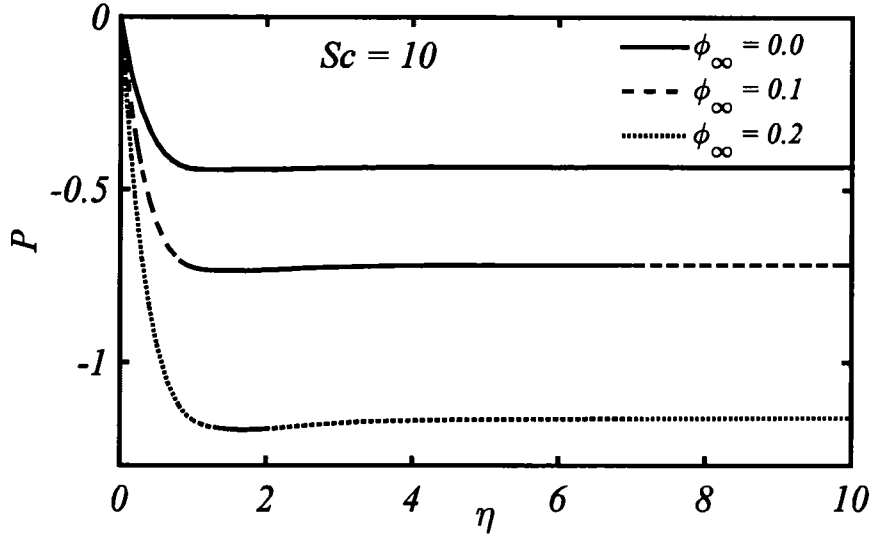


Fig. 2.7: Effects of ϕ_∞ on pressure profile.

The calculation of tangent of flow swirl angle and moment coefficient have also been displayed in Table 2.2 for different values of ϕ_∞ and Sc . These results are in fact very useful and emphasize the significance of non-uniform distribution of nanoparticles across the boundary-layer. An increase in the values of relative Nusselt number is clearly observed in this Table by increasing nanoparticle concentration but it (relative Nusselt number) decreases upon increasing Sc for a fixed nanoparticle concentration. Moreover, the rate of increase of relative Nusselt number (Nu/Nu_0) regarding nanoparticle concentration (ϕ_∞) is higher for the smaller Schmidt number than that of higher Schmidt number. The reason behind this fact is that at smaller values of the Schmidt number the impact of non-homogeneous distribution of nanoparticle on heat transfer rate is strong whereas this character (non-homogeneous) is weaker at the larger values of Schmidt number for which the nanoparticle concentration becomes uniform in most part of the momentum boundary-layer. Here one can realize the significance of current non-homogeneous modelling of nanofluid which in fact correctly incorporates the role of Brownian motion of nanoparticles towards the momentum and thermal transport. It is also observed from Table 2.2 that moment of a rotating disk is significantly influenced by ϕ_∞ meaning that power of rotating disk system gets increased when the working fluid is nanofluid. The influence of nanoparticle concentration parameter ϕ_∞ on temperature profile is displayed in Fig. 2.6. The thermal boundary-layer grows in the same fashion as the momentum boundary-layer for higher values of ϕ_∞ . The parameters Nu/Nu_0 , C_m/C_{m_0} , α_w/α_{w_0} and \dot{m}_d/\dot{m}_{d_0} are depicted in Figs. 2.8 – 2.11 against the nanoparticle concentration. A linear (almost) correlation

occurs between Nu/Nu_0 and ϕ_∞ but non-linear for C_m/C_{m0} . The nonlinearity is more prominent for the 20% or higher concentration level of nanoparticles (i.e. $\phi_\infty > 0.2$). The relative values of tangent of the flow swirl angle (α_w/α_{w0}) are weak function of nanoparticle concentration but these values are higher for nanofluid than the pure fluid. A non-linear correlation is also owned by the relative mass flow rate (\dot{m}_d/\dot{m}_{d0}) with nanoparticle concentration ϕ_∞ but the nonlinearity weakens as the concentration level grows. The values of Nu/Nu_0 , C_m/C_{m0} , α_w/α_{w0} , \dot{m}_d/\dot{m}_{d0} and δ^*/δ^*_0 are quantized in Tables 2.2 – 2.5 for specific values of Sc, D, Pr and ϕ_∞ . Form Table 2.2, it is noticed that the relative Nusselt number, the tangent of the flow swirl angle, moment coefficient, mass flow rate and displacement thickness are increased on increasing the nanoparticle concentration ϕ_∞ . The values of all these parameters decrease by increasing the value of Sc .

Table 2.2: Impact of nanoparticle concentration and Schmidt number on relative values of vital physical parameters for $Pr = 6, D = 0.05, \frac{\rho_p}{\rho_f} = 3.98195$.

ϕ_∞	0	0.01	0.1	0.15	0.2	0.3	0.4
$Sc = 10 (Nu/Nu_0)_{Le \rightarrow \infty}$	1	1.0537	1.3341	1.5001	1.6746	2.0528	2.4780
$(Nu/Nu_0)_{Le}$	1	1.0558	1.3368	1.5032	1.6781	2.0570	2.4828
C_m/C_{m0}	1	1.0418	1.3166	1.4925	1.6903	2.1744	2.8344
α_w/α_{w0}	1	1.0380	1.0356	1.0350	1.0348	1.0353	1.0369
\dot{m}_d/\dot{m}_{d0}	1	1.1084	1.3813	1.5569	1.7548	2.2417	2.9080
δ^*/δ^*_0	1	1.0060	1.0102	1.0284	1.0570	1.1481	1.2959
$Sc = 50 (Nu/Nu_0)_{Le \rightarrow \infty}$	1	1.0391	1.3184	1.4839	1.6579	2.0350	2.4594
$(Nu/Nu_0)_{Le}$	1	1.0400	1.3196	1.4852	1.6593	2.0367	2.4614
C_m/C_{m0}	1	1.0329	1.3060	1.4809	1.6775	2.1586	2.8148
α_w/α_{w0}	1	1.0230	1.0215	1.0210	1.0207	1.0206	1.0209
\dot{m}_d/\dot{m}_{d0}	1	1.0836	1.3564	1.5317	1.7292	2.2139	2.8766
δ^*/δ^*_0	1	1.0025	1.0065	1.0242	1.0522	1.1420	1.2020
$Sc = 100 (Nu/Nu_0)_{Le \rightarrow \infty}$	1	1.0355	1.3146	1.4800	1.6539	2.0311	2.4557
$(Nu/Nu_0)_{Le}$	1	1.0361	1.3153	1.4808	1.6548	2.0322	2.4570
C_m/C_{m0}	1	1.0308	1.3036	1.4781	1.6745	2.1550	2.8104
α_w/α_{w0}	1	1.0173	1.0162	1.0158	1.0155	1.0153	1.0153
\dot{m}_d/\dot{m}_{d0}	1	1.0740	1.3464	1.5212	1.7184	2.2016	2.8622
δ^*/δ^*_0	1	1.0014	1.0051	1.0226	1.0506	1.1400	1.2854
$Sc = 1000 (Nu/Nu_0)_{Le \rightarrow \infty}$	1	1.0306	1.3097	1.4751	1.6491	2.0267	2.4522
$(Nu/Nu_0)_{Le}$	1	1.0307	1.3098	1.4753	1.6493	2.0269	2.4525
C_m/C_{m0}	1	1.0281	1.3003	1.4746	1.6706	2.1505	2.8050
α_w/α_{w0}	1	1.0054	1.0050	1.0047	1.0049	1.0046	1.0045
\dot{m}_d/\dot{m}_{d0}	1	1.0509	1.3234	1.4979	1.6948	2.1767	2.8343
δ^*/δ^*_0	1	0.9989	1.0024	1.0197	1.0474	1.1362	1.2807

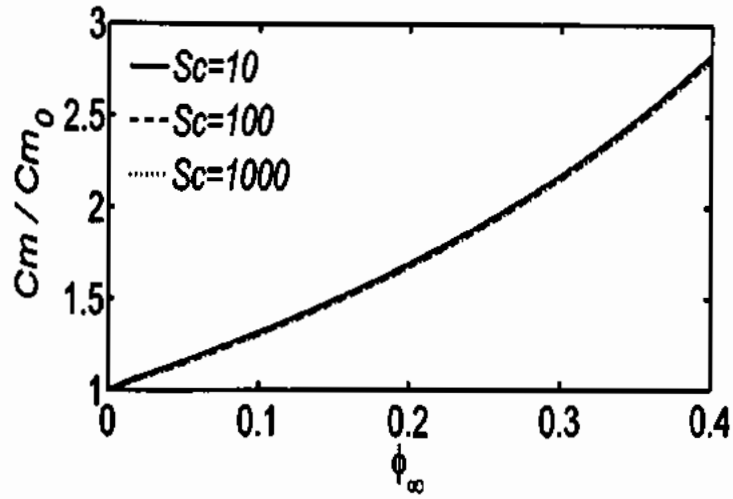


Fig. 2.8: Relative moment coefficient plotted against ϕ_∞ .

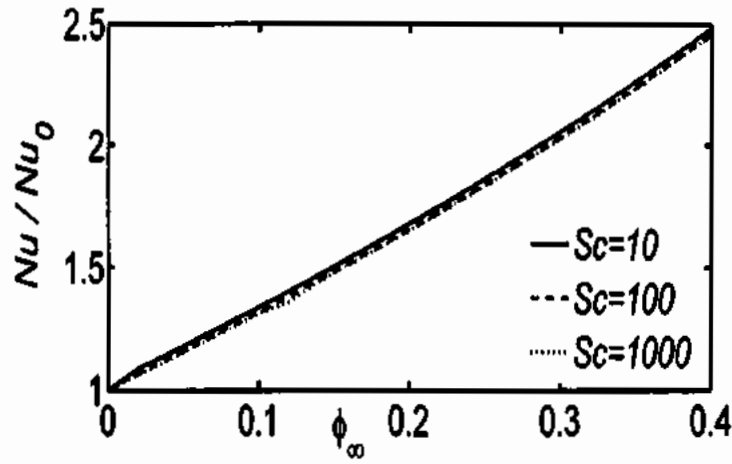


Fig. 2.9: Relative Nusselt number as a function of nanoparticle concentration.

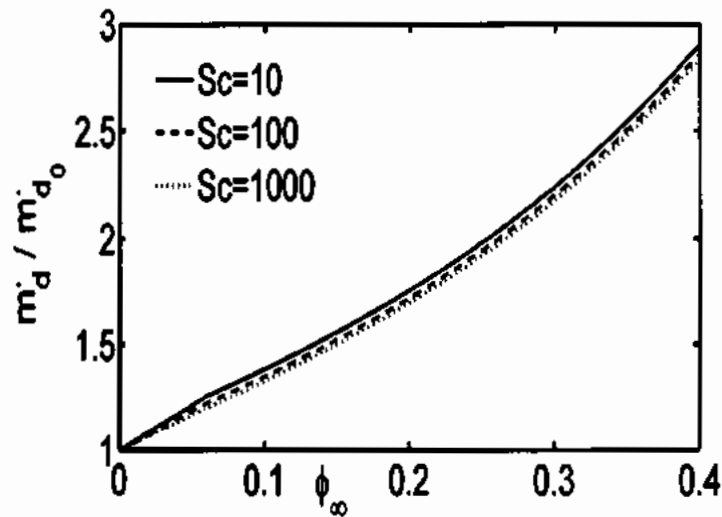


Fig. 2.10: Relative mass flow rate as a function of nanoparticle concentration.

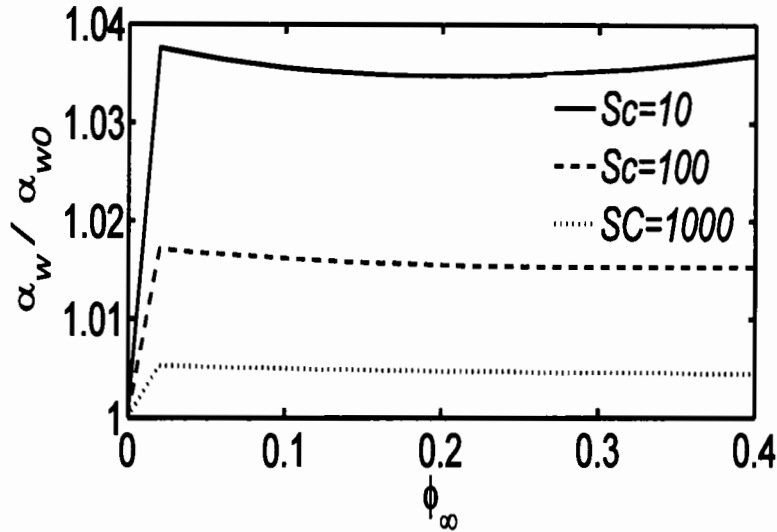


Fig. 2.11: Relative tangent of the swirl angle plotted against ϕ_∞ .

The reliance of physical quantities, namely, the moment coefficient, the mass flow rate, the tangent of angle of swirl, the displacement thickness, and the Nusselt number on the pure fluid is a significant feature of present work. The current findings help one to identify a specific pure fluid which should be employed to attain optimal results in practical applications. This information can be found from Tables 2.3 and 2.4 where the results are listed for several Prandtl numbers. Table 2.3 contains percent increase in the heat transfer rate for different types of pure fluids. It is obvious that higher heat transfer rate occurs for pure fluids having larger Prandtl number. For a fixed $Sc = 10$ and $\phi_\infty = 0.01$, an enhancement of almost 129% in heat transfer is achieved when the Prandtl number is varied 130 times (i.e. from 0.1 to 13). But for the nanofluid with 20% nanoparticles the enhancement is not that significant, which is almost 3.18%. Almost the same situation persists with some depreciation for $Sc = 100$. On the other hand 68% augmentation in heat transfer rate is observed for water containing 20% nanoparticles. Table 2.3 concludes that the heat transfer rate is increased for the base fluid having larger Prandtl numbers, but the major enhancement in heat transfer rate exists at higher nanoparticle concentration. The relative values of aforementioned parameters are demonstrated in Table 2.4 for various Prandtl numbers. From this Table it is revealed that all the parameters are not a strong function of Prandtl number. This means that the substantial augmentation in heat transfer rate (as observed in Table 2.3) is just because of the insertion of nanoparticles and the nature of clear fluid does not matter by a lot. However, the fluids of larger Prandtl number serve as a good coolant at

very low concentration levels of nanoparticles. In a similar manner the impact of the diffusion parameter (D) has been explored in Table 2.5. The values of the moment coefficient, the mass flow rate, displacement thickness, tangent of the flow swirl angle, and the Nusselt number are enhanced up to 5%, 7%, 8%, 14%, and 8%, respectively, when the values of D were enlarged by 20 times. This reveals a considerable impact of the diffusion parameter towards flow and heat transfer augmentation. The discussion of Tables 2.3-2.5 concludes that maximum gain in the heat transfer rate is attained by increasing the concentration level of nanoparticle and further augmentation is acquired by incorporating the effect of diffusion parameter and the nature of the pure fluid. Table 2.6 exhibits very vital findings about the current non-homogeneous model of the nanofluid. A comparison has been made in Table 2.6 between the non-homogeneous (in the current work) and homogeneous (Tiwari and Das [42]) models towards the augmentation of heat transfer rate. The comparison shows that the non-homogeneous model predicts higher heat transfer rate at all nanoparticle concentration levels and for all Prandtl numbers. It is also noted that the difference gets wider when the nanoparticle concentration is 10% or higher. Particularly, almost 30% more gain in the rate of heat transfer is observed for water having 20% nanoparticles for non-homogeneous model in comparison to the homogeneous model. From here one can realize the importance of non-uniform distribution of nanoparticles within the boundary-layer which is completely ignored in the Tiwari and Das [42] model (i.e. homogeneous model).

Table 2.3: Percent increase in the values of Nusselt number relative to the pure fluid calculated at different Pr when $D = 0.05$, $\frac{\rho_p}{\rho_f} = 3.98195$.

Pr	$Sc = 10$			$Sc = 100$		
	$\phi_\infty = 0.01$	$\phi_\infty = 0.1$	$\phi_\infty = 0.2$	$\phi_\infty = 0.01$	$\phi_\infty = 0.1$	$\phi_\infty = 0.2$
0.1	2.8463%	30.2198%	66.5684%	2.8069%	30.1748%	66.5140%
1.0	3.7659%	31.5972%	66.3448%	3.0856%	30.8465%	65.5093%
6.0	5.5816%	33.6799%	67.8088%	3.6071%	31.5329%	65.4810%
10.0	6.1954%	34.3412%	68.3926%	3.8613%	31.8120%	65.6580%
13.0	6.5041%	34.6684%	68.6865%	4.0140%	31.9754%	65.7776%

Table 2.4: Relative values of important physical parameters for different values of Pr when $D = 0.05$, $\frac{\rho_p}{\rho_f} = 3.98195$, $\phi_\infty = 0.1$.

Pr		0.1	1	6	10	13
$Sc = 10$	Nu/Nu_0	1.3022	1.3160	1.3368	1.3434	1.3467
	C_m/C_{m0}	1.3028	1.3122	1.3166	1.3162	1.3157
	α_w/α_{w0}	0.9922	1.0065	1.0237	1.0281	1.0030
	\dot{m}_d/\dot{m}_{d0}	1.3108	1.3439	1.3813	1.3919	1.3974
	δ^*/δ^*_0	1.0038	1.0122	1.0202	1.0219	1.0225

$Sc = 80$	Nu/Nu_0	1.3018	1.3088	1.3165	1.3197	1.3215
	C_m/C_{m0}	1.3004	1.3026	1.3042	1.3044	1.3044
	α_w/α_{w0}	0.9902	0.9969	1.0061	1.0090	1.0105
	\dot{m}_d/\dot{m}_{d0}	1.3066	1.3246	1.3497	1.3593	1.3640
	δ^*/δ^*_0	1.0022	1.0054	1.0097	1.0108	1.0113

Table 2.5: Effects of D for $Pr = 6$, $\frac{\rho_p}{\rho_f} = 3.98195$, $\phi_\infty = 0.1$.

D		0.01	0.05	0.1	0.15	0.2
$Sc = 10$	Nu/Nu_0	1.3145	1.3368	1.3640	1.3905	1.4163
	C_m/C_{m0}	1.3032	1.3166	1.3328	1.3483	1.3632
	α_w/α_{w0}	0.9955	1.0237	1.0598	1.0967	1.1347
	\dot{m}_d/\dot{m}_{d0}	1.3169	1.3809	1.4589	1.5348	1.6097
	δ^*/δ^*_0	1.0056	1.0202	1.0398	1.0592	1.0791
$Sc = 80$	Nu/Nu_0	1.3104	1.3165	1.3239	1.3310	1.3378
	C_m/C_{m0}	1.3007	1.3042	1.3086	1.3128	1.3168
	α_w/α_{w0}	0.9921	1.0061	1.0239	1.0418	1.0599
	\dot{m}_d/\dot{m}_{d0}	1.3110	1.3494	1.3960	1.4420	1.4871
	δ^*/δ^*_0	1.0031	1.0097	1.0180	1.0263	1.0348

Table 2.6: Percent increase in heat transfer rate computed for homogeneous and non-homogeneous models.

Pr	Homogeneous			Non-homogeneous ($Sc = 10$)		
	$\phi_\infty = 0.01$	$\phi_\infty = 0.1$	$\phi_\infty = 0.2$	$\phi_\infty = 0.01$	$\phi_\infty = 0.1$	$\phi_\infty = 0.2$
0.1	0.00%	0.94%	4.93%	2.85%	30.22%	66.57%
1.0	1.13 %	10.91%	22.03%	3.77%	31.60%	66.34%
6.0	1.60 %	15.85 %	31.83 %	5.58%	33.68%	67.81%
10.0	1.66%	16.53%	33.20%	6.19%	34.34%	68.39%
13.0	1.68%	16.80%	33.77%	6.50%	34.67%	68.69%

CHAPTER 3

Heat Transfer Enhancement via Non-Isothermal Rotating Disk

The consideration of variable disk temperature is another strategy towards the enhanced heat transfer phenomena. Usually, according to literature, certain convenient forms of variable wall temperature are considered which consequently give rise to a self-similar heat transfer problem. However, in this chapter a new class of variable surface temperatures of rotating disk has been considered for which the heat transfer phenomenon turns to non-similar nature within the rotating boundary-layer. Within the volume of available literature only those variable disk temperatures have been considered for which the self-similarity of the associated convective heat transport phenomenon does not break down; such a variable disk temperature, in general, belongs to the power-law family. In this chapter, consideration has been given to those variable forms which do not belong to this family. Specifically, the sinusoidal; the exponential (increasing/decreasing), and the non-linearly varying (increasing/decreasing) surface temperature distribution of the rotating disk have been considered for which the self-similar solution is impossible; and have never been studied so-far, to the best of our knowledge. The motivation behind this study is twofold: first, to extend the heat transfer phenomenon in the rotating disk flow from self-similar to non-similar case; second, to find out the best possible situations which result in the enhanced heat transfer process with the consideration of above mentioned interesting forms. Our analysis reveals a significant heat transfer enhancement for the case of exponential and non-linearly increasing distribution of the disk temperature. For example, exponentially increasing disk temperature of a freely rotating disk in the quiescent air yields 27% augmentation in heat transfer rate in comparison to the isothermal case. Similarly, an enhancement of 15% in the heat transfer rate is obtained for the case of increasing non-linear disk temperature when again compared with the isothermal case. Whereby the other forms of the variable disk temperature show a reverse trend with some interesting findings highlighting the insulating role of rotating disk under certain conditions. In addition to these conclusions the considered cases have been investigated in detail and the results

have been reported in several Tables which would serve as a reference for the future experimental and theoretical studies.

3.1 Problem statement

It is an established and well known fact that the problem of rotating free disk does admit an exact similarity solution for both, the boundary-layer equations and the full Navier-Stokes equations with the consideration of no boundary-layer assumption at all. However, it is also generally agreed upon that the rotating free disk flow does exhibit the boundary-layer character. Being convinced by this fact, we do prefer to utilize the boundary-layer equations in this study. The axially-symmetric nature of this flow makes the velocity, pressure, and the temperature function independent of the polar coordinate. The absence of any potential flow makes the pressure constant within the boundary-layer. Consequently, the pressure gradient terms, appearing in the Navier-Stokes equations, get vanished. In view of the above facts the boundary-layer equations for the steady, incompressible three-dimensional, axi-symmetric flow due to a rotating free disk are given in Eqs. (1.7)-(1.10). The associated boundary data is

$$\left. \begin{aligned} v_r = v_z = v_\phi - \omega r = 0, \quad T_w - T_\infty = S_w(r), \quad \text{at } z = 0 \\ v_r = v_z = 0, \quad T = T_\infty \quad \text{at } z \rightarrow \infty \end{aligned} \right\} \quad (3.1)$$

where $S_w(r)$ is an arbitrary temperature distribution. The similarity variables are defined as

$$r^* = \frac{r}{b}, \quad \eta = \sqrt{\frac{\omega}{\nu}} z. \quad (3.2)$$

The non-dimensional functions are defined by

$$\psi(r, z) = \sqrt{\nu \omega} r^2 f(r^*, \eta), \quad g(r^*, \eta) = \frac{v_\phi}{\omega r}, \quad \Theta(\varepsilon, \eta) = \frac{T - T_\infty}{T_w - T_\infty}, \quad (3.3)$$

$$\text{where } v_r = \frac{\partial \psi}{\partial z}, \quad v_z = -\frac{\partial \psi}{\partial r}.$$

In view of above relation the equation of continuity is satisfied identically and the utilization of these relations along with Eq. (3.3) transforms the Eqs. (1.8) & (1.9) to the self-similar form and the Eq. (1.10) to non-similar form given, respectively, by

$$f_{\eta\eta\eta} - f_\eta^2 + g_\eta^2 + 2f f_{\eta\eta} = 0, \quad (3.4)$$

$$g_{\eta\eta\eta} - 2f_\eta g_\eta + 2f g_{\eta\eta} = 0, \quad (3.5)$$

$$\frac{\Theta_{\eta\eta}}{Pr} + 2f\Theta_\eta - P(r^*)f_\eta\Theta = r^*f_\eta\Theta_{r^*}, \quad (3.6)$$

$$\text{where } P(r^*) = r^* \frac{d \ln S_w(r^*)}{dr^*}. \quad (3.7)$$

The corresponding boundary data, defined in Eq. (3.1), do also transform as

$$\left. \begin{aligned} f = g = f_\eta = g_\eta - 1 = \Theta - 1 = 0 & \quad \text{at } \eta = 0 \\ f_\eta = 0, g_\eta = 0, \Theta = 0 & \quad \text{at } \eta = \infty \end{aligned} \right\} \quad (3.8)$$

In view of Eq. (3.3) the definition of the Nusselt number furnishes the following formula:

$$Nu = -\Theta_\eta(r^*, 0). \quad (3.9)$$

3.2 Heat transfer analysis

Three different forms of the disk temperature functions have been considered in this study, as mentioned in the introduction part, namely, the sinusoidal form, the exponential form, and the polynomial form. Both, the quantitative and qualitative descriptions of the results have been made in this section for a wide range of Prandtl number values (i.e. from 0.1 to 100). An implicit finite difference scheme (Keller-box) has been utilized for the solution of Eqs. (3.4) – (3.6) & (3.8).

3.2.1 Sinusoidal disk temperature variations

The surface temperature of the disk in this case is taken of sinusoidal form $T_w - T_\infty = A \sin r^*$ which transforms the Eq. (3.7) into the form

$$P(r^*) = r^* \cot r^*; P(0) = 1. \quad (3.10)$$

The values of heat transfer coefficient are quantified in Table 3.1 (also see Fig. 3.1) with the help of numerical computations. From Table 3.1 it is clear that the values of the Nusselt number decrease as one marches in the increasing radial direction. This depreciation in the heat transfer phenomena is found to depend on the nature of the fluid by noticing an overall (i.e. from $r^* = 0.0$ to 1.0) decrease in the heat transfer rate (when one moves from $r^* = 0.0$ to 1.0) is 9%, 5.8%, 5.4%, 4.3% and 4.4% for $Pr = 0.1, 0.71, 1.0, 10$ & 100, respectively, (refer to Table 3.1) in comparison to the isothermal case.

Table 3.1: Local Nusselt number at various stations for sinusoidal disk temperature.

r^*/Pr	0.1	0.71	1	10	100
0	0.1104	0.4319	0.5180	1.4094	3.3035
0.05	0.1104	0.4319	0.5179	1.4085	3.2839
0.10	0.1104	0.4317	0.5177	1.4081	3.2831
0.20	0.1101	0.4310	0.5170	1.4064	3.2795
0.50	0.1081	0.4260	0.5114	1.3945	3.2539
0.75	0.1050	0.4183	0.5028	1.3761	3.2143
0.90	0.1024	0.4120	0.4956	1.3608	3.1815
1.00	0.1004	0.4068	0.4899	1.3487	3.1554

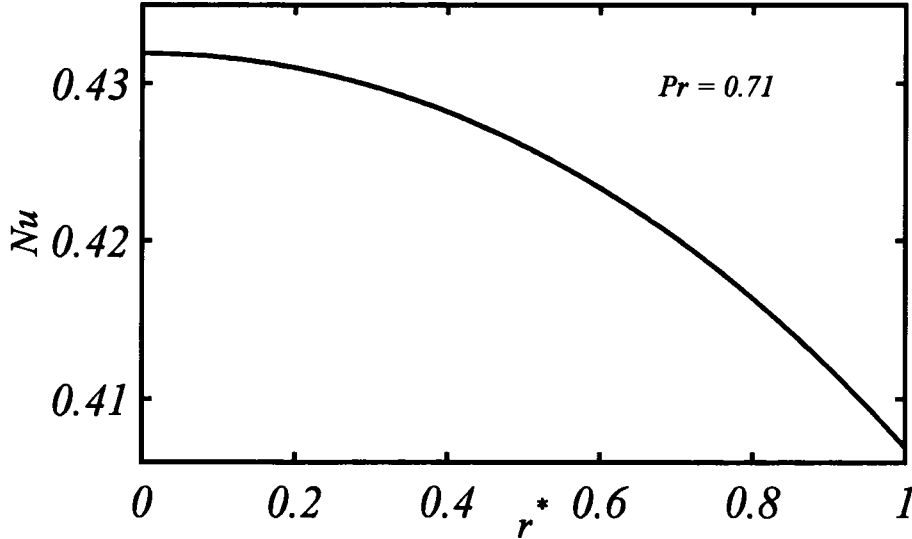


Fig. 3.1: Variation in Nusselt number for sinusoidal disk temperature.

3.2.2 Exponential disk temperature distribution

In this case the variation of the disk temperature is taken of the form $T_w - T_\infty = Ae^{mr^*}$ which modifies the Eq. (3.7) as

$$P(r^*) = mr^*; \quad P(0) = 0. \quad (3.11)$$

Interestingly, for $r^* = 0 = m$ the disk temperature reduces to the isothermal case for which the thermal transport is self-similar. In view of solution procedure, the self-similar solution (at $r^* = 0$) has been utilized as an initial solution for the non-similar case. Figure 3.2 depicts the heat transfer rate obtained for $m = \pm 1, \pm 2$ and ± 3 at $Pr = 0.71$ against r^* showing increasing behavior for $m > 0$ and decreasing behavior for $m < 0$ as one marches outwards radially. Obviously the positive values of m correspond to radially increasing surface temperature, whereas the negative values of m correspond to radially decreasing distribution of temperature. Consequently, the rate of heat exchange is an increasing function of r^* for $m = 1, 2,$ and 3 and a decreasing function for $m = -1, -2,$ and -3 . However, the radial dependence of the heat transfer rate is linear for all $m = \pm 1, \pm 2,$ and ± 3 which is an interesting observation, indeed. More detailed analysis of this case has also been made reflecting the dependence of heat transfer rate on the exponent m which is summarized in Tables 3.2 – 3.4. It is observed that the values $m > 0$ lead to heat transfer enhancement (see Table 3.2 and Fig. 3.2) whereas $m < 0$ cause to decrease the Nusselt number (see Table 3.3 and Fig. 3.2). Table 3.4 contains the information about the particular values of r^* (for $m = -3$ and $m = -4$) beyond which the heat transfer phenomena ceases to exist.

The r^* –stations corresponding to (almost) zero heat transfer rate were found to depend on the exponent m as well as the Prandtl number Pr . For example, such local stations are $r^* = 0.545, 0.68, 0.705, 0.84$ & 0.89 corresponding to $Pr = 0.1, 0.71, 1, 10$ & 100 , respectively, for $m = -4$. Clearly, higher values of Pr cause to shift these local r^* –stations towards the disk rim ($r^* = 1$). For $m = -3$ there are no such local r^* –stations for $Pr = 10$ & 100 having negligible heat transfer rate. This means that the heat transfer phenomenon survives for $m = -3$ (for $Pr = 10$ & 100) but couldn't sustain at the further reduced disk temperatures (i.e. the case $m = -4$).

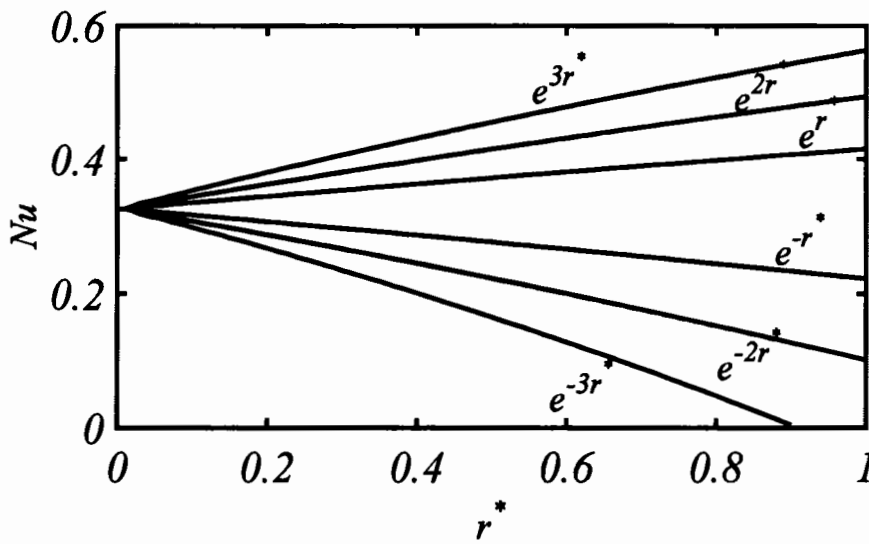


Fig. 3.2: Local Nusselt number corresponding to exponentially varying disk temperature.

Table 3.2: Local Nusselt number at various stations for exponentially increasing disk temperature.

r^*/Pr	$m = 1$					$m = 2$				
	0.1	0.71	1	10	100	0.1	0.71	1	10	100
0	0.0766	0.3259	0.3962	1.1341	2.6871	0.0766	0.3259	0.3962	1.1341	2.6871
0.05	0.0782	0.3304	0.4014	1.1457	2.7120	0.0797	0.3349	0.4066	1.1571	2.7366
0.10	0.0798	0.3352	0.4069	1.1578	2.7383	0.0830	0.3444	0.4174	1.1810	2.7885
0.20	0.0830	0.3447	0.4176	1.1816	2.7897	0.0893	0.3629	0.4384	1.2274	2.8889
0.50	0.0926	0.3722	0.4489	1.2506	2.9391	0.1080	0.4153	0.4980	1.3581	3.1719
0.75	0.1004	0.3942	0.4740	1.3056	3.0583	0.1230	0.4560	0.5440	1.4585	3.3888
0.90	0.1050	0.4071	0.4886	1.3377	3.1276	0.1318	0.4791	0.5702	1.5154	3.5116
1.00	0.1081	0.4155	0.4982	1.3587	3.1730	0.1376	0.4941	0.5871	1.5521	3.5907

Table 3.3: Local Nusselt number at various stations for exponentially decreasing disk temperature.

r^*/Pr	$m = -2$					$m = -1$				
	0.1	0.71	1	10	100	0.1	0.71	1	10	100
0	0.0766	0.3259	0.3962	1.1341	2.6871	0.0766	0.3259	0.3962	1.1341	2.6871
0.05	0.0736	0.3167	0.3858	1.1111	2.6369	0.0751	0.3213	0.3910	1.1227	2.6621
0.10	0.0702	0.3068	0.3745	1.0860	2.5825	0.0735	0.3164	0.3855	1.1103	2.6353
0.20	0.0636	0.2867	0.3515	1.0349	2.4716	0.0702	0.3066	0.3742	1.0854	2.5812
0.50	0.0431	0.2226	0.2780	0.8703	2.1139	0.0602	0.2762	0.3395	1.0080	2.4132
0.75	0.0254	0.1644	0.2110	0.7186	1.7838	0.0517	0.2498	0.3092	0.9403	2.2662
0.90	0.0145	0.1271	0.1679	0.6204	1.5696	0.0465	0.2335	0.2905	0.8983	2.1748
1.00	0.0070	0.1012	0.1379	0.5516	1.4195	0.0431	0.2224	0.2777	0.8696	2.1124

Table 3.4: Local Nusselt number at various stations for exponentially decreasing disk temperature.

r^*/Pr	$m = -4$					r^*/Pr	$m = -3$				
	0.1	0.71	1	10	100		0.1	0.71	1	10	100
0.000	0.0766	0.3259	0.3962	1.1341	2.6871	0	0.0766	0.3259	0.3962	1.1341	2.6871
0.050	0.0705	0.3075	0.3752	1.0875	2.5858	0.05	0.0720	0.3121	0.3805	1.0993	2.6115
0.100	0.0638	0.2872	0.3521	1.0360	2.4743	0.10	0.0670	0.2971	0.3634	1.0612	2.5289
0.200	0.0502	0.2452	0.3039	0.9284	2.2405	0.20	0.0570	0.2663	0.3281	0.9825	2.3581
0.500	0.0072	0.1018	0.1386	0.5534	1.4233	0.50	0.0255	0.1647	0.2113	0.7194	1.7855
0.545	0.0004	0.0777	0.1107	0.4892	1.2829	0.725	0.0005	0.0781	0.1111	0.4901	1.2849
0.680		0.0007	0.0210	0.2813	0.8280	0.75		0.0678	0.0992	0.4626	1.2249
0.705			0.0034	0.2401	0.7377	0.90		0.0033	0.0241	0.2884	0.8336
0.840				0.0011	0.2132	0.905		0.0011	0.0215	0.2823	0.8302
0.890					0.0016	0.945			0.0003	0.2327	0.7217
						1.000				0.1625	0.5676

3.2.3 Polynomial (increasing or decreasing) form of disk temperature

A polynomial (increasing/decreasing) form of disk temperature i.e., $T_w - T_\infty = (1 \pm r^{*n})$ is considered in this case due to which Eq. (3.7) modifies as

$$P(r^*) = \pm \frac{nr^{*n}}{(1 \pm r^{*n})}; \quad P(0) = 0. \quad (3.12)$$

The selection of '+' and '-' signs in the above expression, respectively, correspond to the increasing and decreasing disk temperatures. Figure 3.3 shows the variation of heat transfer rate against the radial coordinate (r^*) in the case of increasing and decreasing polynomial temperature distributions. Heat transfer augmentation can be noticed in the increasing case, whereas the reverse is observed in the case of decreasing distribution of the disk temperature. However, the rate of increase/decrease of the Nusselt number, in this case is lesser than the exponential case. Furthermore, the variation in Nusselt number does not follow the linear relationship with r^* as it was observed in the exponential case. Table 3.5 reflects that a total increase of 21.7%, 15.4%, 14.5%, 11.2%, 10.3% (for $n = 1$) and 40.9%, 26.8%, 25%, 19%, 17.4% (for $n = 2$) in heat transfer rate (for the case of $(1 + r^{*n})$) is observed when one moves from $r^* = 0.0$ to $r^* = 1.0$ corresponding to $Pr = 0.1, 0.71, 1, 10$ & 100 , respectively. Again, higher

values of the Prandtl number lead to the increased value of the heat transfer rate, while on the other hand a decreasing trend is noted for the decreasing disk temperature ($1 - r^{*n}$). Table 3.6 signifies that a decrease of 22.3%, 16.8%, 15.8%, 12.5%, 11.4% (for $n = 1$) and 43.5%, 30.4%, 28.5%, 22%, 20% (for $n = 2$) in the heat transfer rate are observed, for the same variation of Pr , as one moves from $r^* = 0.0$ to $r^* = 1.0$. In comparison to the exponential case a general observation is possible to draw that the thermal transport is, in total, depreciated in the polynomial distribution case. However, an interesting advantage of the polynomial distribution in the case of the decreasing disk temperature is that the heat transfer process starts to seize for the higher values of the power index n . For instance, heat transfer rates are diminished at $r^* = 1.0$ for $n = 5.1$ ($Pr = 0.1$), $n = 12.8$ ($Pr = 0.71$), $n = 15.2$ ($Pr = 1$), $n = 32.2$ ($Pr = 10$), and $n = 46$ ($Pr = 100$).

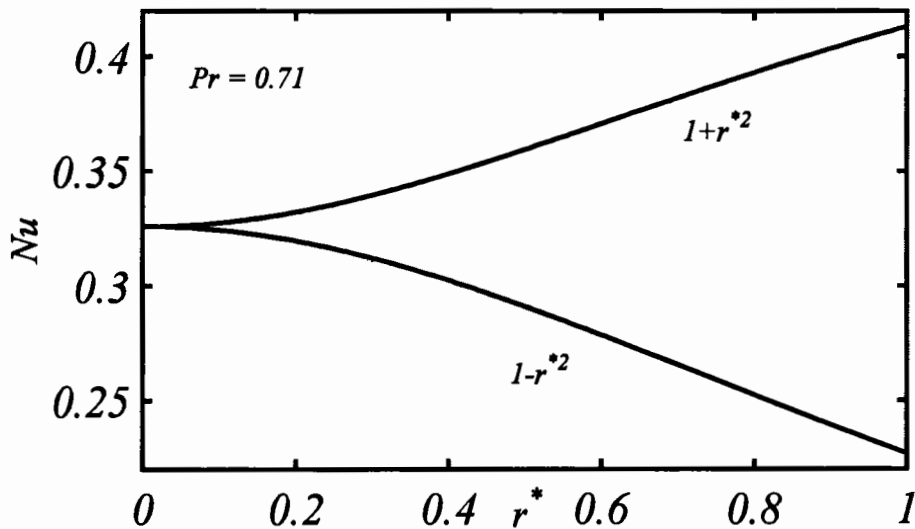


Fig. 3.3: Local Nusselt number for polynomial distribution of disk temperature.

Table 3.5: Local Nusselt number at various stations for non-linearly increasing disk temperature.

r^*/Pr	$n = 1$					$n = 2$				
	0.1	0.71	1	10	100	0.1	0.71	1	10	100
0.00	0.0766	0.3259	0.3962	1.1341	2.6871	0.0766	0.3259	0.3962	1.1341	2.6871
0.05	0.0781	0.3303	0.4012	1.1452	2.7110	0.0768	0.3263	0.3967	1.1351	2.6891
0.10	0.0796	0.3345	0.4061	1.1559	2.7344	0.0772	0.3275	0.3980	1.1380	2.6954
0.20	0.0821	0.3420	0.4146	1.1748	2.7755	0.0789	0.3321	0.4033	1.1494	2.7202
0.50	0.0876	0.3587	0.4337	1.2174	2.8678	0.0888	0.3593	0.4341	1.2165	2.8653
0.75	0.0908	0.3685	0.4449	1.2424	2.9221	0.0989	0.3874	0.4659	1.2861	3.0158
0.90	0.0923	0.3732	0.4503	1.2544	2.9482	0.1045	0.4033	0.4840	1.3257	3.1013
1.00	0.0932	0.3760	0.4535	1.2615	2.9636	0.1079	0.4131	0.4951	1.3500	3.1539

Table 3.6: Local Nusselt number at various stations for non-linearly decreasing disk temperature.

r^*/Pr	$n = 1$					$n = 2$				
	0.1	0.71	1	10	100	0.1	0.71	1	10	100
0.00	0.0766	0.3259	0.3962	1.1341	2.6871	0.0766	0.3259	0.3962	1.1341	2.6871
0.05	0.0752	0.3215	0.3912	1.1231	2.6631	0.0765	0.3255	0.3958	1.1333	2.6852
0.10	0.0737	0.3172	0.3863	1.1120	2.6392	0.0761	0.3244	0.3945	1.1303	2.6789
0.20	0.0712	0.3094	0.3774	1.0922	2.5962	0.0744	0.3196	0.3892	1.1187	2.6538
0.50	0.0654	0.2913	0.3566	1.0454	2.4944	0.0642	0.2910	0.3567	1.0478	2.5003
0.75	0.0621	0.2801	0.3437	1.0162	2.4307	0.0534	0.2589	0.3201	0.9673	2.3260
0.90	0.0605	0.2746	0.3373	1.0016	2.3796	0.0471	0.2393	0.2977	0.9175	2.2181
1.00	0.0595	0.2713	0.3335	0.9928	2.3796	0.0433	0.2267	0.2832	0.8852	2.1479

CHAPTER 4

Heat Transfer Augmentation in Rotating Flow between a Cone and Disk with Suction/Injection

The impact of mass removal or addition on the flow and heat transfer phenomena inside a gap between a cone and a porous disk has been examined in this chapter. The convective transport phenomena are examined under various conditions including stationary disk with rotating cone and vice versa, co- and counter-rotation of cone and disk with prescribed values of mass transfer parameter. It is revealed that mass removal or addition plays an important role in altering the nature of flow inside the gap in all the considered cases. The heat transfer phenomenon is also strongly influenced by the mass removal or fluid injection. Specifically, an interesting relation between the exponent of the radial distribution of disk temperature and the mass transfer parameter is realized in the current study. For the radially increasing temperature of the disk surface the fluid injection optimizes the heat transfer phenomenon whereas for the isothermal and radially decreasing temperature situations the wall suction is required for the augmentation of heat transfer process. In this regard, some threshold values of the mass transfer parameter are determined which correspond to the diminishing of the heat transfer process.

4.1 Problem formulation

An incompressible viscous fluid having constant properties is assumed to be filling the gap between a flat porous disk of sufficiently large radius and a vertical circular cone joining the disk at its center. In general, the disk and the cone are assumed to rotate with different rotation rates. This gives rise to a main rotating flow and a secondary radial flow within the conical gap. The disk surface is assumed to be heated variably; following the power-law distribution in r . The advantage of such a power-law temperature distribution of the disk surface is twofold: (i) such a power-law form in r does not alter the self-similarity of the thermal transport because of the admissibility of the scaling symmetry by it; just for mentioning, the rotating velocities of the disk and the cone does also follow a power-law form in r (with the selection of power-law

exponent equal to unity) which are in fact responsible for its self-similar nature, (ii) in many practical applications the variable disk temperature usually follows the power-law form such as in the heated cavities of the gas turbine. A stationary frame of reference with respect to the rotating disk or cone has been considered (as shown in Fig. 4.1). The body forces are assumed to be absent and the energy losses due to viscous dissipation have been neglected. Moreover the internal heat generation/absorption is also assumed to be absent in the considered flow. With the consideration of these assumptions the laws of conservation of mass, momentum and energy are given in system (1.1) – (1.5) subject to the boundary conditions

$$\left. \begin{aligned} z = 0: & \quad v_r = 0, \quad v_z = v_{wd}, \quad v_\varphi = \Omega r, \quad T_w - T_\infty = c_0 r^{n_*} \\ z = h(r): & \quad v_r = 0, \quad v_z = 0, \quad v_\varphi = \omega r, \quad T = T_\infty \end{aligned} \right\}. \quad (4.1)$$

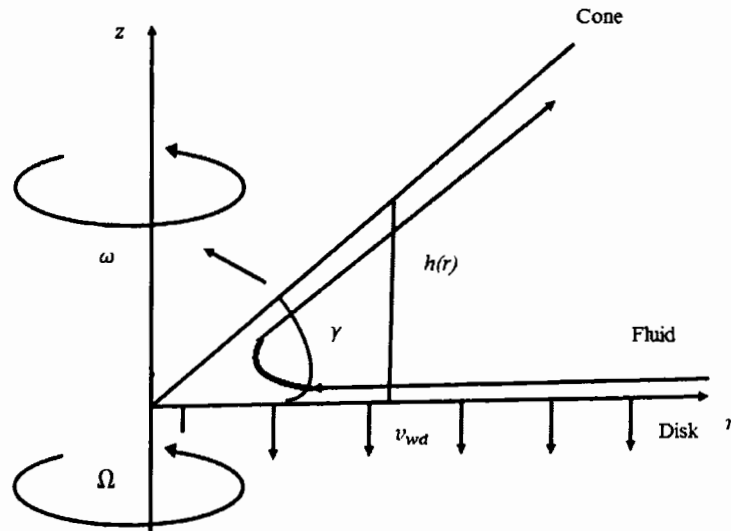


Fig. 4.1: Schematic of the flow.

The quantity v_{wd} denotes the suction/injection velocity at the disk boundary (wall). The constant n_* permits to model the temperature of the disk as radially decreasing ($n_* < 0$), constant ($n_* = 0$), and radially increasing ($n_* > 0$) which is of significant importance from the engineering perspective. The conical gap height is denoted and defined by

$$h(r) = r \tan \gamma. \quad (4.2)$$

Since the heat transfer phenomenon within the gap, due to the radial distribution of disk temperature, is the focus of this study. In this regard, the cone temperature is assumed to be the reference ambient temperature (T_∞).

4.2 Similarity solution

In the absence of any cone the gap widens to an open semi-infinite space above the rotating disk, and the considered problem turns to the classical von-Kármán problem for which the three-dimensional Navier-Stokes equations admit an exact solution. Therefore, the current problem is better to be considered as an extension of the classical von-Kármán swirling flow. In this perspective, the considered problem may or may not allow for an exact self-similar solution, in general. In view of a similarity criteria of the classical von-Kármán problem, a similarity solution is likely to exist for a gap geometry if the gap height remains constant at all local radial locations. In this way the current problem seems quite unlikely to admit an exact self-similar solution therefore a corresponding non-similar formulation would be the better ultimate strategy. However, in view of the existing researches on this flow, a self-similar formulation has been reported to work quite good in order to achieve an excellent agreement of the theoretical results with the available experimental data (see for instance [68]). An acceptable mathematical justification to this fact could be that, as the flow is self-similar for a rotating free disk as well as for the gap of constant height, where the variable height of the gap is not a big departure from the self-similarity situation which also does not destroy the self-similarity by a lot and allows to obtain a quite exact solution (due to the self-similar formulation) at the local r -locations which could be designated as locally self-similar in nature. Based upon these facts the considered problem does also allow for a locally self-similar solution in an analogous manner. Therefore, the self-similar form of the governing transport equations are obtained as

$$H' - \eta F' = 0, \quad (4.3)$$

$$MF'' + \eta P' + LF' + 2P + F^2 + G^2 = 0, \quad (4.4)$$

$$MG'' + LG' = 0, \quad (4.5)$$

$$MH'' + LH' + H(1 + F) - P' = 0, \quad (4.6)$$

$$\Theta'' - Pr(\nu_* F \Theta + \Theta'(H - \eta F)) = 0, \quad (4.7)$$

by the utilization of the similarity variables defined by (see [68])

$$\eta = \frac{z}{r}, \quad F = \frac{rv_r}{\nu}, \quad G = \frac{rv_\theta}{\nu}, \quad H = \frac{rv_z}{\nu}, \quad P = \frac{pr^2}{\rho\nu^2}, \quad \Theta = \frac{T - T_\infty}{T_w - T_\infty}, \quad (4.8)$$

due to which the related boundary conditions do also transform as

$$\left. \begin{aligned} \eta = 0: & \quad F = 0, \quad G = G_0, \quad H = H_w, \quad \Theta = 1 \\ \eta = \eta_1: & \quad F = 0, \quad G = G_1, \quad H = 0, \quad \Theta = 0 \end{aligned} \right\} \quad (4.9)$$

where $M = \eta^2 + 1$, $L = 3\eta + \eta F - H$, $\eta_1 = \frac{h}{r}$, $G_0 = Re_\Omega$, $G_1 = Re_\omega$, $Re_\Omega = \frac{\Omega r^2}{\nu}$, $Re_\omega = \frac{\omega r^2}{\nu}$. In Eq. (4.9) $H_w (= v_{wd} r/\nu)$ denotes the non-dimensional wall velocity normal to the disk surface. Negative values of H_w correspond to suction (i.e. mass withdrawal) whereas the positive values correspond to the uniform wall injection. The primes in Eqs. (4.3) – (4.7) denote the differentiation w.r.t. η . The transformed system of equations, namely, Eqs. (4.3) – (4.7) and Eq. (4.9) allow to make an important note here. The transformed transport equations (4.3) – (4.7) are in self-similar form with the complete elimination of the previous variables, but, the boundary conditions (4.9) do not appear in self-similar form because of the appearance of the original (previous) variable r in Eq. (4.9). However, an exact self-similarity solution is still possible and limited to the cases: fixed disk with G_1 being constant or for stationary cone with G_0 being constant. In general, such type of boundary conditions (in full) are designated as locally self-similar where both the parameters (G_0 & G_1) are considered at each concrete location r [69]. Interestingly, such consideration produces quite accurate results which are in very good accordance with the experimental and predicted data as reported by Shevchuk [68].

Built-in solver of the Mathcad software is used for the solution of Eqs. (4.3) – (4.7) and (4.9) with the help of shooting method for various arbitrarily chosen values of H_w . The influence of mass transfer parameter H_w on the velocity and temperature profiles, for all possible considered situations, is depicted through several plots where the quantified data have been reported in the form of numerous Tables. Following Shevchuk [68], only two values of the gap angle ($\gamma = \frac{\pi}{45}$ ($\eta_1 = 0.0698$) and $\frac{\pi}{4}$ ($\eta_1 = 1$)) have been taken into account just to make the present outcomes in accordance with the already existing results. The calculations are performed for only a single value of Prandtl number i.e. 0.71 (air). By doing so the attention has been focused upon the realization of an interesting relationship (inter-dependence) between the mass transfer parameter (H_w) and the temperature power-law index (n_*) which enables one to understand its important role towards the heat transfer enhancement. For this purpose, different values of n_* , for example $n_* = -1$ (decreasing), $n_* = 0$ (constant), $n_* = 1$ (linearly increasing) and $n_* = 2$ (quadratically increasing) have been taken into account which characterize the heat transfer from the disk, as observed in the related engineering applications. The value of $Re = Re_\Omega \eta_1^2/12$ or $Re = Re_\omega \eta_1^2/12$ is taken equal to unity.

Consequently, $Re_{\Omega} = Re_{\omega} = 12$ at $\eta_1 = 1$ and $Re_{\Omega} = Re_{\omega} = 2463$ at $\eta_1 = 0.0698$. A detailed analysis has been made in four different cases which are discussed one-by-one in the following:

Case I: Rotating cone with stationary permeable disk

The velocity components in a large conical gap ($\eta_1 = 1$) are drawn in Figs. 4.2 – 4.4 under the action of fluid injection or mass withdrawal. The radial velocity distribution is depicted in Fig. 4.2 for the prescribed values of suction/injection parameter H_w . The impermeable disk case ($H_w = 0$) is better to observe first for which the flow is centripetal near the disk and centrifugal near the cone. In this situation both the centripetal and centrifugal flows do co-exist simultaneously. But, as the mass removal ($H_w < 0$) is introduced at the disk surface, the centripetal flow starts to dominate. It is depicted (in Fig. 4.2) that the centripetal flow gradually strengthens and extends towards the cone region upon continuous strengthening the mass removal parameter H_w . Ultimately a stage is reached when the centrifugal flow vanishes completely and there is only the centripetal flow within the whole gap. The value of H_w for which this situation is achieved is called the minimum threshold value $H_{w,Thrs}^{Suc}$ of H_w for which the total radial flow in the gap becomes centripetal and is calculated to be $H_{w,Thrs}^{Suc} = -1.384$. This means that the fluid drawn out, at the disk surface, supports the centripetal flow on the disk and radially draws the more fluid into the gap which consequently reduces the centrifugal flow near the cone. Analogously, a reverse of this situation is observed for the mass injection case. The centrifugal flow can be seen to extend towards the disk surface as one continuously increases the mass injection velocity at the disk surface. In this case too there exists a minimum threshold value $H_{w,Thrs}^{Inj}$ of H_w for which the entire radial flow within the gap becomes centrifugal. This particular value of H_w is calculated as $H_{w,Thrs}^{Inj} = 1.1$ (see Fig. 4.2).

Tangential velocity component under the influence of fluid injection or mass withdrawal in a large conical gap has been plotted in Fig. 4.3. Slope of tangential velocity component rises as suction becomes stronger (see Fig. 4.3) which means that the flow establishes within the gap; whereas the blowing depreciates the flow which ultimately correspond to decrease the velocity gradient at the rotating disk. The effects of suction/injection on axial velocity component have also been depicted in Fig. 4.4. Obviously, the magnitude of the axial velocity is higher in the case of fluid injection; which is somewhat a trivial fact. The pressure distribution is also greatly influenced by

the mass withdrawal and blowing phenomena. A decrease in pressure is noticed when the mass is drawn out from the disk surface (see Fig. 4.5) whereas blowing has an opposite effect and leads to increase the pressure in the gap and on the disk surface, also.

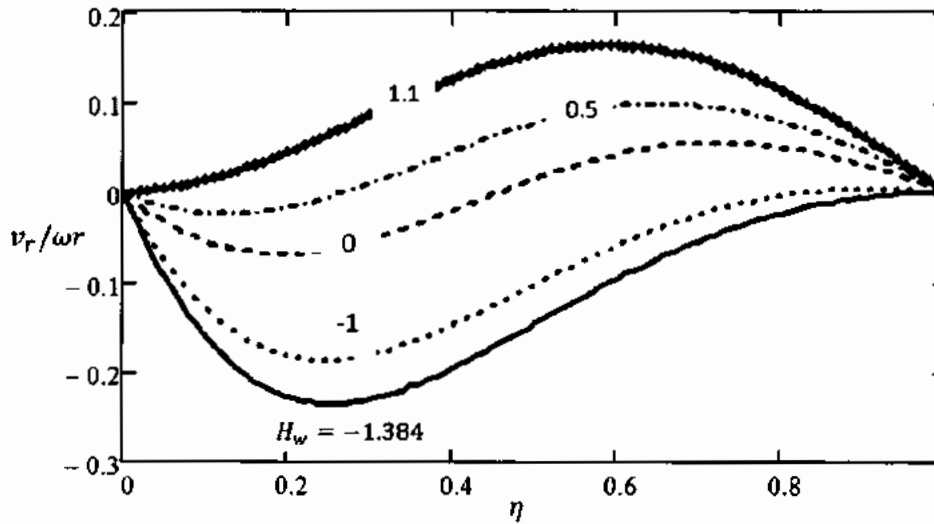


Fig. 4.2: Dimensionless mass transfer parameter effects on radial-velocity distribution in a large conical gap between a rotating cone and stationary permeable disk.

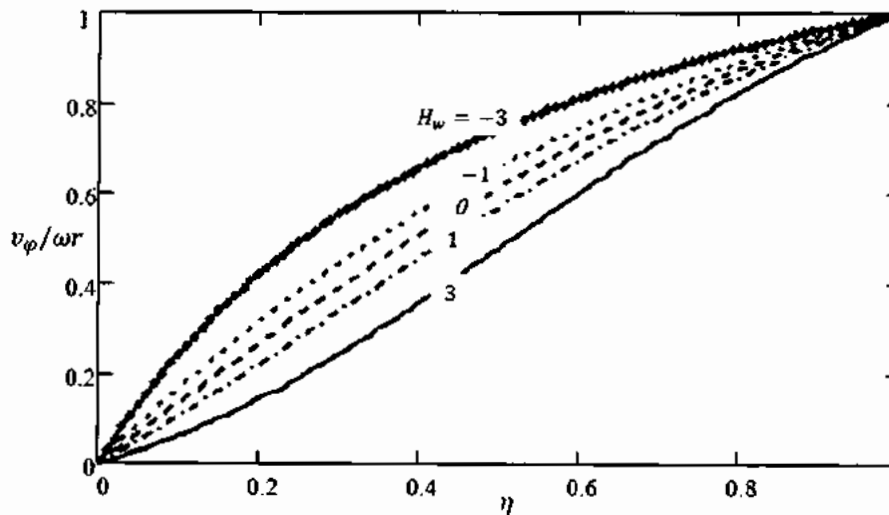


Fig. 4.3: Dimensionless mass transfer parameter effects on tangential velocity distribution in a large conical gap between a rotating cone and stationary permeable disk.

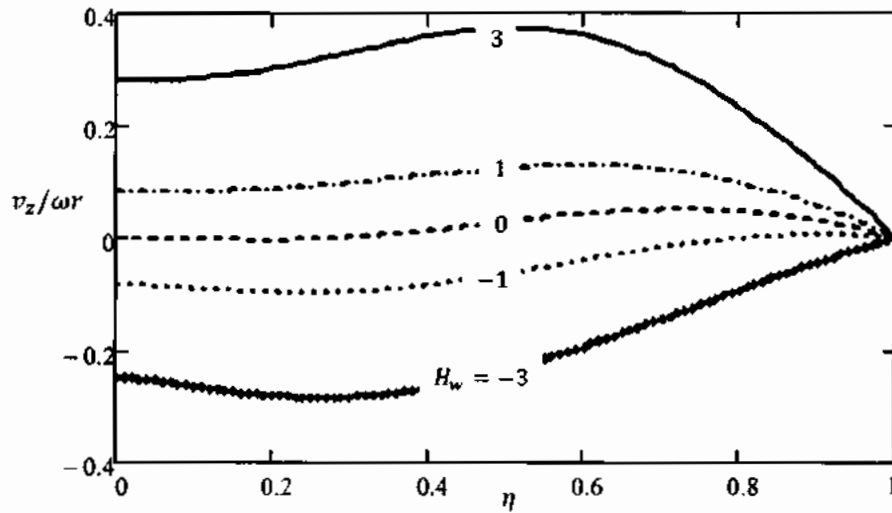


Fig. 4.4: Dimensionless mass transfer parameter effects on axial velocity distribution in a large conical gap between a rotating cone and stationary permeable disk.

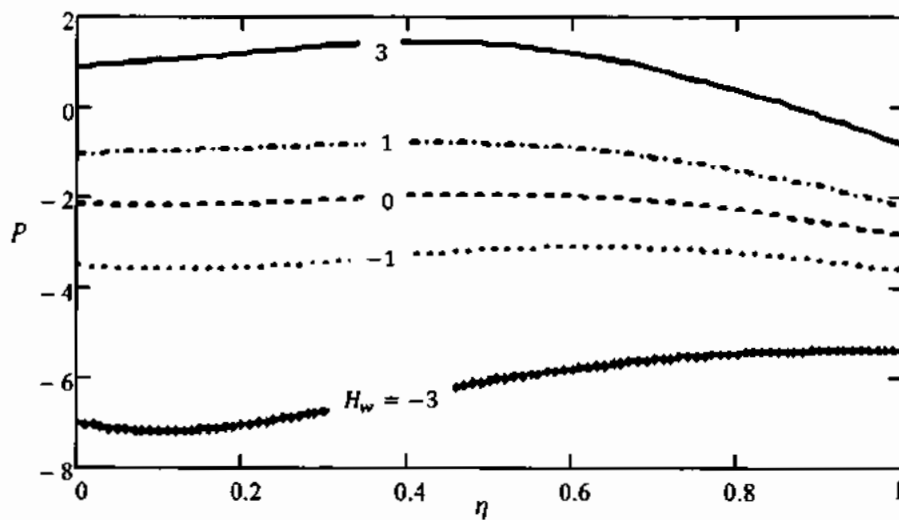
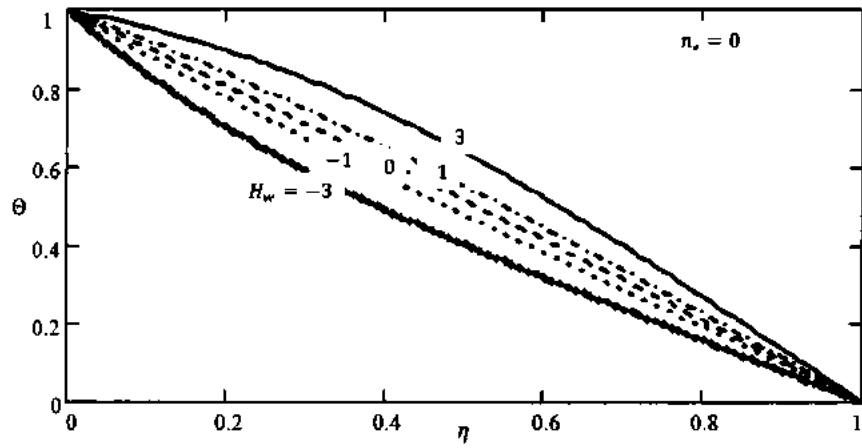


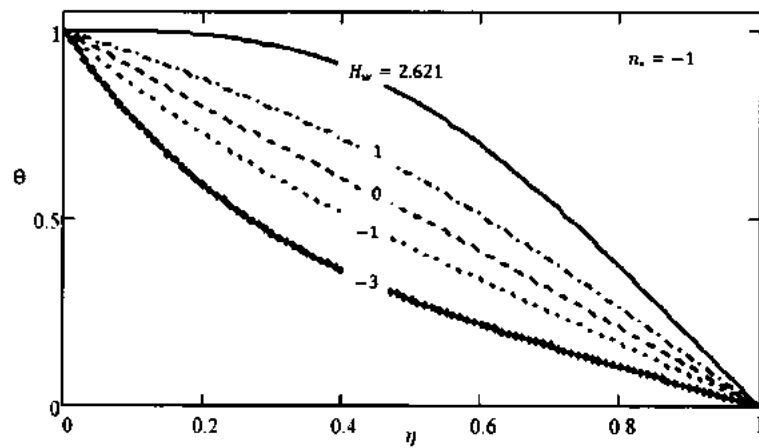
Fig. 4.5: Dimensionless mass transfer parameter effects on pressure in a large conical gap between a rotating cone and stationary permeable disk.

Temperature profiles are plotted in Figs. 4.6 (i – iii) for various values of n_s ($= -1, 0$ & 2). A downward shifting of temperature curves can be noticed in Figs. 4.6 (i & ii) exhibiting increased wall temperature gradients, as one assumes the decreasing values of dimensionless velocity H_w . This clearly highlights the key role of wall suction velocity towards the convective heat transfer enhancement for the cases $n_s = 0.0$ and $n_s = -1.0$ (see Fig. 4.6 (i & ii)). But, on the other hand, when the fluid (having the

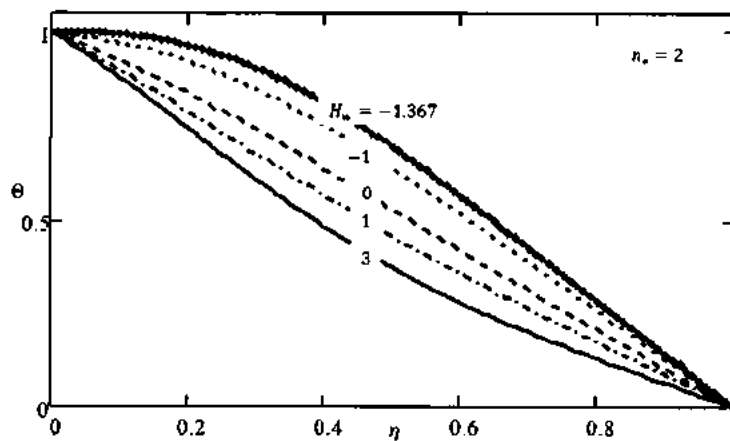
same temperature as that of disk) is injected through the disk, it leads to flatten the temperature curves. These effects are more pronounced when one considers the strong wall blowing. Eventually, at $H_w = 2.621$ ($n_* = -1$), 15 ($n_* = 0$), the injected fluid behaves as an insulating layer which corresponds to no heat transfer from the disk surface (see Figs. 4.6 (ii)). This phenomena can also be observed from Fig. 4.7 where Nusselt number ($Nu = -\theta'(0)$) hits the zero value at corresponding values of $H_w = 2.621$ & 15 . But for $n_* = 1$ & 2 , it takes large values of H_w (greater than 20) to vanish the heat transfer rate. These values are not evaluated in this study as solution is more sensitive and highly dependent upon the initial guess which requires the extra efforts. Similarly for the small conical gap heat transfer seizes at $H_w \approx 220$ for the considered values of n_* . Interestingly, the role of suction/injection gets reversed when one assumes $n_* > 0.0$ (see Figs. 4.6(iii) & 4.7) i.e. the fluid injection is now responsible for the heat transfer enhancement and suction results to decrease the heat transfer rate. Ultimately the flattened temperature curves (for $n_* = 2.0$) are obtained at $H_w = -1.367$ where no heat transfer is observed (see also Fig. 4.7, $n_* = 2.0$). Heat transfer enhancement due to fluid injection is given quantitatively in Table 4.1 where it can be noticed that the trend in heat transfer enhancement is the same for small conical gap, also. For instance, corresponding to the fixed value $H_w = -2$, heat transfer is enhanced by 6% and (almost) by 4% when $n_* = -1$ & 0 , respectively, with small gap ($\eta_1 = 0.0698$), and 99% and 52% for large gap ($\eta_1 = 1$), respectively. For the radially increasing temperature, an enhancement of 0.9% ($n_* = 1$) & 44% ($n_* = 2$) for the large gap and 0.05% ($n_* = 1$) & 5.6% ($n_* = 2$) for the small gap are achieved. With the availability of this quantitative data it is noticed that the heat transfer enhancement in the mass injection case is not that rapid as it is in the suction case. Interestingly, radially decreasing temperature case corresponds to highest enhancement in the heat transfer rate. The reason behind this fact is that the suction causes the centripetal flow and the injection causes the centrifugal flow. In the case ($n > 0$) the disk temperature is higher near the rim and lower near the center. When the radially inward (centripetal) flow enhances, it brings the hotter fluid towards the cooler region which ultimately reverses the cooling process.



(i)



(ii)



(iii)

Fig. 4.6: Dimensionless mass transfer parameter effects on temperature distribution in a large conical gap between a rotating cone and stationary permeable disk. (i) $n_s = 0.0$, (ii) $n_s = -1.0$ & (iii) $n_s = 2.0$.

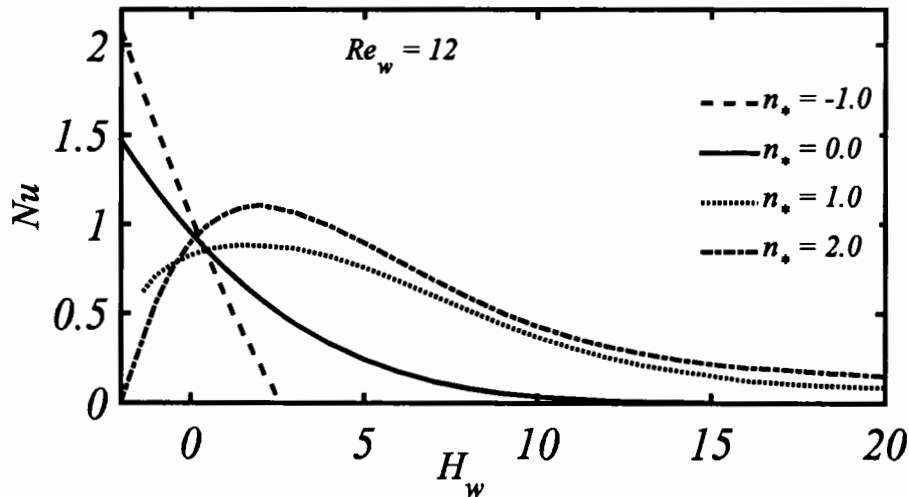


Fig. 4.7: Heat transfer rate as a function of dimensionless mass transfer parameter in a large conical gap between a rotating cone and stationary permeable disk.

Table 4.1: Data of heat transfer rate, rotating cone and stationary permeable disk.

H_w	$Re_\omega = 12$ (large conical gap)				$Re_\omega = 2463$ (small conical gap)			
	$n_* = -1$	$n_* = 0$	$n_* = 1$	$n_* = 2$	$n_* = -1$	$n_* = 0$	$n_* = 1$	$n_* = 2$
-2.0	2.084	1.473	0.621		16.189	13.878	11.410	8.768
-1.2	1.649	1.246	0.755	0.136	15.822	13.685	11.418	9.006
-0.4	1.241	1.045	0.834	0.606	15.458	13.495	11.424	9.235
0.0	1.047	0.954	0.858	0.759	15.276	13.401	11.427	9.346
0.5	0.816	0.849	0.876	0.899	15.051	13.283	11.429	9.481
1.0	0.599	0.752	0.882	0.995	14.826	13.167	11.431	9.613
2.0	0.209	0.583	0.866	1.093	14.379	12.936	11.433	9.866

Case II: Rotating permeable disk and stationary cone

This is a reverse of the above case which obviously causes to reverse the associated phenomena. Now the centripetal flow shifts to the cone region and the centrifugal flow happens to appear near the porous disk. The influence of mass withdrawal or blowing has been the same on velocity as well as on temperature profiles in this case also where the more removal/supply in the form of suction/injection can diminish the occurring of centrifugal and centripetal flows, respectively. However, from Fig. 4.8 it can be seen that the threshold values for diminishing the heat transfer phenomenon are altered i.e. $H_w = 2.2065$ ($n_* = -1$), 15 ($n_* = 0$), 20 ($n_* = 1$) and $H_w = -1.9032$ ($n_* = 2$); which is also an obvious fact, now. The threshold values for small gap again exist for the large value of $H_w \approx 220$ for considered value of n_* . The heat transfer increment for suction ($H_w = -2$) inside the large and small gap situations are, respectively, 112% & 7% ($n_* = -1$) and 51% & 3% ($n_* = 0$), whereas, for the

fluid injection ($H_w = 2$) it is 21% & 2% ($n_* = 2$), respectively (see Table 4.2). Again in the situation of radially decreasing distribution of the disk temperature the heat transfer increment is the largest and it is in fact also greater than the value obtained in the previous case which is 99% with the same temperature distribution. This indicates that the efficiency of cone-disk arrangement, used in cooling processes, can be higher for a rotating porous disk (subject to mass removal) with radially decreasing temperature and a stationary cone.

Table 4.2: Data of heat transfer rate, stationary cone and permeable rotating disk.

H_w	$Re_\omega = 12$				$Re_\omega = 2463$			
	$n_* = -1$	$n_* = 0$	$n_* = 1$	$n_* = 2$	$n_* = -1$	$n_* = 0$	$n_* = 1$	$n_* = 2$
-2.0	2.032	1.572	0.919		14.310	15.858	17.347	18.779
-1.2	1.585	1.341	1.038	0.646	13.918	15.655	17.323	18.927
-0.4	1.162	1.135	1.103	1.065	13.528	15.453	17.298	19.067
0.0	0.960	1.041	1.120	1.197	13.334	15.353	17.284	19.134
0.5	0.719	0.931	1.128	1.312	13.093	15.228	17.267	19.215
1.0	0.490	0.830	1.125	1.385	12.852	15.104	17.249	19.293
2.0	0.076	0.651	1.090	1.443	12.373	14.859	17.210	19.440

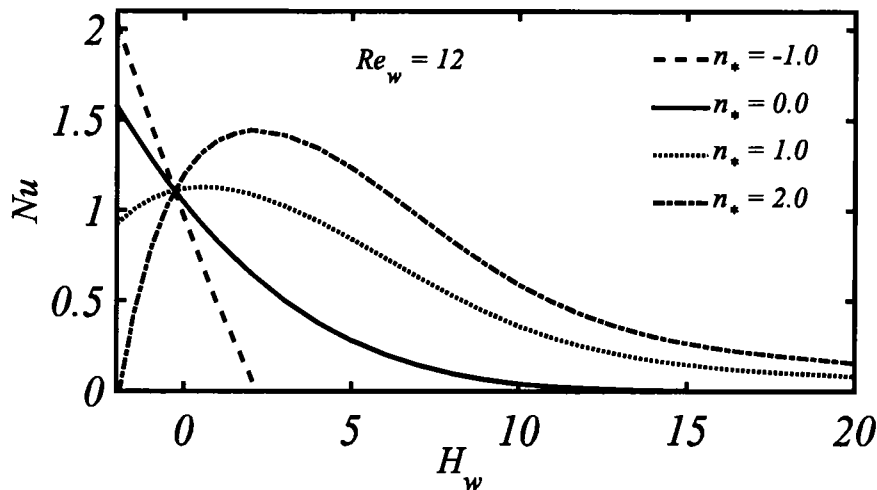


Fig. 4.8: Heat transfer rate as a function of dimensionless mass transfer parameter in a large conical gap between a stationary cone and permeable rotating disk.

Case III: Co-rotating cone and permeable disk

The flow pattern in the current case is characterized by the ratio (Re_Ω/Re_ω). If cone rotates faster ($Re_\omega > Re_\Omega$), motion of the fluid is centripetal over the disk and centrifugal near the cone. The flow pattern is reversed when disk revolves faster ($Re_\Omega > Re_\omega$). Therefore, it is important to investigate the situation when both the disk and cone rotate almost with identical velocities ($Re_\omega = 1.01 Re_\Omega$ or $Re_\omega = 0.99 Re_\Omega$). Table 4.3

contains the numerical values of heat transfer rate with the effects of suction/injection when the ratio (Re_Ω/Re_ω) is 0.99. The threshold values of H_w are 2.4223 ($n_* = -1$), 15 ($n_* = 0$), 20 ($n_* = 1$) & -1.71754 ($n_* = 2$) for which no heat transfer (see Fig. 4.9) is found for a large gap ($\eta_1 = 1$). Similar to the above two cases such threshold values exist at $H_w \approx 220$ for small conical gap. According to Table 4.3 the augmentation in heat transfer rate for mass removal ($H_w = -2$) in a large and small gap are, respectively, 105% & (almost) 7% ($n_* = -1$) and 53% & (almost) 4% ($n_* = 0$), whereas for the blowing ($H_w = 2$) it is 25% & 2% ($n_* = 2$), respectively.

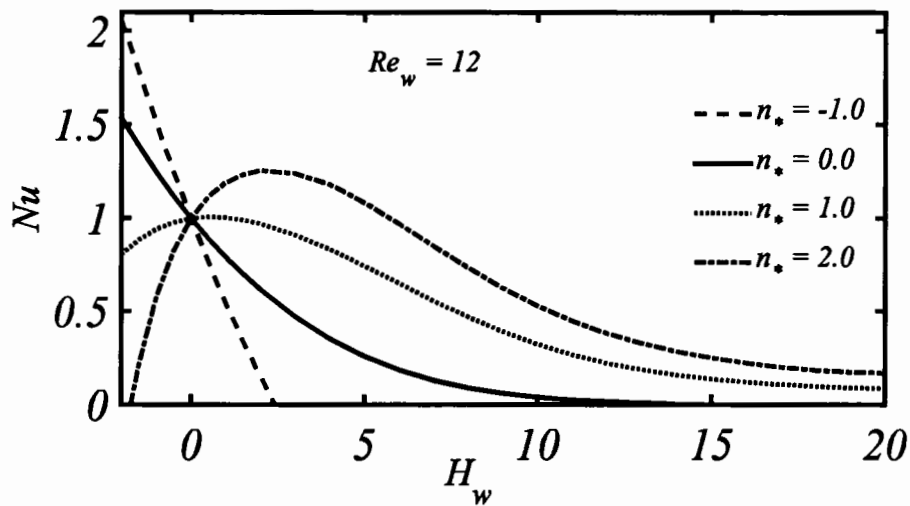


Fig. 4.9: Heat transfer rate as a function of dimensionless mass transfer parameter in a large conical gap between a co-rotating cone and permeable disk.

Table 4.3: Data of heat transfer rate, co-rotating cone and permeable disk.

H_w	$Re_\omega = 12$				$Re_\omega = 2463$			
	$n_* = -1$	$n_* = 0$	$n_* = 1$	$n_* = 2$	$n_* = -1$	$n_* = 0$	$n_* = 1$	$n_* = 2$
-2.0	2.051	1.533	0.810		15.239	14.848	14.448	14.040
-1.2	1.611	1.301	0.925	0.453	14.864	14.646	14.425	14.202
-0.4	1.196	1.095	0.987	0.872	14.491	14.446	14.400	14.355
0.0	0.999	1.001	1.003	1.004	14.306	14.346	14.387	14.428
0.5	0.764	0.892	1.010	1.121	14.075	14.223	14.370	14.516
1.0	0.542	0.791	1.007	1.196	13.845	14.100	14.352	14.601
2.0	0.145	0.615	0.973	1.259	13.389	13.856	14.313	14.761

Case IV: Counter-rotating cone and permeable disk

First consider the impermeable disk ($H_w = 0$) in which most complicated radial flow pattern is exhibited by both the cone and the disk. In fact centrifugal flow exists over the disk and cone whereas centripetal at the in-between region (center) of the

conical gap. Mass withdrawal has an interesting effects on this centripetal flow (in the central part of the gap) and its region can be extended towards the disk and cone due to the increased wall suction. Particularly, for $H_w = -0.6$, disk rotation effects are almost negligible and at $H_w = -1.91$ fully centrifugal flow is observed in the whole gap region and over the disk and the cone as well. But again a reverse behavior in the flow pattern is observed when blowing is considered, as shown in Fig. 4.10. Table 4.4 gives the detailed information about the different flow situations due to the mass withdrawal or fluid injection. Heat transfer has been affected in the same manner as like the previous cases discussed above. The computations of Nusselt number (over the disk surface) with the influences of suction/injection are depicted in Table 4.5. Heat transfer augmentation (for $n_* \leq 0$) and diminution (for $n_* > 0$) can clearly be seen when greater mass is sucked from the disk surface (refer to Fig. 4.11). Heat transfer is diminished at $H_w = -1.4848$ ($n_* = 2$). The fluid injection has an opposite role and zero heat transfer is observed at $H_w = 2.3562$ ($n_* = -1$), 15 ($n_* = 0$) & 20 ($n_* = 1$). According to Table 4.5 the intensification in heat transfer with mass removal ($H_w = -2$) are 105% & 7% ($n_* = -1$) and 51% & 3% ($n_* = 0$) for the large and small gap situations, respectively, whereas for the blowing ($H_w = 2$) it is almost 40% & 4% ($n_* = 2$), respectively.

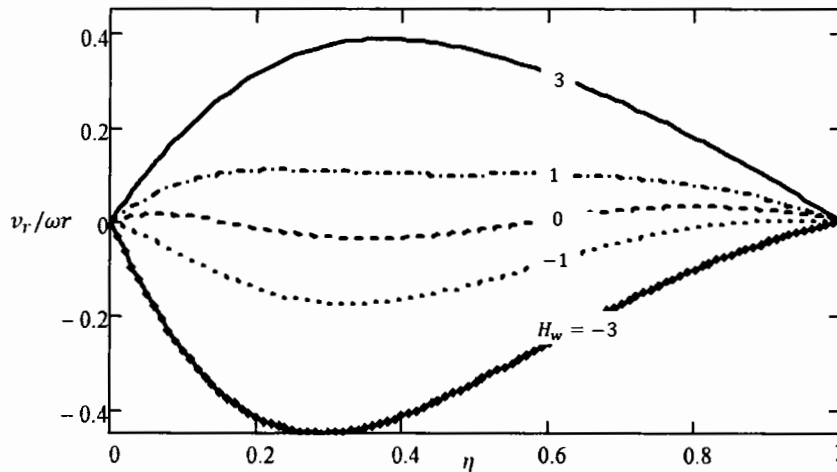


Fig. 4.10: Dimensionless mass transfer parameter effects on radial-velocity distribution in a large conical gap between a counter-rotating cone and permeable disk.

Table 4.4: Situation of centripetal and centrifugal flow under the influence of dimensionless mass transfer parameter in the situation of counter-rotating of porous disk and cone.

H_w	Centripetal flow	Centrifugal flow	Constant
-1.91	100%	-	-
-1.00	85%	15%	-
-0.80	60%	40%	-
0.00	40%	60%	-
0.80	35%	65%	-
1.00	-	78%	22%
1.50	-	90%	10%
2.00	-	93%	7%
3.00	-	94%	6%

Table 4.5: Data of heat transfer rate, counter-rotating cone and permeable disk.

H_w	$Re_\omega = 12$				$Re_\omega = 2463$			
	$n_* = -1$	$n_* = 0$	$n_* = 1$	$n_* = 2$	$n_* = -1$	$n_* = 0$	$n_* = 1$	$n_* = 2$
-2.0	2.072	1.496	0.675		15.187	14.905	14.584	14.218
-1.2	1.630	1.274	0.833	0.264	14.796	14.718	14.613	14.479
-0.4	1.211	1.078	0.933	0.774	14.408	14.532	14.639	14.728
0.0	1.011	0.989	0.966	0.942	14.210	14.440	14.652	14.849
0.5	0.772	0.885	0.993	1.096	13.973	14.325	14.666	14.997
1.0	0.544	0.789	1.007	1.202	13.733	14.211	14.680	15.140
2.0	0.132	0.621	1.002	1.314	13.255	13.984	14.705	15.416

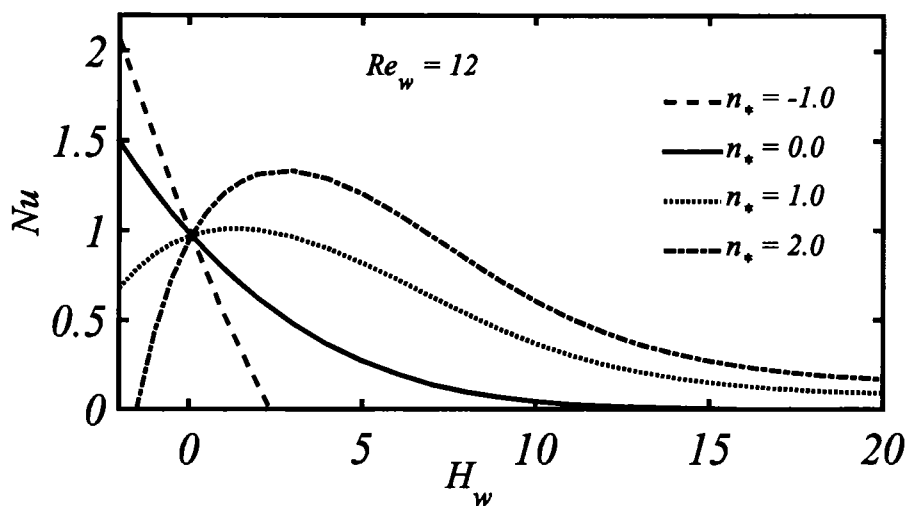


Fig. 4.11: Heat transfer rate as a function of dimensionless mass transfer parameter in a large conical gap between a counter-rotating cone and permeable disk.

CHAPTER 5

Heat Transfer Enhancement from a Non-Isothermal Rotating Disk with Surface Topography

Augmentation in heat transfer rate through wall roughness is a passive technique which is extensively being used in the modern technologies. For the rotating disk geometries its implementation is very rare as the literature does not include any significant works on this topic except a very few. The isothermal rotating wavy disk is available in literature (studied by Le Palec [71]) in which he reported 15% increase in the rate of heat transfer compared to the flat disk case. Such an increased heat transfer rate can further be increased by assuming certain other flow assumptions. An attempt in this regard is made in this chapter in order to acquire the increased heat transfer coefficient when the rotating wavy disk temperature is distributed non-uniformly. The disk temperature is assumed to depend on radial distance in the form of power-law function. In the situation of increasing wall temperature of disk having quadratic function of its radius corresponds to 110% intensification in the overall heat exchange from a hot wavy disk (with two waves and surface roughness ratio equals to 0.1) to the surrounding quiescent air in comparison to the isothermal flat disk. Apart from this, rate of heat transfer from a wavy disk has also been estimated for a very wide range of Prandtl number (10^{-2} to 10^4). In the current analysis some threshold values of exponent of disk temperature distribution has also been manipulated for which the heat transfer rate is seized. The invariant threshold value ($n_s = -2$) of the flat disk is observed to be variant for a non-flat disk case. However, this variation is found to be small for a variety of fluids. Due to the analogy between convective heat transfer and mass transfer phenomena the obtained findings of this study are two fold as they also characterize the mass transfer rate from a wavy rotating disk with a uniform distribution of mass at the disk surface.

5.1 Model description

Consider a non-flat circular disk rotating around its vertical axis with a constant rotation rate ω . The disk is assumed to rotate in a fixed frame due to which Coriolis

forces are absent and the flow resembles to the classical von Kármán's flow. Such a rotating flow is assumed to be steady, viscous, incompressible, with constant thermo physical properties inside and away from the boundary-layer. The effects of viscous dissipation and gravity are neglected. The disk surface is described by the continuous differentiable function $s(r^*) = a_0 \cos(2N\pi r^*)$ which specifies the non-flat surface of the disk as a sinusoidal wavy surface. A schematic diagram of the disk geometry is shown in Fig. 1.4. The so chosen surface topography facilitates a comparison of the current results with those of Le Palec [72], otherwise one is free for choosing any other differentiable form. The governing equations are obtained in an orthogonal curvilinear coordinate system (x, θ, y) in which the direction along the surface of the disk is represented by x , and normal to the surface is y , while the azimuthal direction is described by θ (see Fig. 1.4). The continuity, momentum, energy, and concentration equations for the rotating wavy disk after the utilization of boundary-layer approximations are given in Eqs. (1.11) – (1.15). Where the pressure gradient terms disappeared because of the ambient conditions. These ambient conditions along with wall conditions are specified below.

5.1.1 Boundary conditions

Wall conditions

- (1) No slip condition at the rotating disk surface in the absence of suction/injection correspond to the restriction $v_x = v_y = v_\theta - \omega r = 0$.
- (2) A non-isothermal wall temperature of the power-law form $T_w(r) = T_\infty + c_0 r^{n_*}$ is considered, where n_* characterizes the radially increasing (for $n_* > 0$); radially decreasing ($n_* < 0$), or isothermal ($n_* = 0$) temperature distribution at the disk surface.
- (3) The analogy between heat and mass transfer can be established if one utilizes the constant distribution of concentration on the disk surface, i.e. $C_w = \text{Const}$.

Ambient conditions

- (1) The fluid motion is induced solely due to the disk rotation and the surrounding fluid is quiescent. This certainly gives rise to the condition $v_x = 0 = v_\theta$.
- (2) The ambient temperature of the fluid is given by T_∞ .
- (3) Similar to the ambient temperature a uniform ambient concentration (C_∞) is considered outside the boundary-layer.

5.2 Solution procedure

5.2.1 Non-dimensionalization

In order to obtain the dimensionless form of the governing system we follow the dimensionless variables defined by Le Palec [71] as

$$\begin{aligned} \epsilon = \frac{x}{\lambda}, \quad \eta = \sqrt{\frac{\omega R}{\nu \epsilon}} y, \quad R = r/\lambda. \quad f(\epsilon, \eta) = \sqrt{\frac{\omega R}{\nu \epsilon}} \frac{\psi(x, y)}{\omega r}, \quad g(\epsilon, \eta) = \sqrt{\frac{\omega R}{\nu \epsilon}} \frac{\Psi(x, y)}{\omega r}, \\ \Theta(\epsilon, \eta) = \frac{T - T_\infty}{T_w - T_\infty}, \quad \Phi(\epsilon, \eta) = \frac{C - C_\infty}{C_w - C_\infty}, \end{aligned} \quad (5.1)$$

where the relationship between the velocity components and the stream-functions is given by

$$v_x = \frac{1}{r} \frac{\partial(\psi r)}{\partial y}, \quad v_y = -\frac{1}{r} \frac{\partial(\psi r)}{\partial x}, \quad v_\theta = \frac{\partial \Psi}{\partial y}. \quad (5.2)$$

These dimensionless variables transform the original governing system into the following dimensionless non-similar form:

$$f_{\eta\eta\eta} - \frac{\epsilon}{R} \frac{dR}{d\epsilon} (f_\eta^2 - g_\eta^2) + \left(\frac{1}{2} + \frac{3}{2} \frac{\epsilon}{R} \frac{dR}{d\epsilon} \right) f f_{\eta\eta} = \epsilon (f_\eta f_{\eta\epsilon} - f_{\eta\eta} f_\epsilon), \quad (5.3)$$

$$g_{\eta\eta\eta} - 2 \frac{\epsilon}{R} \frac{dR}{d\epsilon} f_\eta g_\eta + \left(\frac{1}{2} + \frac{3}{2} \frac{\epsilon}{R} \frac{dR}{d\epsilon} \right) f g_{\eta\eta} = \epsilon (f_\eta g_{\eta\epsilon} - g_{\eta\eta} f_\epsilon), \quad (5.4)$$

$$\frac{\Theta_{\eta\eta}}{Pr} + \left(\frac{1}{2} + \frac{3}{2} \frac{\epsilon}{R} \frac{dR}{d\epsilon} \right) f \Theta_\eta - \frac{\epsilon}{R} \frac{dR}{d\epsilon} n_* f_\eta \Theta = \epsilon (f_\eta \Theta_\epsilon - \Theta_\eta f_\epsilon), \quad (5.5)$$

$$\frac{\Phi_{\eta\eta}}{Sc} + \left(\frac{1}{2} + \frac{3}{2} \frac{\epsilon}{R} \frac{dR}{d\epsilon} \right) f \Phi_\eta = \epsilon (f_\eta \Phi_\epsilon - \Phi_\eta f_\epsilon). \quad (5.6)$$

Notice that Eqs. (5.5) and (5.6) admit the same solution whenever the parameters Pr and Sc take the same values (at $n_* = 0$). This means that the solution of Eq. (5.5) can serve as the solution of Eq. (5.6) ($n_* = 0$) by designating the same values to Sc as designating to Pr . Because of this analogy we shall prefer to solve Eq. (5.5) only and to use the same solution for Φ by assigning the same values to Sc to Pr . By using Eqs. (5.1) & (5.2) the boundary conditions defined in Sec. 5.1.1 can be transformed as

$$\left. \begin{aligned} f = g = f_\eta = g_\eta - 1 = \Theta - 1 = \Phi - 1 = 0, & \quad \text{at } \eta = 0 \\ f_\eta = 0, \quad g_\eta = 0, \quad \Theta = 0, \quad \Phi = 0, & \quad \text{at } \eta = \infty \end{aligned} \right\} \quad (5.7)$$

5.2.2 Numerical method

An implicit finite difference scheme commonly known as Keller-box method has been implemented to acquire the solution of non-similar Eqs. (5.3) – (5.7). The commercial tool MATLAB was used for this numerical solution. The program has been validated by reproducing heat transfer data for a non-isothermal rotating flat disk, already studied by Shevchuk [37]. The comparison of the two data is presented in Tale 5.1 where an excellent matching of the two data can be seen. Apart from this, several

runs were also made in order to acquire the grid independence of the data, especially for the large Prandtl (Schmidt) numbers. Finally, the results were obtained by setting $\Delta\eta = 0.001$ for $Pr \gg 1$ and for small values of the Prandtl number ($Pr \ll 1$) $\Delta\eta = 0.01$ was used. However, for the values $Pr < 1$ the outer edge of the boundary-layer varies with Pr . For example, for $Pr = 0.1$ the outer edge of the boundary-layer is taken as $\eta_\infty = 90$ which rapidly increases to the value $\eta_\infty = 700$ for $Pr = 0.01$. It is important to mention here that our results of the Nusselt number (local and average), depicted graphically for isothermal case (i.e. $n_* = 0$), for the rotating sinusoidal-shaped disk for $Pr = 0.71$ are identical to the results of Le Palec [71] which indeed shows the validation of the current method.

Table 5.1: Comparison of data of heat transfer rates for non-isothermal flat disk.

$Pr(Sc)$	$n_* = -2$		$n_* = -1$		$n_* = 0$		$n_* = 2$	
	Shevchuk [37]	Present	Shevchuk [37]	Present	Shevchuk [37]	Present	Shevchuk [37]	Present
10^{-2}	0.00000	0.00000	0.00438	0.00438	0.00871	0.00871	0.01726	0.01726
10^{-1}	0.00000	0.00000	0.0399	0.0400	0.0766	0.0766	0.1417	0.1417
10^0	0.00000	0.00000	0.3221	0.3221	0.3963	0.3963	0.6159	0.6159
10^1	0.00000	0.00000	0.7368	0.7368	1.1341	1.1341	1.6206	1.6205
10^2	0.00000	0.00000	1.8009	1.8009	2.6871	2.6871	3.7422	3.7421
10^3	0.00000	0.00000	4.0802	4.0802	6.0162	6.0160	8.2972	8.2973
10^4	0.00000	0.00000	8.9846	8.9849	13.181	13.181	18.104	18.105

5.2.3 Quantities of physical interest

The dimensionless temperature gradient at the disk surface is an important engineering quantity which represents the rate of heat transfer from the heated disk to the surrounding fluid. Owing to the surface roughness heat transfer rate can be analyzed as locally and globally. The local Nusselt (Sherwood) number, $Re_\omega^{-1/2} Nu = \sqrt{\frac{R}{\epsilon}} \Theta_\eta(0)$ ($Re_\omega^{-1/2} Sh = \sqrt{\frac{R}{\epsilon}} \Phi_\eta(0)$) predicts the local heat (mass) transfer rate whose dependence upon the local locations on the disk surface is obvious from this expression. The overall estimation of the heat transfer can, however, be made by calculating the average Nusselt number. The calculation of average Nusselt number does also facilitate one to make the comparison among the wavy disk situation and the flat disk situation. With the aid of above expression of local Nusselt (Sherwood) number it is possible to define the average Nusselt (Sherwood) number as

$$\overline{Nu} Re_\omega^{-1/2} = \frac{1}{S} \int_S Re_\omega^{-1/2} Nu \, dS \quad \left(\overline{Sh} Re_\omega^{-1/2} = \frac{1}{S} \int_S Re_\omega^{-1/2} Sh \, dS \right). \quad (5.8)$$

The impact of surface roughness can be calculated with the use of flat disk area (πb^2) as a reference. This leads to an average Nusselt (Sherwood) number of the form

$$\overline{Nu}_p = \overline{Nu} \frac{S}{\pi b^2} \left(\overline{Sh}_p = \overline{Sh} \frac{S}{\pi b^2} \right). \quad (5.9)$$

For the smooth disk $S = \pi b^2$ and consequently one obtains $\overline{Nu}_p = \overline{Nu}$ ($\overline{Sh}_p = \overline{Sh}$).

5.3 Heat transfer analysis

The analysis of heat (mass) transfer phenomena strongly depends upon the involved physical quantities. In this regard four physical parameters are involved in this study, namely; (i) the surface roughness ratio (a_0/λ), (ii) the number of sinusoids (N), (iii) the Prandtl (Pr) (Schmidt (Sc)) number, and (iv) the temperature distribution exponent (n_*), among which all influence the heat transfer rate significantly. The parameters (i) and (ii) characterize the surface roughness, whereas (iii) represents the nature of the fluid and (iv) enables the rotating disk to be non-isothermal. The influence of Prandtl number upon the heat transfer rate is first elucidated by varying it over a very wide range i.e. from 10^{-2} to 10^4 . Its impact on temperature profile in the presence of surface roughness ($a_0/\lambda = 0.1$) is shown in Fig. 5.1. A rapid increase is observed in the thermal boundary-layer thickness for small values of Pr while keeping other parameters fixed, whereas the larger values of Pr make the boundary-layer thinner. Such thinning of the boundary-layer is also found to depend on increasing values of the temperature distribution exponent n_* (depicted in Fig. 5.2). This means that the higher values of Pr and n_* lead to enhance the heat transfer rate at disk surface. These increased rates of heat transfer are quantized in Table 5.2 corresponding to various values of the involved parameters. Due to the presence of surface roughness, the values of \overline{Nu}_p have been manipulated in this Table. It is found that the impact of Prandtl number remains the same for wavy disk also. Interestingly, for $Pr = 1$ the value of \overline{Nu}_p enhances by 3.27 times with an increase in exponent n_* from -1 to 4 whether the disk is flat or sinusoidal. It is also fascinating to note that for $Pr = 10^4$, the corresponding value increases up to 2.38 times over the same range of n_* with and without surface roughness. Therefore, one can say that higher values of Prandtl number weakens the influence of temperature distribution exponent n_* for a sinusoidal-shaped disk, also. These influences were already reported in literature by Shevchuk [37] for a flat rotating disk. From Table 5.2,

one also notices that an increase in Pr results to increase the heat transfer rate for the wavy disk. Almost 28 times enhancement in the overall heat transfer rate is observed when Pr is varied from 10^0 to 10^4 at $n_* = 4$ for both types of disks (either smooth or sinusoidal). But a clear quantitative difference between the values of heat transfer rate of smooth ($a_0/\lambda = 0$) and wavy ($a_0/\lambda = 0.0625$ & 0.1) disks can also be seen in this Table showing more transfer of heat due to the rough rotating disk. For the fixed Prandtl number and exponent index, the increase in the roughness ratio of sinusoidal disk causes to further enhance the heat exchange at the disk surface. Almost 5% enhancement in heat transfer is observed for roughness ratio equals to 0.1 by keeping $Pr = 1.0$ & varying $n_* = -1.0$ to 4.0. Furthermore for all considered range of Prandtl number and temperature distribution exponent, the surface roughness (for surface roughness ratio = 0.1) contributes almost 1.04 times in the augmentation of heat transfer rate. From Table 5.2, it can also be seen that the variation in n_* from 0 to 4 corresponds to 101% enhancement in heat transfer rate for a flat disk situation. But the incorporation of the surface roughness ($a_0/\lambda = 0.1, N = 2$) leads to further enhance this value up to 110% in comparison to the isothermal flat disk (i.e. numerically heat transfer rate is increased from 0.3259 to 0.6842). The data reported in Table 5.2 indicates that the heat transfer rate increases significantly by increasing the height of bumpy surface. But it is also important to note here that the height of bumpy surface (a_0/λ) is taken small enough so that they (surface bumps) do neither cause any flow separation nor they give rise to any secondary flow. The dependence of the local Nusselt number on temperature distribution exponent n_* under the influence of the wavy texture parameter (a_0/λ) is depicted in Fig. 5.3 which reveals the periodic nature of the thermal profile due to the impact of surface waviness for each exponent n_* . Similar trend is observed when the local Nusselt number is plotted for various values of Pr and a_0/λ (see Fig. 5.4). In contrast to the geometry of the disk a double periodicity is exhibited by the local Nusselt number with decreasing amplitude as one departs from the axis of rotation for all considered values of n_* . A similar trend of the local heat transfer rate under the influence of Prandtl number with quadratic law of radially increasing temperature distribution of rough disk are also shown in Fig. 5.4. The local heat exchange at the surface of the disk is higher for larger Prandtl numbers for smooth as well as rough disk.

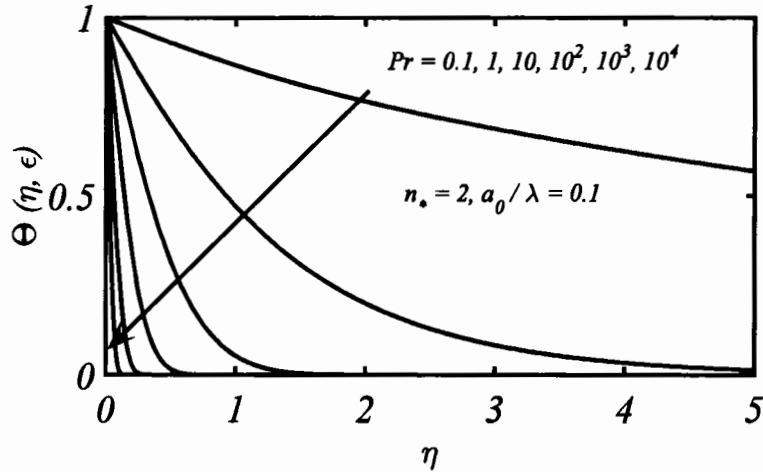


Fig. 5.1: Temperature profile for different values of the Prandtl number.

Table 5.2: Values of $\overline{Nu}_p(\overline{Sh}_p)$ at $N = 2$.

$Pr(Sc)$	a_0/λ	$n_* = -1$	$n_* = 0$	$n_* = 1$	$n_* = 2$	$n_* = 4$
0.01	0	0.0044	0.0087	0.01301	0.0173	0.0256
	1/16	0.00532	0.00971	0.01406	0.01836	0.02685
0.1	0	0.0400	0.0766	0.1104	0.1417	0.1982
	1/16	0.0411	0.0783	0.1127	0.1446	0.2021
	1/10	0.0426	0.0808	0.1160	0.1487	0.2076
0.71	0	0.1893	0.3259	0.4319	0.5185	0.6555
	1/16	0.1928	0.3318	0.4397	0.5279	0.6674
	1/10	0.1979	0.3403	0.4510	0.5413	0.6842
1.0	0	0.2352	0.3963	0.5180	0.6159	0.7693
	1/16	0.2395	0.4035	0.5274	0.6271	0.7832
	1/10	0.2457	0.4137	0.5407	0.6428	0.8028
5.0	0	0.5444	0.8533	1.0697	1.2382	1.4971
	1/16	0.5544	0.8688	1.0891	1.2605	1.5241
	1/10	0.5670	0.8900	1.1161	1.2920	1.5623
10.0	0	0.7368	1.1341	1.4083	1.6205	1.9460
	1/16	0.7502	1.1548	1.4339	1.6499	1.9812
	1/10	0.7667	1.1825	1.4962	1.6909	2.0308
100	0	1.8009	2.6871	3.2840	3.7421	4.4421
	1/16	1.8334	2.7359	3.3435	3.8098	4.5222
	1/10	1.8714	2.8007	3.4251	3.9040	4.6351
500	0	3.2033	4.7351	5.7596	6.5441	7.7413
	1/16	3.2609	4.8211	5.8640	6.6625	7.8809
	1/10	3.3276	4.9348	6.0070	6.8271	8.0777
1000	0	4.0802	6.0160	7.3083	8.2973	9.8058
	1/16	4.1535	6.1253	7.4408	8.4474	9.9827
	1/10	4.2383	6.2696	7.6560	8.6560	10.2320
10^4	0	8.9849	13.1813	15.9721	18.1054	21.3573
	1/16	9.1463	13.4209	16.2620	18.4333	21.7430
	1/10	9.3318	13.7364	16.6579	18.8883	22.2856

Table 5.3: Values of temperature distribution exponent for which heat transfer from the wavy disk (at $N = 2$) is seized.

a_0/λ	$Pr(Sc)$							
	0.1	0.71	1	5	10	100	1000	10000
0.0	-2	-2	-2	-2	-2	-2	-2	-2
1/16	-2	-2	-2	-1.9999	-1.9998	-1.9995	-1.9994	-1.99937
1/10	-1.9996	-1.9996	-1.9995	-1.9993	-1.9990	-1.9932	-1.9927	-1.9925

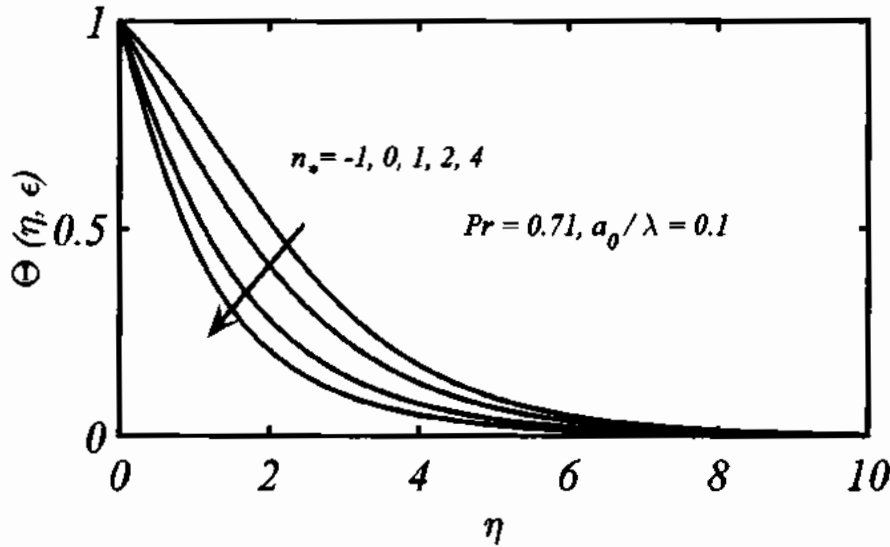


Fig. 5.2: Temperature profile for different values of the disk temperature distribution exponent n_s (the curve $n_s = 0$ also characterizes the concentration profile at $Sc = 0.71$).

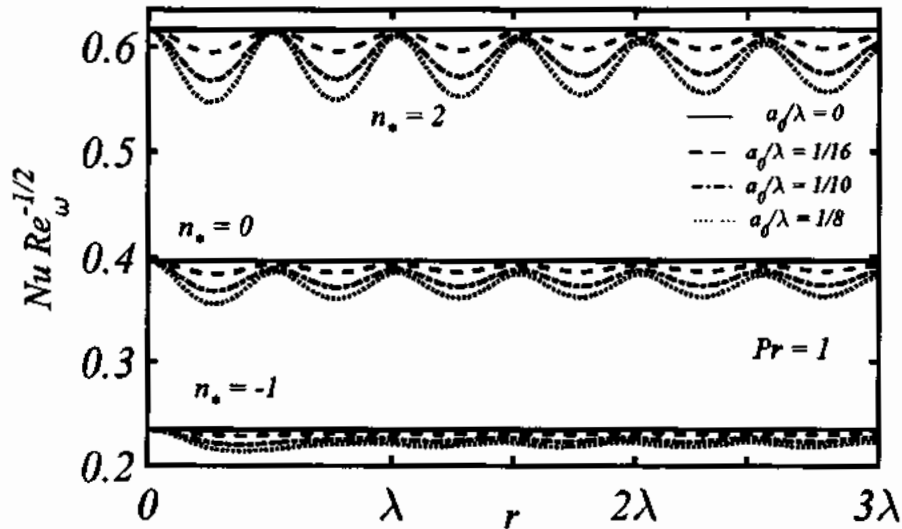


Fig. 5.3: Local Nusselt number variations with surface roughness ratio for a non-isothermal wavy disk (the curve $n_s = 0$ also depicts the local Sherwood number at $Sc = 1$).

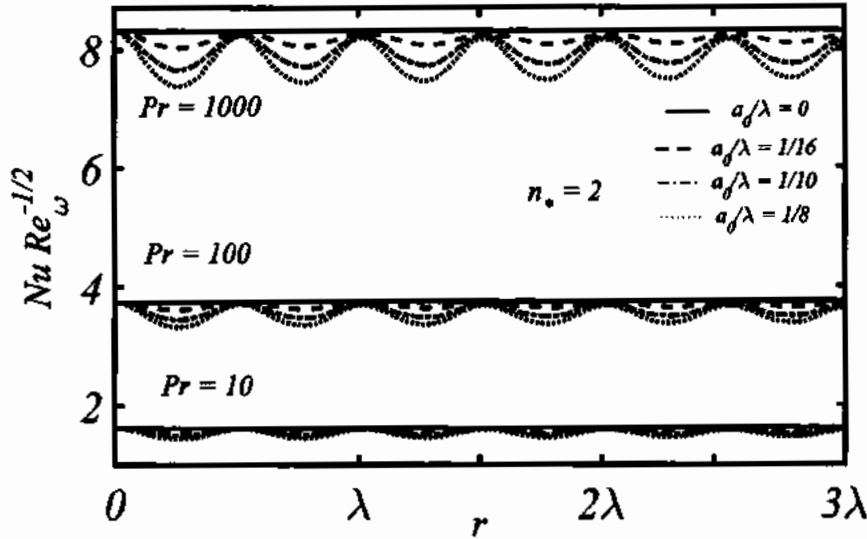


Fig. 5.4: Influence of Prandtl number on local Nusselt number.

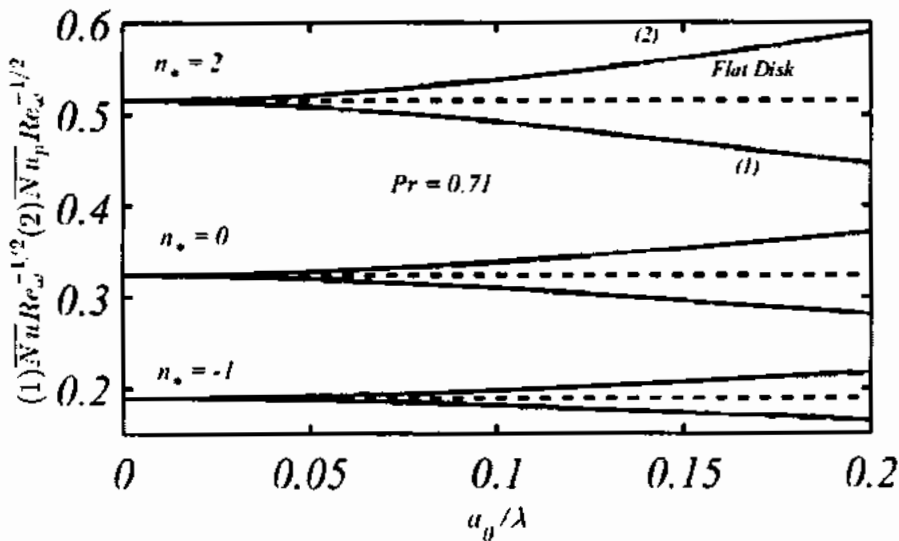


Fig. 5.5: Averaged Nusselt number \overline{Nu} (curve 1) and \overline{Nu}_p (curve 2) under the influence of non-uniform temperature distribution and surface roughness ratio parameters (the curves $n_s = 0$ also correspond the variation of averaged Sherwood numbers \overline{Sh} and \overline{Sh}_p at $Sc = 0.71$).

Average Nusselt numbers \overline{Nu} and \overline{Nu}_p are computed including the area of the wavy disk with the use of the smooth disk area as a reference. Figure 5.5 depicts these values as a function of amplitude – to – wavelength ratio and clearly reflects that the absence of wavy disk area (Eq. (5.8)) shows lower heat transfer rate in comparison to the flat disk (see curve (1) of Fig. 5.5) for increasing values of a_0/λ . But with the inclusion of actual area of the rough disk (Eq. (5.9)), it shows the increased heat transfer rate (curve (2) of Fig. 5.5) for higher values of a_0/λ . Similar pattern is obvious in this Figure for all other chosen values of n_s . It is also noticed that the increase in exponent n_s .

corresponds to higher the values of both \overline{Nu} & \overline{Nu}_p . The influence of the number of sinusoids (N) on the average Nusselt number \overline{Nu}_p for different values of temperature distribution exponent n_* is highlighted in Fig. 5.6. It can be seen that the influence of number of sinusoids on all considered values of n_* is quite weak. It is observed that the multiple waves fitted to the fixed radius of the disk do contribute towards the heat transfer augmentation. However, the augmentation in the heat transfer rate gets weaker with increasing N . From Fig. 5.6 it seems that the impact of number of sinusoids becomes negligible when the parameter N exceeds the value 4. Again, the \overline{Nu}_p obeys a same trend (as observed in Fig. 5.6) for all considered values of n_* apart from a quantitative difference.

From the above discussion, it is realized that the heat transfer rate is reduced when the disk temperature assumes a radially decreasing distribution (i.e. $n_* < 0$); and the heat exchange from the surface of the flat disk to the surrounding is seized at $n_* = -2$, as reported in ref. [37]. Surprisingly this seizing (threshold) value of n_* is found to vary slightly in the considered flow (refer to Table 5.3) due to the wavy nature of the surface. From Table 5.3, it is clear that the threshold value in the presence of surface waviness is found to depend on the Prandtl number quite appreciably, whereas in the case of a flat disk it is independent of the Prandtl number and remains unchanged ($n_{*threshold} = -2$). The influence of surface roughness ratio is also crucial on this critical value where an increase in its value leads to an increase in the critical value also which in turn highlights the role of surface waviness.

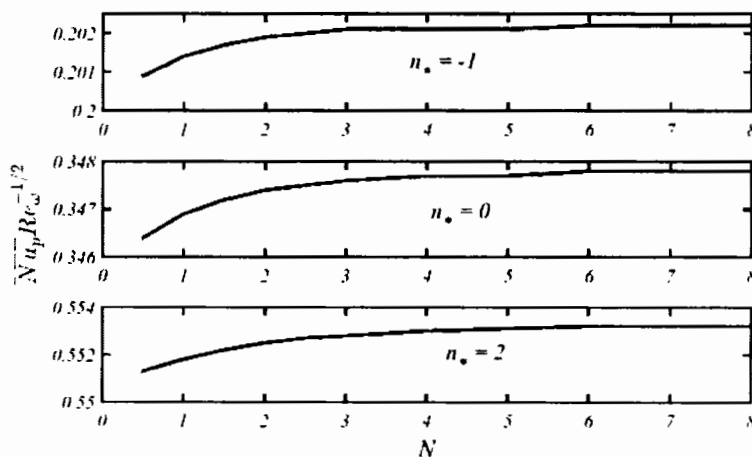


Fig. 5.6: Effects of number of sinusoids on heat transfer rates for various temperature distribution exponent at $Pr = 0.71$ (the curve $n_* = 0$ also represents the mass transfer rate at $Sc = 0.71$).

CHAPTER 6

Heat Transfer from a Wavy Disk Rotating in Forced Flow

The geometric characteristics of the bounding surface and the various flow conditions impart a significant impact on heat transfer augmentation. The surface roughness; the pressure gradient, and the non-uniform disk temperature of the power-law form all attribute to increase the heat transfer rate. These techniques are utilized in this chapter to enhance the convective heat transfer rate in a non-similar boundary-layer flow induced by the rotation of the sinusoidal-shaped disk in a uniform forced stream. The heat transfer coefficient is calculated numerically with the help of Keller - box method. The numerical solution of the governing system is first validated, which is found to be in good agreement with the previous published (theoretical and experimental) results for rotating wavy disk in the absence of external flow ($\frac{a}{\omega} = 0$) and also for a flat disk rotating in a uniform forced stream. It is observed that the impact of surface waviness with a relative motion of fluid and disk on heat transfer rate, shear stresses and shaft torque is quite pronounced and indicates that it is very productive in engineering prospective for the rotating disk systems. Specifically, enhancement of moment coefficient due to waviness of the disk leads to increase the power of wavy disk pump in comparison to the smooth disk. Furthermore, 119%, 174%, 86%, and 86% enhancement in the heat transfer rate (for the case of constant heat flux), the radial shear stress, the tangential shear stress, and the moment coefficient is observed for the wavy disk rotating in forced flow at a fixed $a/\omega = \infty$ and $a_0/\lambda = 0.125$ in comparison to the free rotating flat disk. The considered rough non-isothermal disk rotating in the linear stream of air ($Pr = 0.71$) leads to a significant (about 263%) enhancement in overall heat transfer rate compared to that of the flat free rotating disk when the wavy disk (with two sinusoids) having surface temperature as quartic function of its radial distance. Furthermore, a special attention is also given in identifying the threshold values of the temperature distribution exponent for which the rate of heat transfer is seized from the disk surface and these values are found to depend upon the disk structure only. Furthermore, the present calculations showed that the variation in these

threshold values was not that huge and they remained very close to the flat disk value (i.e. $n_* = -2$) under various circumstances.

6.1 Flow configuration and heat transfer

The alteration of the flat disk surface to the non-flat wavy surface is depicted in Fig. 6.1 with the description of the boundary-layer coordinate system.

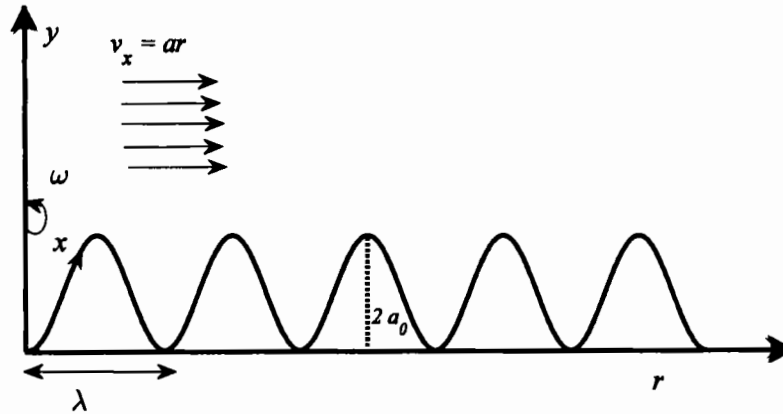


Fig. 6.1: Schematic of the disk geometry and the used coordinate system.

As depicted in Fig. 6.1, the rotating wavy disk is also assumed to be subjected to a linear forced flow. However, the rigid nature of the wavy disk surface and the axially-symmetric nature of the concentric wavy patterns ensure the absence of any wall normal flow and the independence of the dependent quantities from θ . This study considers two cases: first, the disk surface is assumed to be heated in a manner that there exists a constant heat flux throughout the disk surface, second, the disk temperature is assumed to follow the same power-law form as considered in previous chapter. Far away from the disk surface the fluid assumes the ambient temperature denoted by T_∞ . These flow and thermal conditions can be stated, mathematically, as,

$$\left. \begin{aligned} v_x = v_y = v_\theta - \omega r = 0, \quad (i) \quad -k \frac{\partial T}{\partial y} = q, \quad (ii) \quad T_w = T_\infty + c_0 r^{n_*}, \quad \text{at } y = 0 \\ v_x = ar, \quad v_\theta = 0, \quad T = T_\infty, \quad \text{at } y \rightarrow \infty \end{aligned} \right\}. \quad (6.1)$$

The thermal boundary condition (i) will be called as CHF (constant heat flux) case and (ii) will be referred as VWT (variable wall temperature) case in the coming analysis. The presence of external forced stream of fluid gives rise to the pressure variation within the boundary-layer which is determined with the aid of Bernoulli's equation. However, the pressure variations across the boundary-layer are still ignorable.

Therefore, the governing system remains the same as it was in the previous chapter with an additional term $\left(v_x \frac{\partial v_x}{\partial x}\right)_{y \rightarrow \infty}$ appearing in Eq. (1.12) due to the pressure variation outside the boundary-layer.

6.2 Normalization

The normalization of the variables has been carried out in the same manner as it was initially done by Le Palec [71]. However, a little modification is introduced where the disk rotation speed ω has been replaced by the combined rotation rate $\Lambda = (a^2 + \omega^2)^{1/2}$. Therefore, the new independent variables are defined as

$$\epsilon = \frac{x}{\lambda}, \quad \eta = \sqrt{\frac{\Lambda R}{\nu \epsilon}} y, \quad (6.2)$$

whereby the velocity functions have been replaced by their appropriate relations with the stream functions. Therefore, the normalization of the dependent variables is carried out as

$$f(\epsilon, \eta) = \sqrt{\frac{\Lambda R}{\nu \epsilon}} \frac{\psi(x, y)}{\Lambda r}, \quad g(\epsilon, \eta) = \sqrt{\frac{\Lambda R}{\nu \epsilon}} \frac{\Psi(x, y)}{\omega r}, \quad \Theta(\epsilon, \eta) = \frac{T - T_\infty}{T_w - T_\infty} \text{ (VWT)},$$

$$\Theta(\epsilon, \eta) = \frac{(T - T_\infty)}{q} k \sqrt{\frac{\Lambda R}{\nu \epsilon}} \text{ (CHF)}. \quad (6.3)$$

The Eq. (5.3) modifies in the presence of outer radial flow as

$$f_{\eta\eta\eta} - \frac{\epsilon}{R} \frac{dR}{d\epsilon} \left(f_\eta^2 - \left(\frac{\omega}{\Lambda} \right)^2 g_\eta^2 \right) + \left(\frac{1}{2} + \frac{3}{2} \frac{\epsilon}{R} \frac{dR}{d\epsilon} \right) f f_{\eta\eta} + \left(\frac{a}{\Lambda} \right)^2 \frac{\epsilon}{R} \frac{dR}{d\epsilon} = \epsilon (f_\eta f_{\eta\epsilon} - f_{\eta\eta} f_\epsilon), \quad (6.4)$$

and the boundary data transforms to the form

$$\left. \begin{aligned} f = g = f_\eta = g_\eta - 1 = 0, \quad (i) \Theta_\eta + 1 = 0 \quad (ii) \Theta - 1 = 0, \quad \text{at } \eta = 0 \\ f_\eta = \frac{a}{\Lambda}, \quad g_\eta = 0, \quad \Theta = 0, \quad \text{at } \eta = \infty \end{aligned} \right\} \quad (6.5)$$

6.3 Numerical solution

The non-similar Eqs. (6.4), (5.4) and (5.5) subject to boundary conditions (6.5) have been solved numerically by implementing the famous Keller-box method to obtain the velocity and temperature profiles. The validity of the present method is first confirmed by acquiring for isothermal wavy disk case studied by Le Palec [71] and Le Palec et al. [72] (for CHF) by fixing the parameter $\frac{a}{\omega} = 0$. A comparison is made for the case of flat disk rotating in the external forced flow, reported by Mabuchi et al. [79] with the

present numerical procedure and the values are listed in Table 6.1. Our numerical calculations show an excellent agreement with Mabuchi et al. [79] (refer to Table 6.1).

Table 6.1: Comparison of the present numerical calculations with the work of Mabuchi et al. [79].

a/ω	$2f_{\eta\eta}(0)$		$-g_{\eta\eta}(0)$	
	Mabuchi et al. [79]	Present	Mabuchi et al. [79]	Present
0	1.020	1.020	0.6159	0.6159
0.1	1.037	1.037	0.6413	0.6413
0.25	1.124	1.124	0.6991	0.6991
0.5	1.373	1.373	0.8004	0.8004
1	1.871	1.872	0.9334	0.9335
2	2.332	2.333	1.0250	1.0250
∞	2.624	2.624	1.0750	1.0750

6.4 Velocity profiles

6.4.1 Radial component of velocity

The radial velocity component in dimensionless form is displayed in Fig. 6.2 for the surface roughness ratio $a_0/\lambda = 0.1$.

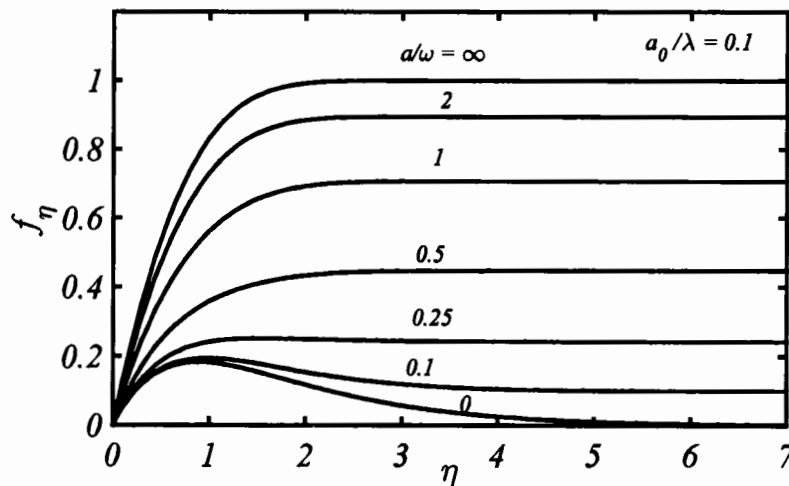


Fig. 6.2: Variation of the radial velocity component with a/ω for a wavy disk.

The impact of external uniform flow on wavy disk is similar to the flat disk case and the disk rotation effects become more lessen as one increase the values of the axial velocity ratio a/ω . This means that when the radial pressure gradient starts to dominate then the surface irregularities do not contribute too much to assist the flow induced by the disk rotation. This fact can also be understood form Fig. 6.3 which depicts that the positive change in surface roughness ratio corresponds to enhance the radial component

of velocity very slightly and do not interrupt the nature of the flow pattern that was exhibited by the smooth disk.

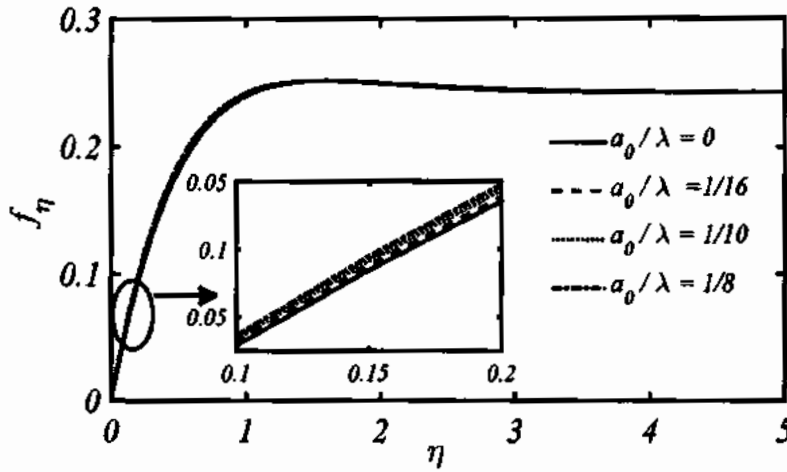


Fig. 6.3: Variation of the radial velocity component with the surface roughness ratio at a fixed $a/\omega = 0.5$.

6.4.2 Circumferential component of velocity

Again the impact of radial pressure gradient on circumferential velocity component remains the same, as shown in Fig. 6.4, in the presence of surface irregularities where the velocity profile shows the typical boundary-layer character. The influence of disk surface texture on this velocity component is also quite weak and increase in surface roughness ratio corresponds to decrease (very slightly) the circumferential component of velocity (refer to Fig. 6.5).

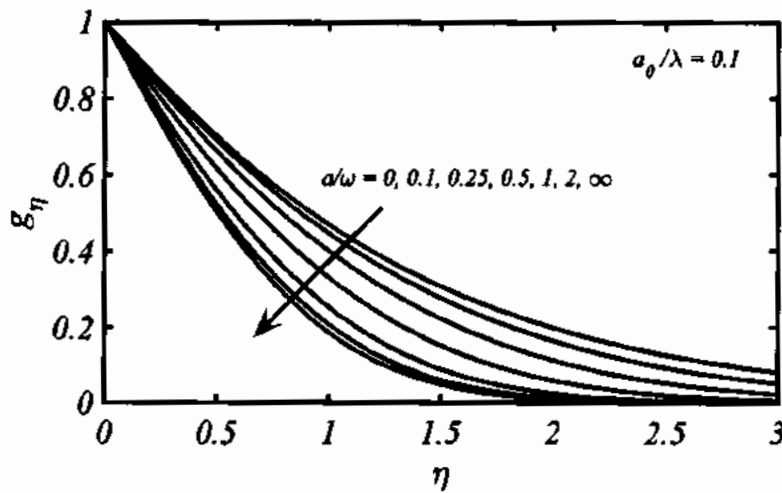


Fig. 6.4: Variation of the circumferential velocity component with a/ω for a wavy disk.

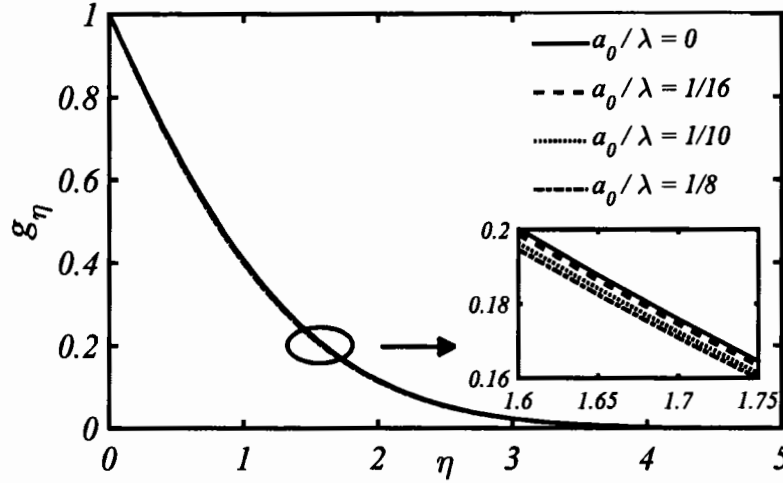


Fig. 6.5: Variation of circumferential velocity component with the surface roughness ratio at a fixed $a/\omega = 0.5$.

6.4.3 Radial and circumferential shearing stresses on wavy disk

The shear stresses acting on the disk surface in the radial and circumferential directions due to the radial and azimuthal flows are, respectively, given by

$$\tau_r = \mu \left. \frac{\partial u_x}{\partial y} \right|_{y=0}, \text{ and } \tau_\theta = \mu \left. \frac{\partial u_\theta}{\partial y} \right|_{y=0}. \quad (6.6)$$

In terms of dimensionless variables, they are transformed to the forms

$$Re_r^{1/2} C_{fr} = 2 \sqrt{\frac{R}{\epsilon}} f_{\eta\eta}(0, \epsilon), \quad Re_r^{1/2} C_{f\theta} = -2 \sqrt{\frac{R}{\epsilon}} g_{\eta\eta}(0, \epsilon), \quad (6.7)$$

where $C_{fr} = \frac{2\tau_r}{\rho r^2 \Lambda^2}$, and $C_{f\theta} = \frac{2\tau_\theta}{\rho r^2 \Lambda^2}$ denote the coefficients of wall skin-friction in the radial and circular directions, and $Re_r = \frac{\Lambda r^2}{\nu}$ represents the local Reynolds number. One can recover the relation for smooth disk from the above ones (Eq. (6.7)) when the surface roughness effects are removed (see Mabuchi et al. [79]). The surface roughness ratio (a_0/λ) strongly effects both the local azimuthal and radial skin-friction coefficients which have been displayed in Figs. 6.6 & 6.7 for a relative motion of fluid and disk ($a/\omega = 0.25$). Due to the disk shape, both are periodic functions with double periodicity in contrast to the surface geometry. This behavior is a consequence of the typical form of the factor $\frac{dR}{d\epsilon}$. It can also be noticed from these Figures that an increase in the amplitude-to-wavelength ratio leads to decrease in both these parameter and interestingly, both shear stresses have maximum value for the case of smooth disk ($a_0/\lambda = 0$) for which the boundary-layer thickness takes the least value. This suggests

that the local shear stresses (of wavy disk) are lesser in magnitude than smooth disk and it is necessary to calculate the overall shear stresses (by calculating average values) on the whole disk surface in order to see the true picture of the shear stresses generated by the simultaneous rotation and motion of fluid flow. The average values of the radial and tangential shear stresses are obtained by integrating Eq. (6.7) over the disk surface as

$$\bar{C}_{f\theta} Re_r^{1/2} = \frac{1}{S} \int_S Re_r^{1/2} C_{f\theta} dS, \quad \bar{C}_{fr} Re_r^{1/2} = \frac{1}{S} \int_S Re_r^{1/2} C_{fr} dS. \quad (6.8)$$

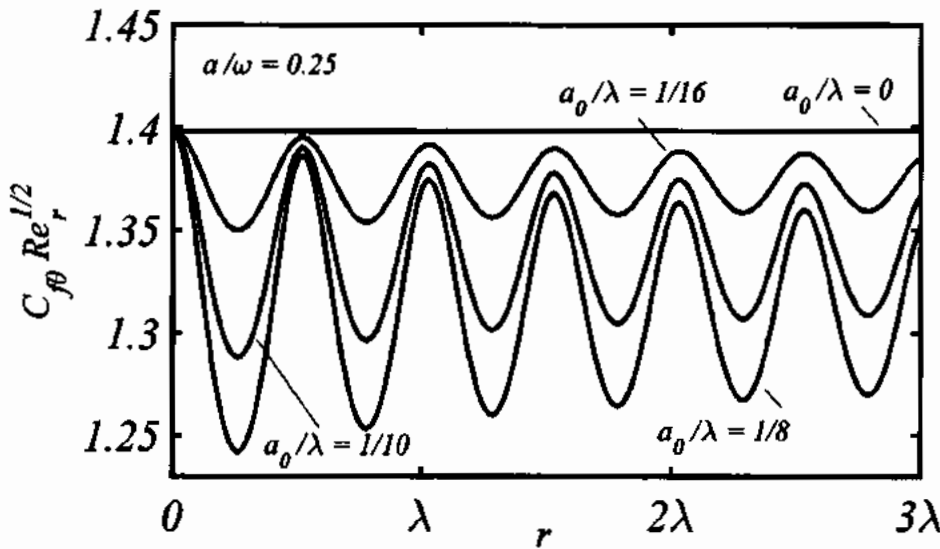


Fig. 6.6: Local azimuthal skin-friction coefficient as a function of amplitude-to-wavelength ratio with relative motion of disk and fluid.

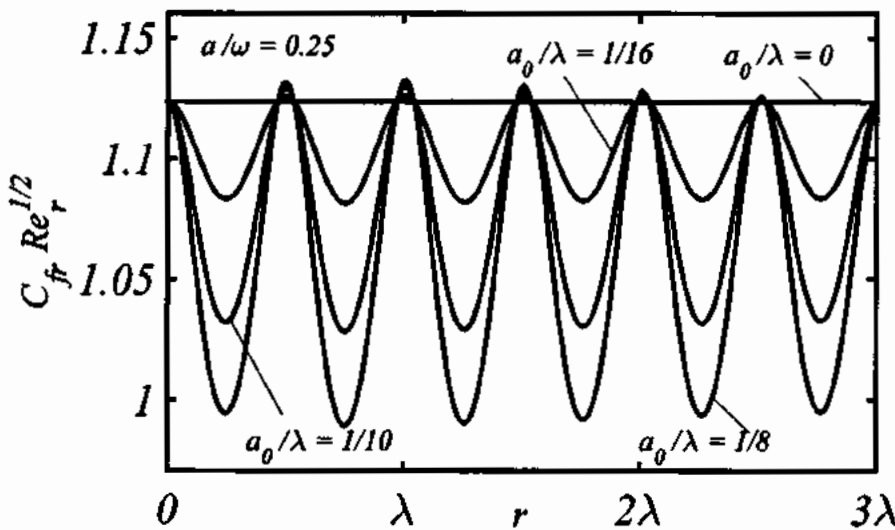


Fig. 6.7: Local radial skin-friction coefficient as a function of amplitude-to-wavelength ratio with relative motion of disk and fluid.

The influence of roughness can be quantified with the help of area of smooth disk (πb^2) taking as a reference. In doing so the corresponding average skin-friction coefficients modify to the form

$$\bar{C}_{f\theta p} = \bar{C}_{f\theta} \frac{S}{\pi b^2}, \quad \bar{C}_{rfp} = \bar{C}_{rf} \frac{S}{\pi b^2}. \quad (6.9)$$

These calculations (Eqs. (6.8) and (6.9)) are demonstrated in Figs. 6.8 & 6.9 from where it can clearly be observed that the $\bar{C}_{f\theta}$ and \bar{C}_{fr} both decrease (curves 1 in Figs. 6.8 & 6.9) as the surface roughness ratio a_0/λ increases. But with the contribution of the actual area of the wavy disk the corresponding average shear stresses given in Eq. (6.9) have higher values in comparison to the smooth disk (refer to curves 2 in Figs. 6.8 & 6.9). Both of these shear stresses ($\bar{C}_{f\theta p}$ & \bar{C}_{frp}) have been enlarged up to 15% for the fixed surface roughness ratio (i.e. $a_0/\lambda = 0.2$) due to the wavy surface in the absence of radial pressure gradients. The influence of a relative motion of the disk and the potential flow on these shear stresses can also be seen from these Figs. 6.8-6.9. It can be seen that these quantities take higher values due to the increasing radial pressure gradient. Interestingly, in the presence of a radial pressure gradient the wavy surface contributes the same (15%) increment in the shear stresses (refer to Table 6.2) as it does in the absence of external flow. In comparison to the free rotating flat disk, the radial and tangential shear stresses of wavy rotating disk in forced flow have been increased up to 174% and 86%, respectively, for $a_0/\lambda = 0.125$ and $\frac{a}{\omega} = \infty$.

Table 6.2: Average azimuthal and radial skin-friction coefficients, moment coefficient, and Nusselt number (CHF) ($Pr = 0.71, N = 3$).

a/ω	a_0/λ	$\bar{C}_{f\theta p}$	\bar{C}_{frp}	\bar{C}_M	$\overline{Nu_p}$
0	0.0	1.2319	1.0204	1.9351	0.3259
	1/16	1.2543	1.0391	1.9703	0.3318
	1/10	1.2865	1.0656	2.0208	0.3402
	1/8	1.3135	1.0878	2.0633	0.3473
0.1	0.0	1.2827	1.0372	2.0149	0.3587
	1/16	1.3061	1.0562	2.0516	0.3652
	1/10	1.3395	1.0832	2.1041	0.3745
	1/8	1.3677	1.1057	2.1483	0.3823
0.25	0.0	1.3983	1.2325	2.1964	0.4103
	1/16	1.4237	1.1441	2.2363	0.4178
	1/10	1.4602	1.1734	2.2937	0.4285
	1/8	1.4910	1.1978	2.3421	0.4374
0.5	0.0	1.6011	1.3711	2.5150	0.4858
	1/16	1.6300	1.3982	2.5604	0.4946
	1/10	1.6719	1.4340	2.6262	0.5072
	1/8	1.7073	1.4641	2.6819	0.5180

1	0.0	1.8675	1.8720	2.9335	0.5764
	1/16	1.9010	1.9060	2.9862	0.5870
	1/10	1.9498	1.9548	3.0628	0.6020
	1/8	1.9914	1.9961	3.1281	0.6148
2	0.0	2.0512	2.3332	3.2220	0.6368
	1/16	2.0877	2.3752	3.2794	0.6484
	1/10	2.1414	2.4361	3.3637	0.6650
	1/8	2.1869	2.4875	3.4352	0.6790
∞	0.0	2.1505	2.6248	3.3780	0.6690
	1/16	2.1886	2.6718	3.4378	0.6812
	1/10	2.2450	2.7404	3.5264	0.6986
	1/8	2.2927	2.7983	3.6013	0.7133

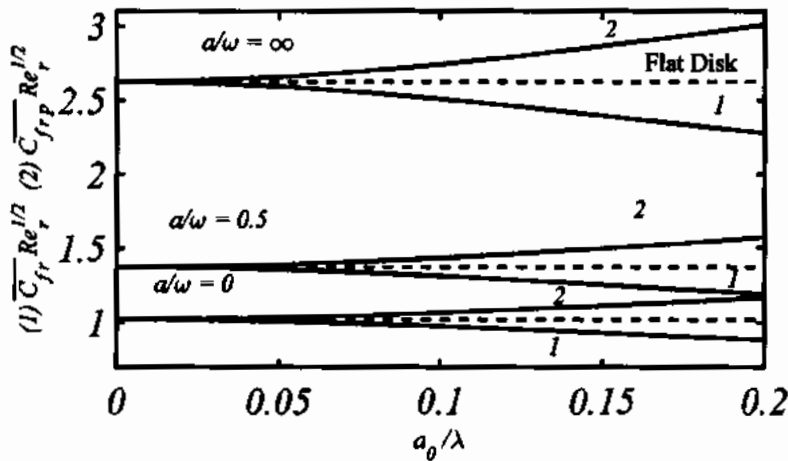


Fig. 6.8: Influence of surface roughness ratio on average radial skin-friction coefficients \bar{C}_{fr} (curve 1) and \bar{C}_{frp} (curve 2).

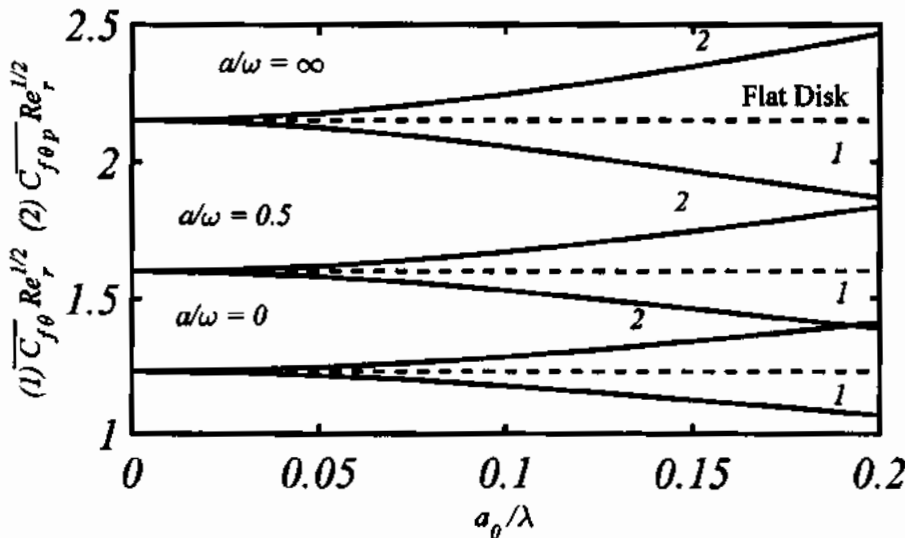


Fig. 6.9: Influence of surface roughness ratio on average azimuthal skin-friction coefficients $\bar{C}_{f\theta}$ (curve 1) and $\bar{C}_{f\theta p}$ (curve 2).

The role of number of sinusoids on the average tangential frictional coefficient ($\bar{C}_{f\theta p}$) is also crucial to be explored. This is presented in Fig. 6.10 where $\bar{C}_{f\theta p}$ is plotted against the number of waves N . The average tangential shear stress increases slowly when N is varied from 1 to 8. For $N > 4$, its value becomes almost constant.

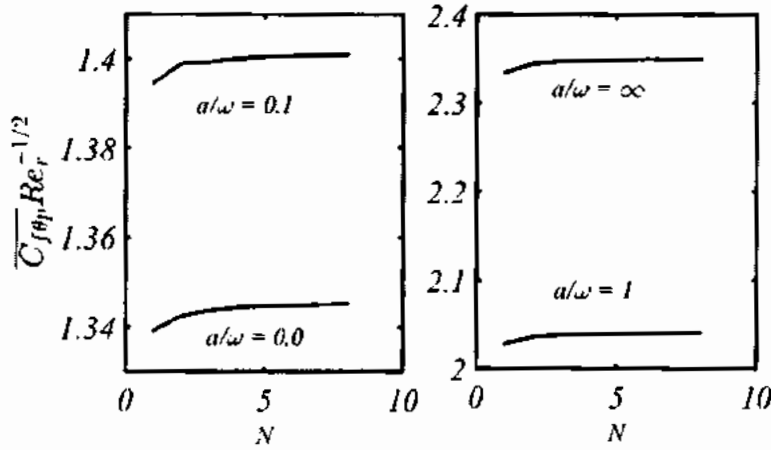


Fig. 6.10: Dependence of average azimuthal skin-friction coefficient on the number of sinusoids.

6.4.4 Heat transfer rate (CHF)

The calculation of influence of sinusoidal-shaped disk on the heat transfer phenomenon is very important. In fact the shape of the disk results in more heat transfer rate as anticipated. The dimensionless local heat transfer rate from the disk surface is computed by the relation

$$Re_{\Lambda}^{-1/2} Nu = \sqrt{\frac{R}{\epsilon}} \frac{1}{\Theta(\epsilon, 0)} \quad (6.10)$$

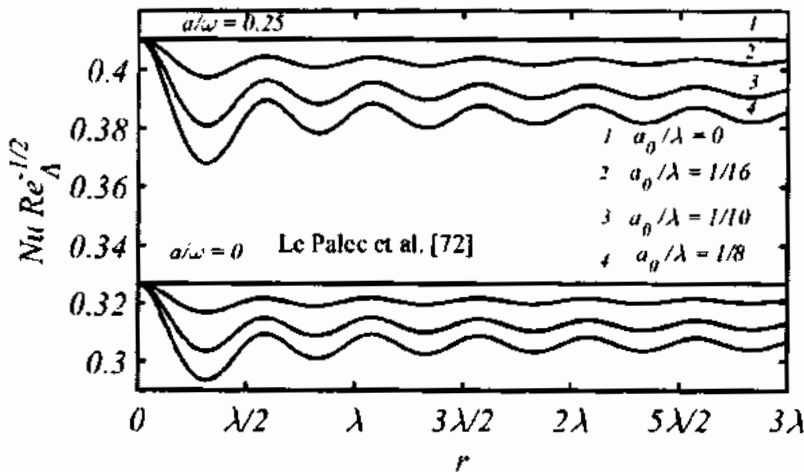


Fig. 6.11: Local Nusselt number as a function of surface roughness ratio with relative motion of disk and fluid for $Pr = 0.71$.

The effect of surface roughness on local heat transfer coefficient is depicted in the Fig. 6.11 which shows the double periodicity in local heat transfer rate with decaying amplitude for the case of $a/\omega = 0$ and $a/\omega = 0.25$; where the absence of radial pressure gradient ($a/\omega = 0$) corresponds to the free rotating wavy disk case investigated by Le Palec et al. [72]. The local heat transfer rate at the wavy disk surface in the forced stream are qualitatively the same as for the free rotating wavy disk situation apart from the fact that the relative motion of the disk and fluid is to strengthen the heat exchange from disk to fluid. Similar to the shear stresses, the local heat transfer rate presented in Fig. 6.11 is lower than the flat disk case and in order to analyze the real heat transfer situation, one must be interested to calculate the overall heat exchange from the wavy disk to the surrounding fluid which can be done by computing the average Nusselt number corrected by the surface area ratio. The average Nusselt number relation can be found in the similar manner as the average skin-friction coefficients were calculated and is given by

$$\overline{Nu} Re_{\Lambda}^{-1/2} = \frac{1}{S} \int_S Re_{\Lambda}^{-1/2} Nu \, dS, \quad (6.11)$$

$$\overline{Nu}_p = \overline{Nu} \frac{S}{\pi b^2}. \quad (6.12)$$

These calculations are demonstrated in Fig. 6.12. From this Figure, it can clearly be observed that the \overline{Nu} decreases (curves 1 of Fig. 6.12) as the ratio a_0/λ increases while the average Nusselt number \overline{Nu}_p (curves 2 of the Fig. 6.12) shows increasing trend in comparison to the smooth disk for increasing values of the surface roughness ratio a_0/λ . In both situations (free rotating disk with and without forced flow), the overall heat transfer rate is 15% higher due to the shape of the disk (for $a_0/\lambda = 0.2$). The influence of waviness on \overline{Nu} & \overline{Nu}_p in the forced flow is again identical to the case when the disk is rotating freely whereas both the Nusselt numbers (\overline{Nu} & \overline{Nu}_p) take larger values in the presence of external forced flow. This means that the relative motion of the disk and fluid corresponds to the cooling of the wavy disk quite significantly. In Table 6.2 the enhancement in the heat transfer rate due to the waviness and the relative motion of the disk and fluid is reported in detail. In the case of $a/\omega = \infty$ and $a_0/\lambda = 0.125$, an enhancement of 119% in comparison to free rotating flat disk has been achieved in heat transfer exchange from the disk to the surrounding fluid.

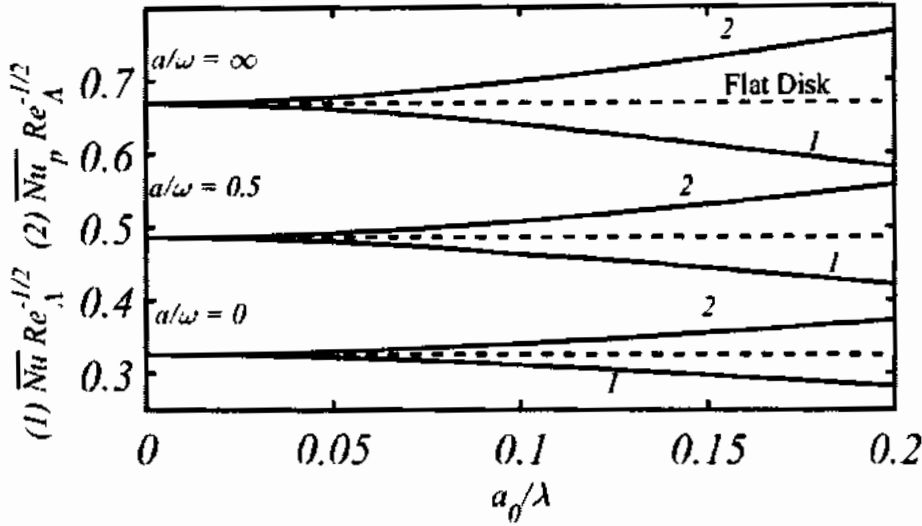


Fig. 6.12: Influence of surface roughness ratio on average Nusselt numbers \overline{Nu} (curve 1) and \overline{Nu}_p (curve 2) for $Pr = 0.71$.

The impact of the number of sinusoids on the average Nusselt number \overline{Nu}_p is displayed in Fig. 6.13 which is the same (in qualitative sense) as it is already observed for the average tangential stress.

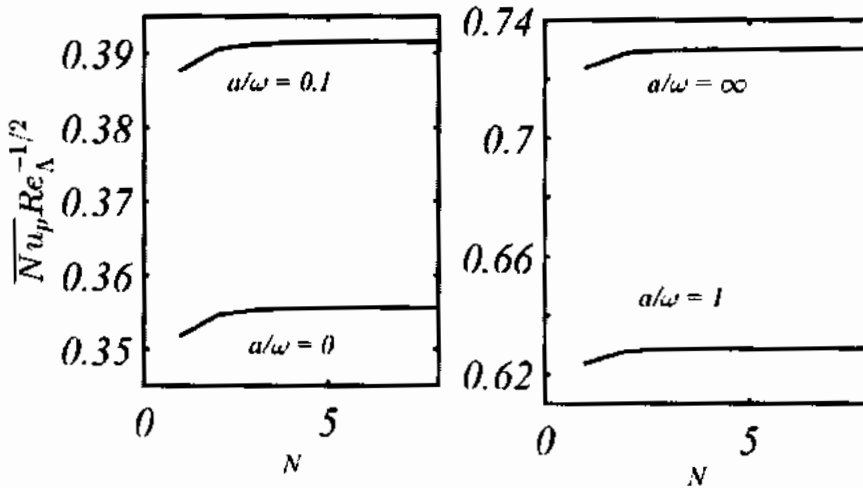


Fig. 6.13: Dependence of heat transfer on number of waves at $Pr = 0.71$.

6.4.5 Heat transfer rate from non-isothermal wavy disk (VWT)

The local heat transfer rate from the non-isothermal wavy disk is measured by the local Nusselt number yielding the following relationship in terms of normalized variables

$$Re_A^{-1/2} Nu = \sqrt{\frac{R}{\epsilon}} \Theta_\eta(\epsilon, 0). \quad (6.13)$$

The spatial variation in the heat transfer rate is illustrated in Fig. 6.14 depicting the wavy nature of the heat transfer rate undergoing two cycles per wavelength (wavelength of $Nu = \lambda/2$) with the decreasing amplitudes (irrespective to the geometrical configuration) for the non-isothermal disk ($n_* \neq 0$) also. Such exhibition of the local Nusselt number had already been reported by Le Palec [71] for the isothermal free rotating disk case ($n_* = 0$). Clearly (see Fig. 6.14) the higher values of temperature distribution exponent ($n_* > 0$) correspond to increase the local heat transfer rate and decreasing values ($n_* < 0$) result in lowering the local heat transfer rate than the isothermal case ($n_* = 0$). A similar trend of the local heat transfer rate is also seen in Fig. 6.15 when the relative velocity ratio takes various values (i.e. $a/\omega \neq 0$). This Figure also illustrates that an increase in the relative velocity ratio leads to increase the associated local heat transfer rate as anticipated for the non-uniform distribution of disk temperature. The zero value of the relative velocity ratio refers to the flow purely induced by the rotation of the sinusoidal disk, whereas its infinite value corresponds to the axis-symmetric stagnation point flow over a resting wavy disk. One thing is most important to note in these Figures (Figs. 6.14 & 6.15) that the surface irregularities of the disk result in the reduction of local heat transfer rate as compared to the smooth disk. This behavior had already been reported for the isothermal sinusoidal-shaped disk rotating freely (i.e. $n_* = 0$ & $a/\omega = 0$) by Le Palec [71].

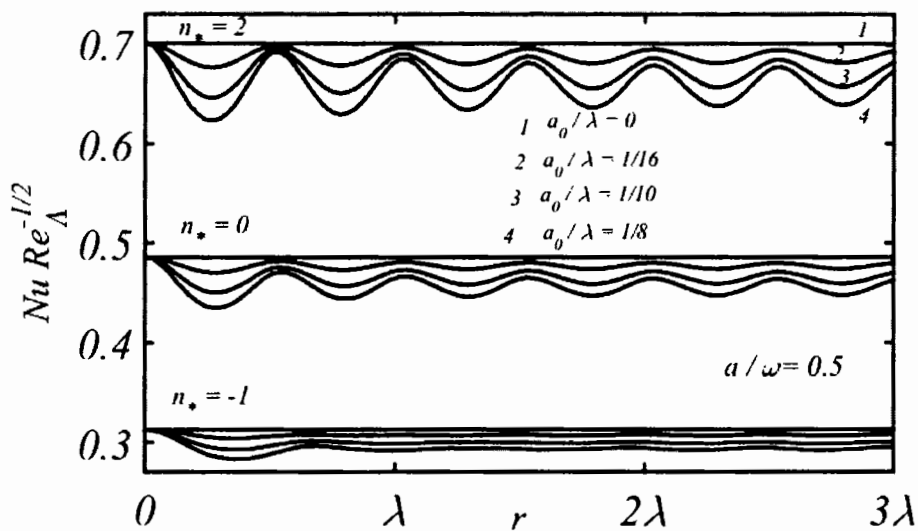


Fig. 6.14: Spatial variation of Nusselt number for different temperature distribution exponents with fixed relative velocity ratio.

The global heat transfer rate from the non-isothermal wavy disk is measured by the mean Nusselt number (\overline{Nu}) which is acquired by the integration of Eq. (6.13) on the whole disk surface and this leads to the following mathematical relation

$$\overline{Nu} Re_\lambda^{-1/2} = \frac{1}{S} \int_S Re_\lambda^{-1/2} Nu \, dS. \quad (6.14)$$

It is also worth mentioning that the flat disk area (πb^2) serves as a reference area which is ultimately utilized to predict the actual global heat transfer rate under the influence of surface irregularities. Such utilization modifies the Eq. (6.14) as

$$\overline{Nu}_p = \overline{Nu} \frac{S}{\pi b^2}. \quad (6.15)$$

These calculations (Eqs. (6.14) & (6.15)) are demonstrated in Fig. 6.16 where the three values of the temperature distribution exponent n_* are considered and a same pattern for the overall heat transfer rate is observed for each considered value of n_* . The curve 1 in Fig. 6.16 shows the calculation of Eq. (6.14) (i.e. without inclusion of wavy surface area) and it clearly decreases with increasing the values of the surface roughness ratio a_0/λ . Whereas the mean Nusselt number obtained from Eq. (6.15) shown in curve 2 in Fig. 6.16 reflects that heat transfer is enhanced with increasing roughness of the disk incongruity to the one which is shown in curve 1. Apart from this it is also noted in Fig. 6.16 that the temperature distribution exponent n_* has also a substantial role on heat transfer enhancement and its higher values yield considerable improvements in the exchange of heat from the hot wavy disk to the cold surrounding fluid. For instance, the considered rough non-isothermal disk rotating in a forced stream of air ($Pr = 0.71$) leads to a significant (about 263%) enhancement in the overall heat transfer rate compared to that of the flat free rotating disk when the wavy disk (with two sinusoids) temperature is quartic function of its radial distance (see Table 6.3(i)). An increment of 3.46 times (for any a_0/λ) in the heat transfer rate is also observed when n_* is varied from -1 to 4 for the situation of flow induced by the pure rotation of the sinusoidal disk. For the relative velocity ratio $a/\omega = 0.5$ & ∞ , a hike of 2.70 & 2.58 (respectively) times in the average heat transfer rate is observed. Obviously, the larger values of the relative velocity ratio correspond to frail the influence of the temperature distribution exponent. Interestingly, the values of temperature exponent n_* has no association with waviness of the surface and perhaps it enhances the heat transfer rate at the same time whether the disk is flat or rough. It is also important to note that the influence of n_* gets also weaken when the nature of fluid (flowing in axial stream) is changed (i.e. with the increase in values of Pr). As an example, refer to Table 6.3 (iii) ($Pr = 10$), where

it can be seen that an increment of 2.64, 2.50 and 2.43 times is achieved when n_* is varied from -1 to 4 for $a/\omega = 0, 0.5, \infty$, respectively for any a_0/λ showing the weak character of n_* as compared to the case $Pr = 0.71$.

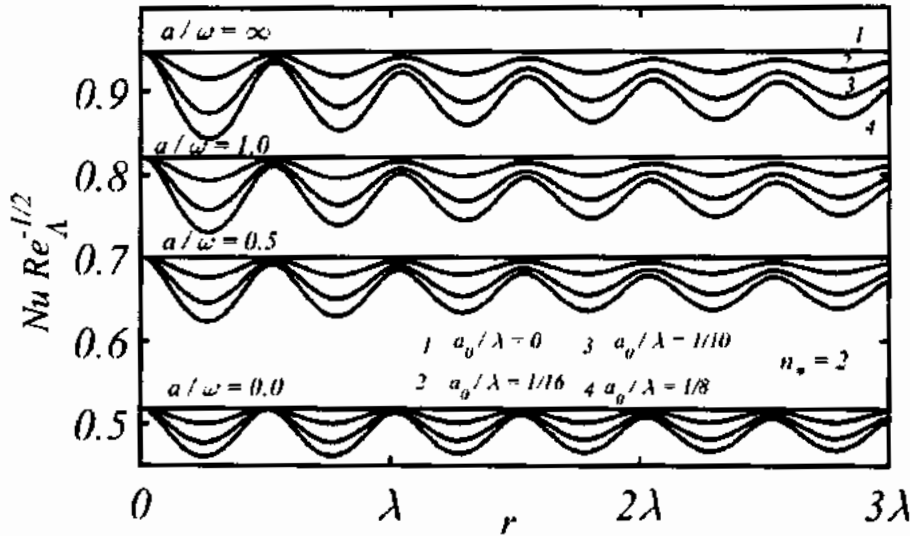


Fig. 6.15: Spatial variation of Nusselt number for different values of relative velocity ratio with fixed temperature distribution exponent.

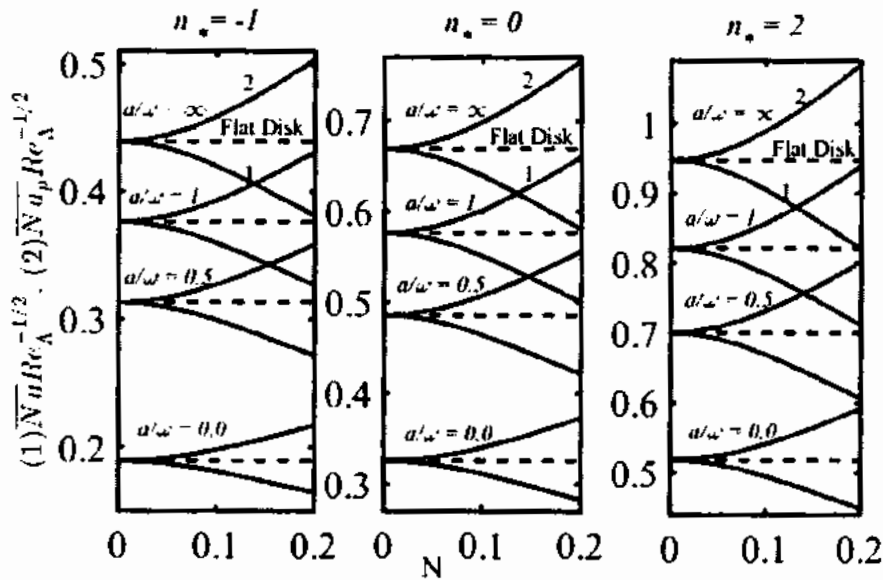


Fig. 6.16: Mean Nusselt number \bar{Nu} (curve 1) and \bar{Nu}_p (curve 2) under the influence of non-uniform temperature distribution and amplitude-to-wavelength ratio.

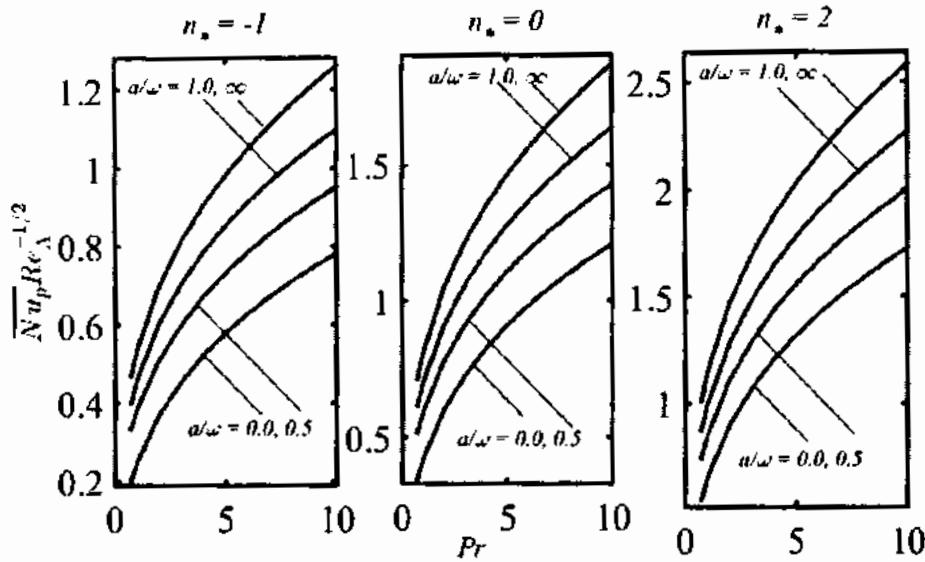


Fig. 6.17: Effect of Prandtl number on mean Nusselt number for various variation in relative velocity ratio at $\alpha_0/\lambda = 0.1$.

The effects of Prandtl number on the mean Nusselt number are also presented in Fig. 6.17 in the presence of surface roughness ($\alpha_0/\lambda = 0.1$) for three values of n_s and for the different relative velocity ratios. Increase in heat transfer rate with the larger values of Pr can clearly be seen from this Figure which is, however, a trivial fact.

Table 6.3 (i) $Pr = 0.71$, (ii) $Pr = 1$ & (iii) $Pr = 10$: Values of mean Nusselt number \overline{Nu}_p for different temperature distribution exponent and relative velocity ratios with two sinusoids.

(i)						
a/ω	α_0/λ	$n_s = -1$	$n_s = 0$	$n_s = 1$	$n_s = 2$	$n_s = 4$
0.0	0.0	0.1893	0.3259	0.4319	0.5185	0.6555
	1/16	0.1928	0.3318	0.4397	0.5279	0.6674
	1/10	0.1979	0.3403	0.4510	0.5413	0.6842
0.5	0.0	0.3132	0.4858	0.6065	0.7006	0.8461
	1/16	0.3190	0.4947	0.6175	0.7133	0.8614
	1/10	0.3272	0.5073	0.6332	0.7315	0.8832
1	0.0	0.3763	0.5765	0.7143	0.8211	0.9851
	1/16	0.3832	0.5870	0.7273	0.8360	1.0028
	1/10	0.3930	0.6019	0.7457	0.8571	1.0281
2	0.0	0.4174	0.6368	0.7872	0.9033	1.0812
	1/16	0.4251	0.6484	0.8014	0.9196	1.1007
	1/10	0.4358	0.6648	0.8217	0.9428	1.1284
∞	0.0	0.4392	0.6690	0.8262	0.9476	1.1332
	1/16	0.4473	0.6812	0.8412	0.9647	1.1536
	1/10	0.4588	0.6987	0.8627	0.9893	1.1829

(ii)

a/ω	a_0/λ	$n_* = -1$	$n_* = 0$	$n_* = 1$	$n_* = 2$	$n_* = 4$
0.0	0.0	0.2352	0.3963	0.5180	0.6159	0.7693
	1/16	0.2395	0.4035	0.5274	0.6271	0.7832
	1/10	0.2457	0.4137	0.5407	0.6428	0.8028
0.5	0.0	0.3615	0.5577	0.6942	0.8004	0.9641
	1/16	0.3681	0.5679	0.7068	0.8149	0.9816
	1/10	0.3776	0.5824	0.7248	0.8356	1.0064
1	0.0	0.4320	0.6583	0.8135	0.9334	1.1173
	1/16	0.4399	0.6703	0.8282	0.9503	1.1375
	1/10	0.4512	0.6874	0.8493	0.9744	1.1662
2	0.0	0.4784	0.7260	0.8949	1.0251	1.2244
	1/16	0.4871	0.7392	0.9111	1.0436	1.2465
	1/10	0.4997	0.7581	0.9343	1.0701	1.2780
∞	0.0	0.5031	0.7622	0.9387	1.0747	1.2826
	1/16	0.5123	0.7761	0.9557	1.0941	1.3057
	1/10	0.5254	0.7960	0.9802	1.1220	1.3388

(iii)

a/ω	a_0/λ	$n_* = -1$	$n_* = 0$	$n_* = 1$	$n_* = 2$	$n_* = 4$
0.0	0.0	0.7368	1.1341	1.4083	1.6205	1.9460
	1/16	0.7502	1.1548	1.4339	1.6499	1.9812
	1/10	0.7667	1.1825	1.4962	1.6909	2.0308
0.5	0.0	0.8932	1.3411	1.6445	1.8781	2.2356
	1/16	0.9094	1.3655	1.6743	1.9121	2.2759
	1/10	0.9320	1.4001	1.7169	1.9606	2.3335
1	0.0	1.0315	1.5355	1.8744	2.1346	2.5319
	1/16	1.0501	1.5634	1.9084	2.1731	2.5775
	1/10	1.0779	1.6041	1.9577	2.2289	2.6432
2	0.0	1.1293	1.6754	2.0417	2.3223	2.7507
	1/16	1.1496	1.7059	2.0786	2.3643	2.8003
	1/10	1.1803	1.7503	2.1322	2.4248	2.8715
∞	0.0	1.1825	1.7522	2.1337	2.4260	2.8720
	1/16	1.2038	1.7840	2.1724	2.4698	2.9237
	1/10	1.2346	1.8295	2.2277	2.5326	2.9977

The average heat transfer is also found to depend upon the number of sinusoids fitted to the disk radius of $0 \leq r \leq b$ in Fig. 6.18. It is observed that whatever the flow situation is for any a/ω or whether the disk is isothermal or non-isothermal (for any n_*) the mean Nusselt number increases slowly with the increase in the number of cycles N up to $N = 4$. After that it becomes almost constant.

According to Shevchuk [37], the heat transfer rate from the free rotating flat disk seizes at the value $n_* = -2$. This value does also remain invariant for the flat rotating disk in the presence of radial pressure gradient or with the alteration of Prandtl number. But interestingly, this threshold value is found to depend upon the waviness

of the surface; the radial pressure gradient, and as well as the Prandtl number which play their role when the disk texture is changed from smooth to non-smooth. The threshold values of temperature distribution exponent vary as: $n_* = -1.996$ ($Pr = 0.71$), -1.995 ($Pr = 1.0$) & -1.990 ($Pr = 10$) for fixed $a_0/\lambda = 0.1$ & $a/\omega = 0$ (see Table 6.4 (i) – (iii)). This indicates that the variations in the threshold values are not too huge and a slightly decreasing trend is observed for increasing Prandtl numbers. These variations become more less when surface roughness ratio is kept smaller than 0.1. Furthermore, the relative motion of wavy disk and the forced flow also have their role in altering this value ($n_* = -2$). In Table 6.4 (i) one can notice that this value ($n_* = -2.0001$) is further close to the flat disk value ($n_* = -2$) for the wavy disk ($a_0/\lambda = 0.1$) in the presence of an axial stream ($a/\omega = 1, 2$ & ∞). The relative motion of the disk and fluid, for the case $Pr = 10$, causes to change this threshold value further away from the flat disk (see Table 6.4 (iii)). This means that the surface roughness have strong impact on the threshold values for which heat transfer is seized.

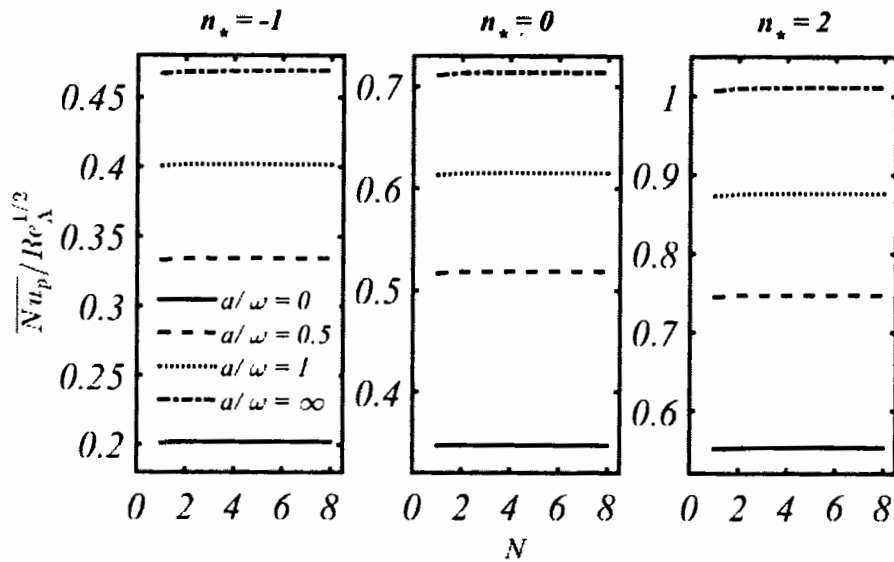


Fig. 6.18: Heat transfer rate influenced by number of sinusoids at $Pr = 0.71$.

Table 6.4: (i) $Pr = 0.71$, (ii) $Pr = 1$ & (iii) $Pr = 10$: Values of temperature distribution exponent for which heat transfer from the wavy disk is seized.

(i)

a_0/λ	a/ω				
	0	0.5	1	2	∞
0.0	-2	-2	-2	-2	-2
1/16	-2	-2	-2.0001	-2.0001	-2.0001
1/10	-1.9996	-2.0001	-2.0004	-2.0004	-2.0004

(ii)

a_0/λ	a/ω				
	0	0.5	1	2	∞
0.0	-2	-2	-2	-2	-2
1/16	-2	-2	-2	-2	-2
1/10	-1.9995	-1.99997	-2	-2	-2

(iii)

a_0/λ	a/ω				
	0	0.5	1	2	∞
0.0	-2	-2	-2	-2	-2
1/16	-1.9998	-1.9996	-1.9996	-1.9996	-1.9996
1/10	-1.9990	-1.9990	-1.9989	-1.9989	-1.9989

CHAPTER 7

Conclusions

In this dissertation, special attention is given to enhance the heat/mass transfer in three-dimensional complex flows which arise in rotating disk systems. In this regard, significant enhancement in heat/mass transfer is achieved by considering non-uniform distribution of nanoparticle in the fluid flowing over a rotating disk. This strategy has been considered in **Chapter 2**. The influence of non-homogeneous distribution of nanoparticle on working fluid is observed as many-fold; it enhances the heat transfer rate, and also increases the disk power. The nanofluid flow and the associated heat transfer rate depend upon the nanoparticle concentration and the Schmidt number. The analysis of Chapter 2 reveals that the concentration profile within the boundary-layer is strongly effected by the variation in Schmidt number but the same variation of Schmidt number on velocity and temperature profile is not that significant. The concentration boundary-layer becomes almost 10% of the momentum boundary-layer at higher Schmidt numbers. However, the variations in nanoparticle concentration parameter (ϕ_∞) contribute by different means i.e. the velocity profiles are increased at higher concentration levels. The mass flow rate and the moment coefficient are also enlarged with increasing ϕ_∞ which means that the pumping capability of the rotating disk is enhanced when the working fluid is a nanofluid. The pressure raises (in magnitude) with increasing nanoparticle concentration whereas it falls at higher Schmidt numbers. The displacement thickness is also observed to be increased at higher concentration levels.

Additionally, the heat transfer enhancement is observed by changing the values of Prandtl number at a fixed concentration level but more heat transfer augmentation has been attained by varying the nanoparticle concentration parameter ϕ_∞ and fixing the Prandtl number. An enhancement of 68% in heat transfer rate is observed for water at 20% concentration level of nanoparticle. The comparison between the non-homogeneous and the homogeneous models reflects that the heat transfer enhancement is higher for non-homogeneous model. From this one can realize that the non-homogeneous model is more advantageous while analyzing the convective heat transfer of nanofluid. For instance, a significant intensification (of almost 30%) in heat transfer

rate is obtained through the non-homogeneous modeling for a mixture of 20% nanoparticles and water in comparison to the homogeneous modeling. This fact emphasizes the character of non-uniform distribution of nanoparticle within the rotating disk boundary-layer.

A new class of wall temperature distribution on the rotating disk boundary-layer has been analyzed in **Chapter 3** for which no self-similar solution exists. The problem is modelled with the boundary-layer equations which are then solved numerically with the aid of Keller-box scheme. A detailed and careful analysis has been made for different cases of wall temperature following the sinusoidal, exponentially increasing or decreasing, and non-linearly increasing or decreasing forms. The manipulations revealed that significant heat transfer enhancement is achieved for the exponentially increasing and non-linearly increasing distribution of disk temperature. Furthermore, enhancement in heat transfer is directly linked to the exponent as well as Prandtl number while a reversed trend is observed for the remaining cases and some values of exponents are reported for which disk surface becomes insulator at specific radial locations.

The self-similar transport equations were used to simulate the flow and heat transfer in a conical gap between a porous disk and cone (which touches the disk by its apex) in **Chapter 4**. Different situations were considered for the flow analysis which comprise of cone rotation with fixed disk, and vice versa, simultaneous and counter rotation of the disk and cone. The disk surface temperature has been assumed to follow the power-law radial distribution whereas the cone surface was considered as isothermal. The mass transfer (addition or removal) has a strong impact on different flow regimes along with heat transfer. Mass withdrawal (suction), as usual, stabilizes the flow in all cases but surprisingly, in the current analysis, a sufficient amount of suction completely changes the nature of flow within the gap or near the disk or cone. For instance, Table 4.4 gives the information regarding the case of counter-rotating disk and cone. It can easily be noticed that with the supply of sufficient amount of suction the centrifugal flow is converted into centripetal flow. In fact, fully 100% centripetal flow is observed at $H_w = -1.91$ whereas for impermeable disk case it was 40% and remaining 60% was centrifugal flow within the gap which is greatly influenced by mass addition or removal. Moreover, heat transfer enhancement has been achieved through mass removal from the disk surface for $n_* \leq 0$. But for $n_* > 0$, even suction was unable to enhance the heat transfer and rate of heat transfer decreases considerably with mass removal. Mass

addition (fluid injection) was responsible for the heat transfer enhancement for this case ($n_* > 0$) which clearly shows the reversed influence of fluid injection. This opposite outcome can also be observed on flow regimes with all considered cases of disk and cone rotation. Apart from this, current investigation also contains some threshold values of mass transfer parameter in the large conical gap case which are responsible for zero heat transfer rate for the prescribed values of n_* . For $n_* = 2$, heat transfer was diminished due to the suction whereas for $n_* = -1$ fluid injection was responsible for zero heat transfer rate. Neither the suction nor injection were able to diminish the heat transfer for the isothermal or linearly increasing temperature distribution cases. Diminishing of heat transfer is also absent when the gap is small for all the considered values of n_* .

From the engineering point of view and practicality of the problem some conclusions were drawn that the efficiency of cone-and-disk arrangement used in cooling processes can be higher for a rotating porous disk (with mass removal) distributed with radially decreasing temperature and stationary cone. But when the disk is isothermal then one can obtain higher heat transfer rate (with suction) in the case with simultaneous rotation of disk and cone with almost identical velocities. In the case of quadratic distribution of disk temperature one can acquire increased heat transfer rate (with fluid injection) in the situation when disk is fixed and cone is rotating.

Heat and mass transfer over a rotating rough non-isothermal disk has been investigated in **Chapter 5** for a very large range of Prandtl (Schmidt) number. The roughness of the disk is modelled by periodic sinusoids with a surface roughness ratio $a_0/\lambda \leq 0.2$. Numerical solution of the governing non-similar equations are obtained with the aid of Keller-box method and attained results show that the presence of surface irregularities account towards the significant enhancement in heat transfer rate. For instance, 110% enhancement in overall heat transfer rate is observed for a surface roughness ratio equals to 0.1 by keeping $Pr = 0.71$ & $n_* = 4.0$ in comparison to the isothermal flat disk case. Furthermore, for the whole considered range of Prandtl (Schmidt) number and temperature distribution exponent, the non-flatness of the disk (for surface roughness ratio = 0.1) contributes almost 1.04 times in the augmentation of global heat transfer rates. Apart from this a similar trend (like smooth disk) in a wavy disk was also noticed when the temperature/mass distribution exponent n_* was increased i.e. it results in thinning the thermal boundary-layer thickness which in turn

increases the heat transfer rate. An identical influence of the number of sinusoids on heat transfer coefficient was observed in the case of non-isothermal sinusoidal disk like the work reported by Le Palec [71]. An interesting observation related to the threshold value ($n_{threshold} = -2$ for a flat disk) for which heat transfer is seized from the disk surface, has been made for the wavy disk which highlights the role of surface roughness on non-isothermal disk. The threshold value which is independent of the Prandtl number in the case of flat disk is found to depend on Prandtl number. Surprisingly this seizing (threshold) value is found to vary slightly in the considered flow due to the wavy nature of the disk surface.

A numerical study is performed in **Chapter 6** for the flow and heat transfer subject to uniform heat flux and for a rotating wavy disk in the presence of a uniform forced stream. The numerical solution has been validated for a flat rotating disk case in the presence of an external forced flow with the results reported in [79] and in excellent agreement has been found. Moreover, the authenticity of our solution is also confirmed with the theoretical and experimental work of Le Palec et al. [72] (i.e. the heat transfer and flow is induced only due to the rotation of sinusoidal-shaped disk) and the present results are in good accordance with those reported by Le Palec et al. [72]. The analysis presented in **Chapter 6** reveals that all the physical parameters of interest like the radial and tangential wall shear stresses, moment coefficient, and heat transfer rate (Nusselt number) exhibit double periodicity in both situations (rotating disk with and without forced stream) in comparison to the geometrical configuration. Due to the surface roughness almost 15% enhancement in the values of the average radial, azimuthal skin-friction coefficients and the average Nusselt number is observed for both conditions (rotating disk with and without external flow field) at $a_0/\lambda = 0.2$. The moment coefficient is also increased due to the sinusoidal-shaped disk which in turn shows that the power of such a disk is increased in comparison to the smooth disk. Furthermore, 119%, 174%, 86%, and 86% enhancement in the heat transfer rate, the radial shear stress, the tangential shear stress, and the moment coefficient, respectively, is observed for the wavy disk rotating in forced flow at a fixed $a/\omega = \infty$ and $a_0/\lambda = 0.125$ in comparison to the free rotating flat disk. This fact highlights the beneficial role of disk with sinusoidal waves under the action of a uniform external forced stream.

Heat transfer over a non-isothermal sinusoidal disk rotating inside a uniform stream has also been examined numerically in **Chapter 6**. The numerical results reveal that

the power-law exponent of the non-isothermal distribution of temperature has the key role in enhancing the heat transfer rate in the presence of surface roughness. The role of temperature exponent becomes weakened with the increase in Prandtl number, similar to the flat disk case. The double periodicity has also been exhibited by the local heat transfer rate with non-isothermal disk situation in the presence or absence of the radial pressure gradient. The local Nusselt number has been found to decrease from the flat disk value for all considered values of temperature distribution exponent. This decrease is more pronounced when the amplitude – to – wavelength ratio is increased. For this purpose a mean Nusselt number is calculated which reveals the clear picture of heat transfer from the corrugated disk. In fact, the mean Nusselt number increases showing heat transfer enhancement due to surface roughness. Such enhancement in the heat transfer rate is observed to be a strong function of the amplitude – to – wavelength ratio; the relative velocity ratio, and the temperature exponent. It is worth mentioning here that some threshold values of temperature exponent were also identified for which the disk surface behaves like a layer of isotherm and heat transfer is seized from the disk surface. These values were found to depend only on the wavy character of the disk. Furthermore, a very small variation in the threshold values was observed and these values are just slightly different from those of the smooth disk case.

REFERENCES

- [1] L. Prandtl, "Über Flüssigkeits bewegung bei sehr kleiner Reibung," in *Proc. 3rd Int. Math. Cong.*, Heidelberg, 1904.
- [2] H. Blasius, "Grenzschichten in Flüssigkeiten mit kleiner Reibung," *Z. Math. u. Phys.*, vol. 56, pp. 1-37, 1908.
- [3] R. J. Lingwood, "Absolute instability of the boundary layer on a rotating disk," *Journal of Fluid Mechanics*, vol. 299, pp. 17-35, 1995.
- [4] B. Pier, "Finite-amplitude crossflow vortices, secondary instability and transition in the rotating-disk boundary layer," *Journal of Fluid Mechanics*, vol. 487, pp. 315-343, 2003.
- [5] P. W. Carpenter and P. J. Thomas, "Flow over a compliant rotating disks," *Journal of Engineering Mathematics*, vol. 57, pp. 303-315, 2007.
- [6] C. Davies and P. W. Carpenter, "Global behaviour corresponding to the absolute instability of the rotating-disk boundary layer," *Journal of Fluid Mechanics*, vol. 486, pp. 287-329, 2003.
- [7] S. Imayama, *Experimental study of the rotating-disk boundary layer flow. Ph. D. thesis, Linne FLOW Centre, Sweden: Royal Institute of Technology SE-100 44 Stockholm*, 2014.
- [8] T. V. Kármán, "Über laminaire und turbulente reibung," *Journal of Applied Mathematics and Mechanics*, vol. 1, pp. 233-252, 1921.
- [9] W. G. Cochran, "The flow due to a rotating disk," *Mathematical proceedings of the Cambridge Philosophical Society*, vol. 30, pp. 365-375, 1934.
- [10] S. Goldstein, "On the resistance to the rotation of a disc immersed in a fluid," *Proceedings of the Cambridge Philosophical Society*, vol. 31, pp. 232-241, 1935.
- [11] N. Gregory, T. J. Stuart and S. W. Walker, "On the stability of threedimensional boundary layers with application to the flow due to a rotating disk," *Proceedings of the Royal Society of London. Series A, Mathematical and Physical Sciences*, vol. 248, pp. 155-199, 1955.
- [12] H. Schlichting and E. Truckenbrod, "The flow around a rotating disc in a uniform stream," *Journal of the Aeronautical Sciences*, vol. 18, no. 9, pp. 639-640, 1951.
- [13] A. N. Tifford, "On the flow around a rotating disc in a uniform stream," *Journal of the Aeronautical Sciences*, vol. 19, no. 4, pp. 284-285, 1952.

- [14] J. T. Stuart, "On the effects of uniform suction on the steady flow due to a rotating disk," *The Quarterly Journal of Mechanics and Applied Mathematics*, vol. 7, pp. 446-457, 1954.
- [15] K. G. Mithal, "On the effects of uniform high suction on the steady flow of a non-Newtonian liquid due to a rotating disk," *The Quarterly Journal of Mechanics and Applied Mathematics*, vol. 14, pp. 403-410, 1961.
- [16] S. N. Lance and M. H. Rogers, "Axially symmetric flow of a viscous fluid between two infinite rotating disk," *proceedings of the royal society of london a mathematical physical and engineering sciences*, vol. 266, no. 1324, pp. 109-121, 1961.
- [17] E. R. Benton, "On the flow due to a rotating disk," *Journal of Fluid Mechanics*, vol. 24, pp. 781-800, 1966.
- [18] G. L. Mellor, P. J. Chapple and V. K. Stokes, "On the flow between a rotating and a stationary disk," *Journal of Fluid Mechanics*, vol. 31, no. 1, pp. 95-112, 1968.
- [19] G. S. Gram and M. Anwar, "Steady flow of a micropolar fluid due to rotating disc," *Journal of Engineering Mathematics*, vol. 13, no. 3, pp. 223-234, 1979.
- [20] C. Y. Wang and L. T. Watson, "Viscous flow between rotating discs with injection in porous disk," *Zeitschrift für angewandte Mathematik und Physik*, vol. 30, pp. 773-787, 1979.
- [21] A. Solan, S. Olek and M. Toren, "Rotating compressible flow over an infinite rotating disk," *Journal of Applied Mechanics*, vol. 50, pp. 511-516, 1983.
- [22] H. A. Attia, "Unsteady MHD flow near a rotating porous disk with uniform suction or injection," *Journal of Fluid Dynamics Research*, vol. 23, pp. 283-290, (1998).
- [23] H. A. Attia and L. A. Aboul-Hassan, "On hydromagnetic flow due to a rotating disk," *Applied Mathematical Modelling*, vol. 28, pp. 1007-1014, 2004.
- [24] M. Miklavcic and C. Y. Wang, "The flow due to a rough rotating disk.," *Journal of Applied Mathematics and Mechanics*, vol. 54, pp. 1-12, 2004.
- [25] A. Mehmood, A. Ali, H. S. Takhar, O. Anwar Beg, M. N. Islam and L. S. Vilson, "Unsteady von Karman swirling flow: Analytic study using the homotopy method," *International Journal of Applied Mathematics and Mechanics*, vol. 6, no. 2, pp. 67-84, 2010.
- [26] K. Millsaps and K. Pohlhausen, "Heat transfer by laminar flow from a rotating plate," *Journal of Aeronautical Science*, vol. 19, pp. 120-126, 1952.

- [27] E. Sparrow and J. Gregg, "Heat transfer from a rotating disk to fluids at any Prandtl number," *Journal of Heat Transfer*, vol. 81, pp. 672-673, 1959.
- [28] J. Hartnett, "Heat transfer from non-isothermal disk rotating in still air," *Journal of Applied Mechanics*, vol. 81, pp. 672-673, 1959.
- [29] J. Hartnett and E. Deland, "The influence of Prandtl number on the heat transfer from rotating non-isothermal disks and cones," *Journal of Heat Transfer*, vol. 83, pp. 95-96, 1961.
- [30] L. C. Tien and J. Tsuji, "Heat transfer by laminar forced flow against a non-isothermal rotating disk," *International Journal of Heat and Mass Transfer*, vol. 7, pp. 247-252, 1963.
- [31] V. G. Levich, *Physico-Chemical Hydro-dynamics*, Englewood Cliffs: Prentice-Hall, 1962.
- [32] B. T. Ellison and I. Cornet, "Mass transfer to a rotating disk," *Journal of the Electrochemical Society*, vol. 118, no. 1, pp. 68-72, 1971.
- [33] S. A. Beg, "Forced convective mass transfer from circular disks," *Wärme-und Stoffübertragung*, vol. 1, pp. 45-51, 1973.
- [34] R. Grief and J. A. Paterson, "Mass transfer to a rotating disk in a Newtonian fluid," *Physics of Fluids*, vol. 16, pp. 1816-1817, 1973.
- [35] S. S. Yoon and W. J. Yang, "Numerical study on heat transfer in laminar flow through co-rotating parallel disks," *International Journal of Heat and Mass Transfer*, vol. 27, no. 11, pp. 1963-1970, 1984.
- [36] G. Evans and R. Grief, "A numerical model of the flow and heat transfer in a rotating disk chemical vapor deposition reactor," *Journal of Heat Transfer*, vol. 109, pp. 928-935, 1987.
- [37] I. V. Shevchuk, *Convective heat and mass transfer in rotating disk systems*, Verlag Berlin Heidelberg: Springer Science & Business Media, 2009.
- [38] J. C. Maxwell, *Treatise on Electricity and Magnetism*, London: Oxford University Press, 1904.
- [39] P. Koblinski, S. R. Philpot, S. U. S. Choi and J. A. Eastman, "Mechanisms of heat flow in suspensions of nano-sized particles (nanofluids)," *International Journal of Heat and Mass Transfer*, vol. 45, pp. 855-863, 2002.
- [40] S. U. S. Choi, "Enhancing thermal conductivity of fluids with nanoparticle in developments and applications of Non-Newtonian flows," *Fluids Engineering Division*, vol. 231, pp. 99-103, 1995.

- [41] J. Buongiorno, "Convective transport in nanofluids," *Journal of Heat Transfer*, vol. 128, pp. 240-250, 2006.
- [42] R. K. Tiwari and M. K. Das, "Heat transfer augmentation in a two-sided lid-driven differentially heated square cavity utilizing nanofluids," *International Journal of Heat and Mass Transfer*, vol. 50, pp. 2002-2018, 2007.
- [43] M. H. Buschmann, "Nanofluid in thermosyphons and heat pipes: overview of recent experiments and modelling approaches," *International Journal of Heat and Mass Transfer*, vol. 52, pp. 3187-3196, 2009.
- [44] U. Rea, T. Meckrell, L. Hu and J. Buongiorno, "Laminar convective heat transfer and viscous pressure loss of alumina-water and zirconia-water nanofluids," *International Journal of Heat and Mass Transfer*, vol. 52, pp. 2042-2048, 2009.
- [45] S. E. B. Magia, C. T. Nguyen, N. Glains and G. Roy, "Heat transfer behaviors of nanofluids in uniformly heated tube," *Superlattices Microstructure*, vol. 35, pp. 543-557, 2004.
- [46] D. Merhi, E. Lemaire, G. Bossis and F. Moukalled, "Particle migration in concentrated suspensions flowing between rotating plates: investigations of diffusion flux coefficients," *Journal of Rheology*, vol. 49, pp. 1429-1448, 2005.
- [47] A. A. Avramenko, D. G. Bilnov and I. V. Shevchuk, "Self-similar analysis of fluid flow and heat-mass transfer of nanofluids in boundary layer," *Physics of Fluids*, vol. 23, pp. 1-8, 2011.
- [48] A. A. Avramenko, D. G. Bilnov, I. V. Shevchuk and A. V. Kuznetsov, "Symmetry analysis and self-similar forms of fluid flow and heat-mass transfer in turbulent boundary layer flow of a nanofluid," *Physics of Fluids*, vol. 24, pp. 1-20, 2012.
- [49] M. Frank, D. Anderson, E. R. Weeks and J. F. Morris, "Particle migration in pressure driven flow of a Brownian suspension," *Journal of Fluid Mechanics*, vol. 493, pp. 363-378, 2003.
- [50] Y. L. Ding and D. Wen, "Particle migration in a flow of nanoparticles suspensions," *Powder Technology*, vol. 149, pp. 84-92, 2005.
- [51] A. Mehmood and M. Usman, "Non-uniform nanoparticle concentration effects on moving plate boundary layer," *Canadian Journal of Physics*, vol. 94, no. 11, pp. 1222-1227, 2016.
- [52] A. Mehmood and M. Usman, "Delaying boundary layer separation in a retarded potential flow," *International Journal of Applied and Computational Mathematics*, vol. 3, pp. 1565-1576, 2017.

- [53] A. A. Avramenko, I. V. Shevchuk, A. L. Tyrinov and D. G. Bilnov, "Heat transfer at film condensation of stationary vapor with nanoparticles near a vertical plate," *Applied Thermal Engineering*, vol. 73, no. 1, pp. 389-396, 2014.
- [54] A. A. Avramenko, I. V. Shevchuk, A. L. Tyrinov and D. G. Bilnov, "Heat transfer at film condensation of moving vapor with nanoparticles near a flat surface," *International Journal of Heat and Mass Transfer*, vol. 82, pp. 316-324, 2015.
- [55] A. A. Avramenko, I. V. Shevchuk, A. L. Tyrinov and D. G. Bilnov, "Heat transfer in stable film boiling of nanofluid over a vertical surface," *International Journal of Heat and Mass Transfer*, vol. 92, pp. 106-118, 2015.
- [56] N. Bachok, A. Ishak and I. Pop, "Flow and heat transfer over a rotating porous disk in nanofluid," *Physica B*, vol. 406, pp. 1767-1772, 2011.
- [57] M. Turkyilmazoglu, "Nanofluid flow and heat transfer due to a rotating disk," *Computers & Fluids*, vol. 94, pp. 139-146, 2014.
- [58] M. M. Rashidi, S. Abelman and N. Freidooni, "Entropy generation in steady MHD flow due to a rotating porous disk in a nanofluid," *International Journal of Heat and Mass Transfer*, vol. 62, pp. 515-525, 2013.
- [59] C. Yin, L. Zheng, C. Zhang and X. Zhang, "Flow and heat transfer of nanofluids over a rotating porous disk with velocity slip and temperature jump," *Zeitschrift für Naturforschung*, vol. 70, pp. 351-358, 2015.
- [60] I. C. Liu, H. H. Wan and C. N. Liu, "Flow and heat transfer of nanofluids near a rotating disk," *Advanced Martial Research*, vol. 664, pp. 859-865, 2013.
- [61] T. Kao, A. Domoto and G. Elrod, "Free convection along a nonisothermal vertical flat plate," *Journal of Heat Transfer*, vol. 99, pp. 72-78, 1977.
- [62] T. Na, "Numerical solution of natural convection flow past a non-isothermal vertical plate," *Applied Scientific Research*, vol. 33, pp. 519-543, 1978.
- [63] M. Mooney and R. Ewart, "The conicylindrical viscometer," *Journal of Applied Physics*, vol. 5, pp. 350-354, 1934.
- [64] H. Sdougos, S. Bussolari and C. Dewey, "Secondary flow and turbulence in a cone-and -plate device," *Journal of Fluid Mechanics*, vol. 138, pp. 379-404, 1984.
- [65] M. Fewell and J. Hellums, "The secondary flow of Newtonian fluids in cone-and-plate viscometers," *Transaction of the Society of Rheology*, vol. 21, pp. 535-565, 1977.

- [66] M. Bucschmann, P. Dieterich, N. Adams and H. Schnittler, "Analysis of flow in a cone-plate apparatus with respect to spatial and temporal effects on endothelial cells," *Biotechnology and Bioengineering*, vol. 89, no. 5, pp. 493-502, 2005.
- [67] I. Pelech and A. Shapiro, "Flexible disk rotating on a gas film next to a wall," *Journal of Applied Mechanics*, vol. 31, pp. 577-584, 1964.
- [68] I. Shevchuk, "A self-similar solution of Navier – Stokes equations for rotating flows between a cone and a disk," *High Temperature*, vol. 42, no. 1, pp. 104-110, 2004.
- [69] I. Shevchuk, "Laminar heat transfer of a swirled flow in a conical diffuser: self-similar solution," *Fluid Dynamics*, vol. 39, pp. 42-46, 2004.
- [70] I. Shevchuk, "Laminar heat and mass transfer in rotating cone-and-plate," *Journal of Heat Transfer*, vol. 133, pp. 024502-1 – 024502-3, 2011.
- [71] G. Le Palec, "Numerical study of convective heat transfer over a rotating rough disk with uniform wall temperature," *International Communications in Heat and Mass Transfer*, vol. 16, pp. 107-113, 1989.
- [72] G. Le Palec, P. Nardin and D. Rondot, "Study of laminar heat transfer over a sinusoidal-shaped rotating disk," *International Journal of Heat and Mass Transfer*, vol. 33, pp. 1183-1192, 1990.
- [73] M. Yoon, J. Hyun and J. Park, "Flow and heat transfer over a rotating disk with surface roughness," *International Journal of Heat and Fluid Flow*, vol. 28, pp. 262-267, 2007.
- [74] R. Webb, E. Eckert and R. Goldstein, "Heat transfer and friction in tubes with repeated-rib roughness," *International Journal of Heat and Mass Transfer*, vol. 14, pp. 601-617, 1971.
- [75] V. Gomelaury, "Influence of two –dimensional artificial roughness on convective heat transfer," *International Journal of Heat and Mass Transfer*, vol. 7, pp. 653-663, 1964.
- [76] D. Dipprey and R. Sabersky, "Heat and momentum heat transfer in smooth and rough tubes at various Prandtl numbers," *International Journal of Heat and Mass Transfer*, vol. 6, pp. 329-353, 1963.
- [77] D. Bettermann, "Contribution á l'étude de la convection forcée turbulente le long de plaques rugueuses," *International Journal of Heat and Mass Transfer*, vol. 9, pp. 401-406, 1976.
- [78] A. Singh, B. Mikic and W. Rohsenow, "Active sites in boiling," *Journal of Heat Transfer*, vol. 98, pp. 401-406, 1976.

- [79] I. Mabuchi, T. Tanaka and M. Kumada, "Studies on convective heat transfer from a rotating disk," *Bulletin of JSME*, Tokyo, 1968.
- [80] I. Mabuchi, T. Tanaka and Y. Sakakibara, "Studies of convective heat transfer from a rotating disk," *Bulletin of JSME*, Tokyo, 1971.
- [81] D. Hannah, "Forced flow against a rotating disc," *British Aerospace Research Community*, United Kingdom, 1947.
- [82] S. Wiesche and C. Helbig, *Convective heat transfer from rotating disks subjected to streams of air*, New York: Springer Cham Heidelberg, 2016.
- [83] J. Owen and R. Rogers, *Flow and heat transfer in rotating-disc systems*, vol. 1, Taunton: Research Studies Press, 1989.
- [84] J. Kierzenka and L. Shampine, "A BVP solver based on residual control and the MATLAB PSE," *ACM Transactions on Mathematical Software*, vol. 27, no. 3, p. 299–316, 2001.
- [85] H. Keller and T. Cebeci, "Accurate numerical methods for boundary-layer flows-I. Two dimensional laminar flows," in *Proc. Ind Int. Conference on Numerical Methods in Fluid Dynamics*, New York, 1971.
- [86] W. J. Minkowycz, E. Sparrow and J. Abraham, *Nanoparticles heat transfer and fluid flow*, New York: CRC Press, Taylor & Franics Group, Boca Raton,, 2013.
- [87] A. Einstein, "Eine neue bestimmung der molekuldimensionen," *Annalen der Physik, Leipzig*, vol. 19, pp. 289-306, 1906.
- [88] H. Brikmann, "The viscosity of concentrated suspensions and solutions," *Journal of Chemical Physics*, vol. 20, pp. 571-581, 1952.
- [89] G. Batchelor, "The effect of Brownian motion on the bulk stress in a suspension of spherical particles," *Journal of Fluid Mechanics*, vol. 83, pp. 97-117, 1977.
- [90] T. Lundgren, "Slow flow through stationary random beds and suspension of spheres," *Journal of Fluid Mechanics*, vol. 51, pp. 273-299, 1972.
- [91] J. Maxwell, *Treatise on electricity and magnetism*, United Kingdom: Calrendon Press, Oxford, 1881.
- [92] D. Brugeman, "Berechnung verschiedener physikalischer konstanten von hetrogenen substanzen," *I. Dielektrizitatskonstanten und liefahigkiten der mischkorper aus isotropen substanzen*, *Annalan der Physik, Leipzig*, vol. 24, pp. 636-679, 1935.